

JYU DISSERTATIONS 216

Sarina Geldhof

Developments for High-Resolution Laser Spectroscopy and Application to Palladium Isotopes



UNIVERSITY OF JYVÄSKYLÄ
FACULTY OF MATHEMATICS
AND SCIENCE

JYU DISSERTATIONS 216

Sarina Geldhof

**Developments for High-Resolution
Laser Spectroscopy and Application
to Palladium Isotopes**

Esitetään Jyväskylän yliopiston matemaattis-luonnontieteellisen tiedekunnan suostumuksella
julkisesti tarkastettavaksi toukokuun 15. päivänä 2020 kello 12.

Academic dissertation to be publicly discussed, by permission of
the Faculty of Mathematics and Science of the University of Jyväskylä,
on May 15, 2020 at 12 o'clock noon.



JYVÄSKYLÄN YLIOPISTO
UNIVERSITY OF JYVÄSKYLÄ

JYVÄSKYLÄ 2020

Editors

Timo Sajavaara

Department of Physics, University of Jyväskylä

Ville Korkiakangas

Open Science Centre, University of Jyväskylä

Copyright © 2020, by University of Jyväskylä

Permanent link to this publication: <http://urn.fi/URN:ISBN:978-951-39-8156-3>

ISBN 978-951-39-8156-3 (PDF)

URN:ISBN:978-951-39-8156-3

ISSN 2489-9003

ABSTRACT

Geldhof, Sarina

Developments for high-resolution laser spectroscopy and application to palladium isotopes

Jyväskylä: University of Jyväskylä, 2020, 90 p. (+included articles)

(JYU Dissertations,

ISSN 2489-9003; 216)

ISBN 978-951-39-8156-3 (PDF)

Diss.

In this work, collinear laser spectroscopy on stable and neutron-rich Pd isotopes was performed. This led to the first determination of changes in mean-square charge radii of $^{112,114,116,118}\text{Pd}$, using atomic factors calibrated during extensive testing on the stable Pd isotopes. The results were compared to nuclear density functional theory, consisting of calculations using Skyrme-type energy density functionals, and new calculations using two Fayans energy density functionals, $Fy(\text{std})$ and $Fy(\Delta r, \text{HFB})$. The recently developed Fayans functionals have been shown to be particularly good at reproducing charge radii in spherical nuclei, and are applied to deformed nuclei for the first time in this work. $Fy(\Delta r, \text{HFB})$ agrees well with the measured charge radii, which show a smooth parabolic trend with increasing neutron number. Technical developments related to frequency stabilisation, crucial for collinear laser spectroscopy, have been conducted and applied for the experiments in this thesis. In parallel, techniques for frequency determination were investigated, with the characterisation of Fabry-Pérot interferometers and an in-depth analysis of a commercial wavemeter. This is important for (high-resolution) laser spectroscopy techniques whereby the laser frequency is scanned rather than stabilised, for example in-source resonant laser ionisation and in-gas-jet laser spectroscopy.

Keywords: Collinear laser spectroscopy, frequency determination, nuclear charge radii, IGISOL, palladium

Author	Sarina Geldhof Department of Physics University of Jyväskylä Jyväskylä, Finland
Supervisor	Prof. Iain Moore Department of Physics University of Jyväskylä Jyväskylä, Finland
Reviewers	Asst. Prof. Xiaofei Yang School of Physics and State Key Laboratory of Nuclear Physics and Technology Peking University Beijing, China Adj. Prof. Kei Minamisono National Superconducting Cyclotron Laboratory Michigan State University East Lansing, MI, USA
Opponent	Prof. Kieran Flanagan School of Physics and Astronomy The University of Manchester Manchester, United Kingdom

PREFACE

Six years ago, my Erasmus application was approved, and I knew I'd be spending an exchange semester in Jyväskylä. Before receiving the list of possible destinations a few months before that, I had never heard of the city. I had always said I wanted to go North for my Erasmus however, and the corresponding Master thesis topic was interesting, so to Finland I went. By now I have spent over five years total here, with this PhD thesis as the final accomplishment, and there are many people to thank for that.

First and foremost, I would like to thank my supervisor Prof. Iain Moore for his invaluable support and advice. His trust in me gave me the confidence needed to see it all through. I've been lucky to have been part of an amazing research group, and for this I want to thank all IGISOL members both past and present. My gratitude goes to the head of the group, Prof. Ari Jokinen, for making sure I stayed on track. Special mention goes to Dr Annika Voss for being a great mentor during my first years and the numerous coffee breaks discussing life. I want to thank Dr Ruben de Groote for sharing his expertise on all things laser spectroscopy, especially the experimental and data analysis parts. None of the work in this thesis would have been possible without the support from the other laser group members, so big thanks to Ilkka, Wouter, Mikael and Agi. Life in the lab, and outside of it, wouldn't have been as pleasant without them and the other IGISOL students and post docs: Laetitia, Antoine, Marjut, Clément, Olga, Lama, Ville, Markus and Sasha. Thank you so much for your company and support.

The collinear laser spectroscopy setup at IGISOL is not just a local effort, but an international one. I would thus like to thank our UK collaborators, Prof. Bradley Cheal and Dr Paul Campbell for their continuous support and much appreciated advice, and Charlie for helping out with experiments. I would also like to thank the other external collaborators on the palladium experiment, Dr Lucia Caceres, Kati Chrysalidis and Felix Sommer. My deepest gratitude goes to Dr Markus Kortelainen for performing the theoretical calculations in this thesis, and for helping me make sense of all EDF-related parts.

A lot of the technical work in this thesis was also performed as part of larger collaborations, i.e. with Nagoya University, KU Leuven, TU Darmstadt and JGU Mainz. I would like to thank all people involved, in particular Ryohei Terabayashi, Matthias Verlinde, Phillip Imgram and Dominik Studer. I had the opportunity to join some experiments at ISOLDE, CERN, which were a great learning experience. For this I would like to thank the CRIS collaboration, and the group of Prof. Piet Van Duppen. Being part of a European-funded project has also been an invaluable experience, for which my gratitude goes to the nuClock consortium.

Life is not just physics however, but also concerts, dancing, parties, board games, brunches, etc. I owe a huge thanks to Hussam, Jae, Danny, Philippos, Arus, Fabi, Ana, Elise, Holly, Daniel, Joonas, and so many others for all the unforgettable memories. For most of my PhD I was also a volunteer at the Erasmus Student Network, where I've learned skills beyond physics and had such great times thanks to all the other wonderful volunteers. Two years ago I dusted off my flute and joined the wind orchestra Puhkupillit, thank you for reminding me of my love for playing music and some great moments together.

Bedankt ook aan Sara, Sofie, Fien, Maaïke, Sarah, Sien en Dries voor alle toffe (chat)gesprekken en reünies in België. Mijn studies en verhuis naar Finland waren nooit mogelijk geweest zonder de steun van mijn volledige familie. Bedankt mama en papa voor alles, vooral om mij altijd vrij mijn toekomst te laten kiezen en alles te doen om het mogelijk te maken, ook al maakte ik vaak niet de gemakkelijkste keuzes voor jullie. Merci Heleen om er ook altijd te zijn voor mij, en voor alle geweldige reizen samen. Finally, thank you Hentter for always listening to my rants and calming me down during this writing process (and every other time), you've made Jyväskylä feel like even more of a home than it did 1.5 years ago.

Jyväskylä, April 2020

Sarina Geldhof

ACKNOWLEDGEMENTS

The work presented in this thesis has been supported by the Academy of Finland programme under the Finnish Centre of Excellence Programme 2012–2017 (Project No. 251353, Nuclear and Accelerator-Based Physics Research at JYFL), and the European Unions Horizon 2020 research and innovation programme under Grants Agreements No. 654002 (ENSAR2) and No. 664732 (nuClock).

LIST OF INCLUDED ARTICLES

This thesis is based on the three publications listed below as well as an additional experiment which is being prepared for publication. In article [PII] the author has conducted the experiments, data analysis and writing related to the Jyväskylä contribution, while for the other two articles [PI] and [PIII] the author performed the experiments, all data analysis and writing. In addition to the listed papers, the author has actively participated in other experiments at IGISOL and ISOLDE, CERN, resulting in several peer-reviewed publications as a co-author.

- PI S. Geldhof, S. El Youbi, I. D. Moore, I. Pohjalainen, V. Sonnenschein, R. Terabayashi, A. Voss. Development of a saturated absorption spectroscopy setup at IGISOL for characterisation of Fabry-Pérot interferometers. *Hyperfine Interactions* **238**: 7 (2017).
- PII M. Verlinde, K. Dockx, S. Geldhof, K. König, D. Studer, T. E. Cocolios, R. P. de Groote, R. Ferrer, Yu. Kudryavtsev, T. Kieck, I. Moore, W. Nörtershäuser, S. Ræder, P. Van den Bergh, P. Van Duppen, K. Wendt. On the performance of wavelength meters: Part 1 – Consequences for medium-to-high-resolution laser spectroscopy. *Applied Physics B* **126**, 85 (2020).
- PIII S. Geldhof, P. Campbell, B. Cheal, R. P. de Groote, W. Gins, I. D. Moore. Collinear laser spectroscopy of stable palladium isotopes at the IGISOL facility. *Hyperfine Interactions* **241**: 41 (2020).

CONTENTS

ABSTRACT

PREFACE

ACKNOWLEDGEMENTS

LIST OF INCLUDED ARTICLES

CONTENTS

1	INTRODUCTION	1
2	THEORY	4
2.1	Fine and hyperfine structure	4
2.1.1	Magnetic dipole moment	6
2.1.2	Electric quadrupole moment	6
2.2	Isotope shift	7
2.2.1	Mass shift	7
2.2.2	Field shift	8
2.2.3	King Plot technique	8
2.2.4	Mean-square charge radius	9
2.3	Concepts from laser spectroscopy	12
2.3.1	Detecting the hyperfine structure	12
2.3.2	Spectral line shape	14
2.4	Nuclear theory	15
2.4.1	Nuclear mean field	16
2.4.2	Nuclear density functional theory	17
3	FREQUENCY DETERMINATION AND STABILISATION USING FABRY-PÉROT INTERFEROMETERS AND SATURATED ABSORPTION SPECTROSCOPY	20
3.1	Saturated absorption spectroscopy technique	20
3.2	Setup	23
3.3	FPI Free Spectral Range calibration	25
3.4	Temperature stabilisation	27
3.5	Frequency stabilisation	29
3.6	Summary and outlook	32
4	COLLINEAR LASER SPECTROSCOPY AT IGISOL	34
4.1	Collinear laser spectroscopy technique	34
4.2	Experimental setup	36
4.2.1	Ion beam production at IGISOL-4	36
4.2.2	Collinear laser spectroscopy beamline	38
4.2.3	Laser system	39
4.3	Systematic tests	40

4.3.1	Wavemeter tests	40
4.3.2	Frequency stabilisation.....	43
5	MEAN-SQUARE CHARGE RADII OF NEUTRON-RICH PALLADIUM ISOTOPES	47
5.1	Motivation.....	47
5.2	Offline work on stable isotopes	50
5.3	Experimental details and data analysis	52
5.3.1	Status of odd- <i>A</i> data	53
5.3.2	Data handling	54
5.3.3	Bootstrapping analysis	56
5.3.4	Systematic errors	57
5.4	Results and discussion	58
5.5	Outlook	63
6	SUMMARY AND OUTLOOK	65
	REFERENCES.....	68
	INCLUDED ARTICLES	

1 INTRODUCTION

The fields of atomic and nuclear physics have a greatly interlinked history. Landmark experiments towards an understanding of the atomic structure were the detection of radioactivity by Henri Becquerel in 1896, and the discovery of the electron by J.J. Thomson the following year. The onset of nuclear physics research came with the discovery of the atomic nucleus in the pioneering experiments by Rutherford in 1911. Not long after, the first atomic model built on Planck's theory of energy quantisation was proposed by Niels Bohr, giving rise to the atomic shell model.

Early work studying nuclei of stable or long-lived isotopes presented a vast array of data, which led to the development of the nuclear shell model in order to interpret the underlying nuclear structure. This nuclear shell model, similar to the atomic shell model, shows that nuclei that have certain so-called magic numbers of protons (Z) and/or neutrons (N) are more stable, i.e. are more tightly bound.

With the construction of radioactive beam facilities worldwide, experiments could be conducted on isotopes far from stability. This has led to the discovery of many nuclear structure phenomena that challenge the classical shell model picture, such as the disappearance of magic numbers and appearance of new ones [1]. Several experiments showed the rich picture of shapes of atomic nuclei, from prolate/oblate to pear-shaped [2], and possible coexistence [3] or rapid changes between them.

The study of these shapes, and other fundamental properties of nuclei, can be done by probing the so-called hyperfine structure, which consists of the minuscule changes and splittings of atomic energy levels due to the influence of the nucleus. The resolution needed to examine this in detail came with the invention of the laser in the 1960's and the subsequent advent of laser spectroscopy techniques.

One of these techniques in routine use at radioactive beam facilities is collinear laser spectroscopy, which relies on a combination of lasers and fast ion beams in a collinear geometry to reduce Doppler broadening. Pioneering collinear laser spectroscopy experiments were done at ISOLDE, CERN, where there are currently two dedicated beamlines (COLLAPS [4] and CRIS [5]). Other experiments are set up at Michigan State University, USA, (BECOLA) [6]; at the ISAC facility TRIUMF, Canada (CFBS) [7]; and at the IGISOL facility, JYFL, Finland. The latter is where all the work in this thesis has taken place. Some experiments are in the commissioning phase, e.g. at Argonne National Laboratory, USA [8], and at ALTO, France (LINO) [9]. There are also experiments planned at future facilities, e.g. at the FAIR facility, GSI, Germany (LaSpec) [10], the SPIRAL-2 facility, GANIL, France (LUMIERE) [11], and the BRIF facility, China Institute of Atomic Energy.

As mentioned, this work took place at the IGISOL facility at the Accelerator Laboratory of the University of Jyväskylä, Finland. Several developments on the continuous-wave (cw) laser systems were made, mainly with the aim to improve frequency determination and stabilisation methods. As laser spectroscopy techniques are being pushed further in terms of resolution and sensitivity, it is ever more important to understand systematic effects due to the laser systems.

Recent upgrades to the collinear laser spectroscopy experiment, such as the installation of a charge-exchange cell and a new cw laser system, have allowed the first experiment on exotic palladium isotopes to be performed, which is part of this work. The results from this experiment led to the determination of the (nuclear) charge radius of the Pd isotopes, a measure of the size of the nucleus. One of the main interests in measuring the charge radius is its sensitivity to deformation, which makes it an excellent probe into the shape of the nucleus, and possible changes in shape along an isotopic chain. Properly reproducing charge radii is also an important test of theoretical nuclear models, as it requires the theory to correctly predict both the bulk size of the nucleus, and the subtle effects such as deformation which affect it.

This thesis is structured as follows. In chapter 2, the theoretical background for this research is outlined. It consists of selected topics of atomic and nuclear physics, mainly related to the structure of atomic spectra, concepts from laser spectroscopy, and an introduction to nuclear theory, focused on nuclear density functional theory.

Chapter 3 proceeds with technical developments towards better frequency determination and stabilisation. This was based on the use of a saturated absorption spectroscopy setup, with two Fabry-Pérot interferometers. The technique and setup are discussed, and the results from several tests presented. The work of Article [PI] is part of this chapter. Chapter 4 presents the experimental setup for the collinear laser spectroscopy experiment on Pd isotopes, from the ion production

to the collinear beamline and the laser system. It also includes systematic tests of the laser system, of which Article [PII] presents additional details.

In chapter 5 the experiment on Pd isotopes and its results are discussed. It starts with the motivation for this work, and the preparation on stable isotopes. The work on stable isotopes is detailed in Article [PIII]. The experimental details and data analysis are outlined. Next the results and discussion are presented, and the chapter ends with an outlook. Chapter 6 summarises this thesis work, and gives a general outlook.

2 THEORY

Optical spectroscopy operates at the intersection of atomic and nuclear physics, measuring the small effects the nucleus imprints on atomic energy levels in order to understand the underlying nuclear structure. Therefore this chapter contains both atomic as well as nuclear theory. Firstly, the fine and hyperfine structure are discussed, detailing how the atomic energy levels are formed, and the key role of the nuclear electromagnetic moments in this. The following section explains the atomic isotope shift and the related mean-square nuclear charge radius. The third section introduces some basic aspects of laser spectroscopy techniques relevant throughout this work. Lastly, a short overview of nuclear theory is given, with a focus on nuclear density functional theory, which is the model used to compare with the newly measured data obtained in this work.

2.1 Fine and hyperfine structure

To a first approximation, the atomic energy levels are determined by the movement of the electrons in the Coulomb field of a point-like nucleus, and the interactions between themselves. This gives rise to an orbital atomic structure, divided in shells labeled by their principal quantum number n , a positive integer. These are further divided in subshells defined by the orbital angular momentum quantum number l . The orbital quantum number can have a value from 0 up to $n - 1$. Each subshell can be occupied by $2(2l + 1)$ electrons, owing to their orbital magnetic quantum number m_l ($-l \leq m_l \leq l$) and spin magnetic quantum number m_s ($= \pm 1/2$). These states are labeled with the electron configuration using the nl^N notation, N being the number of electrons in subshell l .

The spin-orbit interaction between the spin s and orbital angular momentum l

of the electron leads to the coupling of these two to a total angular momentum $\mathbf{j} = \mathbf{l} + \mathbf{s}$. This coupling splits each subshell further into two levels, known as the fine structure. To obtain the total angular momentum \mathbf{J} of an atom, the individual angular momenta \mathbf{j} need to be added. The order in which this happens defines the coupling scheme, using the angular momentum addition theorem. The most prevalent coupling schemes are the LS-coupling, mainly applicable to light elements, and the jj-coupling, used in heavy elements. In the LS-coupling scheme all the orbital angular momenta are added to form the total angular momentum $\mathbf{L} = \sum_i \mathbf{l}_i$ and similarly all spins are added to form the total spin angular momentum $\mathbf{S} = \sum_i \mathbf{s}_i$. The total angular momentum is then obtained by adding these together: $\mathbf{J} = \mathbf{L} + \mathbf{S}$. The jj-coupling scheme involves first coupling the individual spin and orbital angular momentum together to form the electron angular momentum \mathbf{j} , and then adding these to acquire the total angular momentum $\mathbf{J} = \sum_i \mathbf{j}_i$.

Often the fine structure states will be formed using LS-coupling, and labeled with the corresponding atomic term symbol $^{2S+1}L_J^{\circ/-}$. This symbol expresses the total orbital angular momentum L , the total spin angular momentum S and the parity of the state. The electron configuration with addition of the term symbol uniquely defines a state. To obtain the final energies of these atomic levels, the Darwin term, relativistic corrections and Lamb shift have to be accounted for.

Thus far the internal structure of the nucleus has not been taken into account. The electromagnetic interaction between the nuclear moments and the surrounding electrons results in an additional splitting and perturbation of the fine structure levels called the hyperfine structure. This is a very small effect, on the order of μeV (compared to meV due to the fine structure). Labeling of these hyperfine states is done using the total angular momentum \mathbf{F} resulting from the coupling of the nuclear spin \mathbf{I} and atomic spin \mathbf{J} , $\mathbf{F} = \mathbf{I} + \mathbf{J}$. The quantum number F can thus range from $|I - J|$ to $I + J$. The individual contributions of each nuclear moment to the hyperfine level energies can be investigated by using a multipole expansion of the Hamiltonian of the nucleus-electron interaction. Only odd-order magnetic and even-order electric moments have a non-zero contribution to this. In practice, laser spectroscopy techniques are usually limited to measuring up to second order, as higher orders have progressively smaller effects and standard laser spectroscopy techniques do not reach the needed resolution. Hence only the nuclear magnetic dipole and electric quadrupole moments will be considered here. As no nuclear moments were measured in this work, only a short overview will be given. Further details on their determination and interpretation can be found e.g. in [12].

2.1.1 Magnetic dipole moment

The nuclear magnetic dipole moment μ can be written as $\mu = gI\mu_N$, where g is called the g -factor and $\mu_N = \frac{e\hbar}{2m_p}$ is the nuclear magneton. Only nuclei with non-zero spin have an observable magnetic moment, which through its interaction with the magnetic field generated by the electron cloud provides the largest contribution to the hyperfine splitting. The associated term in the interaction Hamiltonian can be written as

$$\mathcal{H}_{M1} = - \int_V \mathbf{B} d\mu = -\mu \cdot \mathbf{B}_0 = -\frac{\mu B_0}{\hbar^2 I J} \mathbf{I} \cdot \mathbf{J} \quad (2.1)$$

where the integral is solved assuming the magnetic field is constant over the nuclear volume, given by B_0 . The energy change of a hyperfine sublevel due to this term can be evaluated as [13]

$$\Delta E_{M1}(F) = -\frac{1}{2} \overbrace{\frac{\mu B_0}{I J}}^A \overbrace{[F(F+1) - I(I+1) - J(J+1)]}^K \quad (2.2)$$

with the hyperfine parameter A thus defining the energy shift.

Nuclear magnetic moments mainly offer information on the shell model configuration of a particular nuclear state, as they are very sensitive to which orbits are occupied by the valence particles [12].

2.1.2 Electric quadrupole moment

The second term in the nucleus-electron interaction Hamiltonian is due to the interaction between the electric quadrupole moment of the nucleus and the electric field gradient generated by the electrons. For nuclei with $I > 1/2$ and electronic states with $J > 1/2$ this results in an energy change for a hyperfine sublevel of

$$\Delta E_{E2}(F) = \overbrace{e Q_s V_{zz}}^B \frac{3K(K+1) - 4I(I+1)J(J+1)}{8I(2I-1)J(2J-1)} \quad (2.3)$$

with the hyperfine parameter B defined in terms of the spectroscopic quadrupole moment Q_s and the electric field gradient $V_{zz} = \frac{\partial^2 V}{\partial z^2}$.

The spectroscopic quadrupole moment is a measure of the deformation of the nucleus, i.e. the deviation from sphericity, and it can be used to evaluate the intrinsic quadrupole moment Q_0 . For well-deformed axially symmetric nuclei in the strong coupling limit, the relation between the two can be given by [12]

$$Q_s = \frac{3\Omega^2 - I(I+1)}{(I+1)(2I+3)} Q_0 \quad (2.4)$$

where Ω is the projection of the total spin I onto the symmetry-axis of the deformed nucleus. The intrinsic quadrupole moment can then be expressed in terms of the quadrupole deformation parameter β_2

$$Q_0 = \frac{3}{\sqrt{5\pi}} Z \langle r_{sph}^2 \rangle \langle \beta_2 \rangle (1 + 0.36 \langle \beta_2 \rangle). \quad (2.5)$$

Thus a measure of the static quadrupole deformation $\langle \beta_2 \rangle$ may be obtained, although it depends on the model dependence of the coupling and choice of spherical radius.

2.2 Isotope shift

The nuclear mass, size and shape cause a change in the transition frequency (or the centroid of a hyperfine structure) between two isotopes of the same element, ν^A and $\nu^{A'}$, called the isotope shift $\delta\nu^{A,A'} = \nu^{A'} - \nu^A$. The isotope shift consists of two main components called the mass shift $\delta\nu_{MS}^{A,A'}$ and the field shift $\delta\nu_{FS}^{A,A'}$

$$\delta\nu^{A,A'} = \delta\nu_{MS}^{A,A'} + \delta\nu_{FS}^{A,A'}. \quad (2.6)$$

A full treatment of isotope shifts can be found in e.g. [14], here a summary of relevant parts will be given.

2.2.1 Mass shift

The mass shift accounts for the recoil motion of a nucleus with finite mass during an electronic excitation and can be expressed as

$$\delta\nu_{MS}^{A,A'} = M \frac{m_{A'} - m_A}{m_{A'} m_A}, \quad (2.7)$$

where M is the mass shift factor and $m_{A,A'}$ are the atomic masses [15]. The mass shift factor may be divided into the normal mass shift (NMS) and specific mass shift (SMS) factors, $M = M_{NMS} + M_{SMS}$. The normal mass shift can be calculated accurately, $M_{NMS} = \nu m_e / m_u$, with ν the transition frequency for an infinitely heavy nucleus. The specific mass shift however arises due to correlations between the electron momenta, which are increasingly difficult to compute when going from light to heavy elements. The mass shift does not offer any nuclear information of interest, but it needs to be accounted for in order to reliably extract the field shift, from which the change in mean-square charge radii can be deduced.

2.2.2 Field shift

The field shift arises from the effect of the nuclear charge distribution on the electrostatic potential experienced by the electrons. The difference in energy shift between two isotopes can be written as

$$\delta E = e \int_0^\infty \psi_e^*(r) \delta V(r) \psi_e(r) d^3 r. \quad (2.8)$$

Here $\psi_e(r)$ is the electron wave function and $\delta V(r)$ is the change in electrostatic potential between the two isotopes. If the electron wave function is assumed to be constant over the nuclear volume this results in a frequency change of

$$\delta \nu_{FS}^{A,A'} = \overbrace{\frac{Ze^2}{6h\epsilon_0} \Delta |\psi_e(0)|^2}^F \delta \langle r^2 \rangle^{A,A'} \quad (2.9)$$

where F is called the atomic field shift factor. The $\Delta |\psi_e(0)|^2$ term corresponds to the change in electron density at the nucleus between the two atomic states involved in the transition and $\delta \langle r^2 \rangle^{A,A'}$ is the change in mean-square charge radii between the two isotopes. The dependency on $\Delta |\psi_e(0)|^2$ causes transitions involving a change in the number of valence s-electrons to exhibit the largest field shifts, and hence greatest sensitivity to changes in mean-square charge radii.

As the approximation of a constant electron density over the nuclear volume becomes less valid for heavier nuclei, the field shift is more generally expressed as

$$\delta \nu_{FS}^{A,A'} = F(Z) \lambda^{A,A'} = FK(Z) \delta \langle r^2 \rangle^{A,A'}, \quad (2.10)$$

where $\lambda^{A,A'}$ is the Seltzer moment which depends on higher-order radial moments with tabulated values for $K(Z)$ [16].

2.2.3 King Plot technique

In order to extract changes in mean-square charge radii from the isotope shifts, the transition-dependent atomic mass and field shift factors mentioned in the previous sections must be determined. This can be done either via atomic theory calculations, using for example the multiconfiguration Dirac-Fock (MCDF) method, which can reach an estimated accuracy of $\sim 10 - 15\%$ in certain cases [17], or empirically via the King plot technique [14]. A King plot can be constructed on the basis of either changes in charge radii obtained from non-optical experimental methods or known atomic factors from another transition.

Combining equations 2.7 and 2.9 gives the following expression for the isotope shifts of a transition i

$$\delta \nu_i^{A,A'} = \frac{m_{A'} - m_A}{m_{A'} m_A} M_i + F_i \delta \langle r^2 \rangle^{A,A'}. \quad (2.11)$$

Multiplying this with a modification factor κ ,

$$\kappa^{A,A'} = \frac{m_A m_{A'}}{m_{A'} - m_A} \quad (2.12)$$

removes the dependence on nuclear masses and yields the so-called modified isotope shifts, which can be written as

$$\kappa^{A,A'} \delta v_i^{A,A'} = M_i + F_i \kappa^{A,A'} \delta \langle r^2 \rangle^{A,A'}. \quad (2.13)$$

These modified isotope shifts can be plotted against the modified isotope shifts of another transition j , $\kappa^{A,A'} \delta v_j^{A,A'}$, or the modified experimental changes in mean-square charge radii $\kappa^{A,A'} \delta \langle r_{exp}^2 \rangle^{A,A'}$, which may exist in literature having been determined using other techniques for the (stable) isotopes. Either plot should yield a straight line. In the case of plotting against the modified changes in mean-square charge radii, the gradient gives the field shift factor and the intercept the mass shift factor of the transition of interest i directly. An example of a King plot using this method on palladium isotopes can be seen in Fig. 2.1. When using another atomic/ionic transition, the gradient is given by $\frac{F_i}{F_j}$ and the intercept by $M_i - M_j \frac{F_i}{F_j}$.

2.2.4 Mean-square charge radius

An important basic property of the nucleus is its size, which is usually characterised by its radius. The total radius, also called the mass or matter radius, cannot be measured with methods relying on an electromagnetic process, such as laser spectroscopy. These techniques are only sensitive to the charged protons, and thus the so-called charge radius of the nucleus is obtained.

In the most simple approach, the nucleus can be described as a homogeneously charged liquid drop. The mean-square charge radius in this case is given by

$$\langle r^2 \rangle = \frac{3}{5} r_0 A^{2/3}, \quad (2.14)$$

where $r_0 \approx 1.2$ fm. If the homogeneous distribution is replaced by a general charge density distribution $\rho(\mathbf{r})$, the mean-square charge radius corresponds to its second radial moment

$$\langle r^2 \rangle = \frac{1}{Ze} \int \rho(\mathbf{r}) r^2 d\mathbf{r}. \quad (2.15)$$

It is in the deviations of the mean-square charge radii from the trend predicted by the liquid drop model that information on the underlying nuclear structure can be elucidated. One of the main factors is deformation, which will lead to an increase

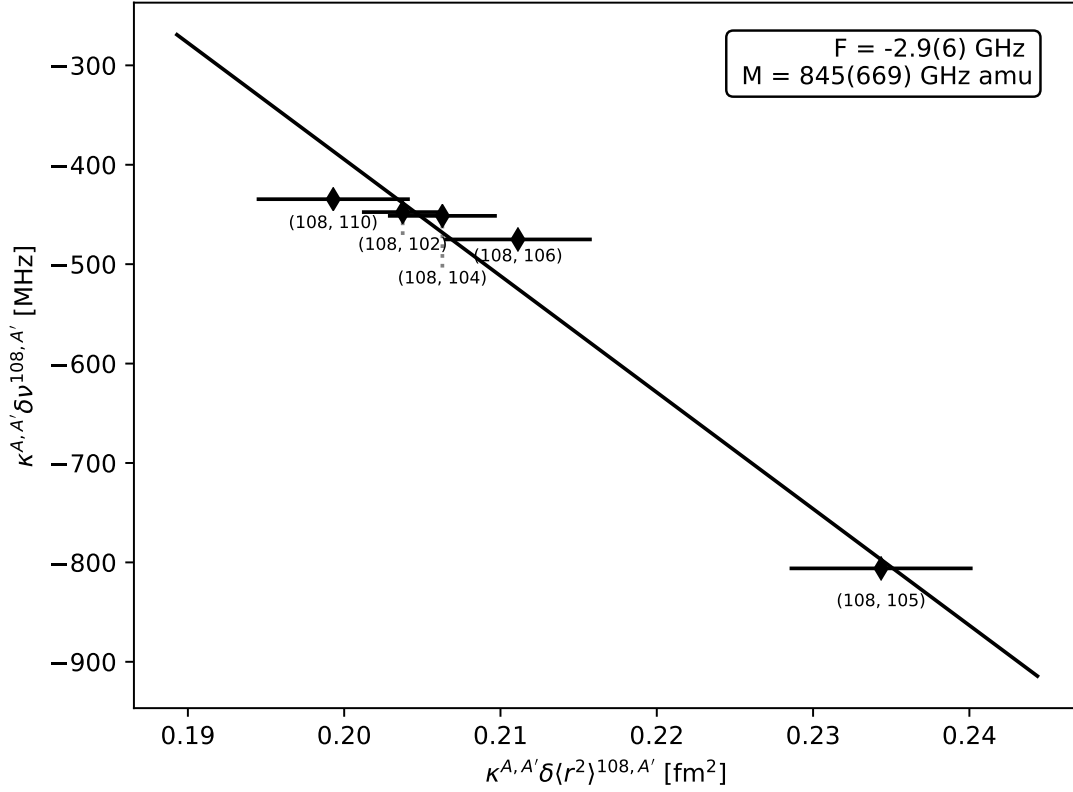


FIGURE 2.1 Example of a King plot for Pd isotopes using known mean-square charge radii of all stable isotopes [18] and measured isotope shifts with respect to the reference isotope $A = 108$. Statistical error bars on the isotope shifts are within the data points.

of the charge radius. This can be shown by expanding Eq. 2.15 using spherical harmonics:

$$\langle r^2 \rangle = \langle r_{sph}^2 \rangle \left(1 + \frac{5}{4\pi} \sum_i \langle \beta_i^2 \rangle \right), \quad (2.16)$$

with $\langle r_{sph}^2 \rangle$ the mean-square charge radius of a spherical nucleus with the same volume and β_i the deformation parameters of order i . For an axially symmetric deformed nucleus with quadrupole deformation parameter β_2 , this becomes

$$\langle r^2 \rangle = \langle r_{sph}^2 \rangle \left(1 + \frac{5}{4\pi} \langle \beta_2^2 \rangle \right). \quad (2.17)$$

The mean-square of the quadrupole deformation parameter $\langle \beta_2^2 \rangle$ contains contributions of both static and dynamic quadrupole deformation, as opposed to the ‘static-only’ contribution to the quadrupole moment obtained from the hyperfine structure (see Eq. 2.5). Comparing both thus gives information about the rigidity of the (deformed) nucleus. This information on the deformation can be correlated to measurements of transition probabilities $B(E2)$ between the first 2^+ and the 0^+ ground state of even-even nuclei [19–21], as $\langle \beta_2^2 \rangle \approx \left(\frac{4\pi}{3Ze^2r_0^2} \right) \sqrt{B(E2)}$ [22].

Another example of nuclear structure effects on the charge radii is the sudden change in the slope of the charge radii in an isotopic chain, also called a *kink*, observed when crossing a magic number. This is clearly visible throughout the nuclear chart [23] and has been linked to reduced correlations at magic numbers [24].

In addition to these kinks, a widespread phenomenon throughout the nuclear chart is the observation that the charge radius of an odd-neutron isotope is usually smaller than the average charge radius of its even-N neighbours. This is called the odd-even staggering (OES), and can be quantified using the three-point OES parameter $\Delta_r^{(3)} = 1/2(r_{A+1} - 2r_A + r_{A-1})$. A complete understanding of the microscopic origins of this effect is not yet available, although qualitatively it can be linked to the odd neutron blocking pair scattering. The observation of sudden changes in the magnitude of the OES, or even a complete inversion, complicates the picture further, see for example [25, 26]. Inversion of the OES has been linked to octupole deformation [27], although this is unlikely to explain all observations of inversion.

In addition to being deduced from isotope shifts measured with laser spectroscopy techniques, the nuclear charge distribution can also be measured using a variety of non-optical methods, including K X-ray spectroscopy, high-energy elastic electron scattering and muonic atom spectroscopy.

Non-optical methods K X-ray Spectroscopy is a variation of optical spectroscopy as it also measures isotope shifts, but using inner-shell X-ray transitions. This makes the calculation of the field and mass shift factors easier and more reliable. Due to experimental restrictions however the achievable precision is much lower than in optical spectroscopy, yielding errors of at least an order of magnitude larger [18].

In high-energy electron scattering, a certain amount of momentum q is transferred from the electron to the nucleus, which can be determined from the electron energy and the measured angular distribution of the scattered electrons. This then leads to the calculation of the so-called form factor $F(q)$, which accounts for the effect of an extended nucleus. In the plane-wave Born approximation, a spherically symmetric nuclear charge distribution is equal to the Fourier-Bessel transformation of the form factor [28], which then yields the root-mean-square (rms) charge radius. Electron scattering has an advantage over optical techniques for very light nuclei, owing to their extremely small field shifts. The main disadvantages are the limited accuracy and the need for at least tens of milligrams of the material of interest, limiting the technique to measuring only stable elements so far. However, the SCRIT electron scattering facility, aiming at electron scattering off short-lived unstable nuclei, has recently been commissioned [29].

The last non-optical method is muonic atom X-ray spectroscopy. This technique relies on the fact that a muon in an atom will lie closer to the nucleus than an electron, as a muon is much heavier ($\sim 200\times$). This allows for the system to be treated as a nucleus with a single 'electron', making theoretical calculations of the muonic energy levels straightforward when assuming a point-like nucleus [28]. From the deviations of the measured energy levels from these point-nucleus calculations the charge radius can be extracted. This technique also has the disadvantage of needing a substantial amount of target material.

2.3 Concepts from laser spectroscopy

Two laser spectroscopy techniques were used in this work, saturated absorption spectroscopy and collinear laser spectroscopy. Their particular details will be discussed later, but some general aspects related to laser spectroscopy experiments will be covered here.

2.3.1 Detecting the hyperfine structure

Laser spectroscopy experiments probe the atomic hyperfine structure by irradiating the atom with laser light, with the goal of extracting nuclear ground state properties. Multiple review papers of the field have been published, e.g. by Otten [30], including the theoretical basis, and the most recent by Campbell, Moore, and Pearson [31].

A laser photon can be absorbed by an atom only if two conditions are met:

1. The photon energy $h\nu$ should match the energy difference between two hyperfine components, each belonging to a different fine structure level. Using Equations 2.2 and 2.3, the energy shift up to second order for an atomic hyperfine component with respect to the unperturbed fine structure level is given by

$$\Delta E_{HFS} = A \frac{K}{2} + B \frac{3K(K+1) - 4I(I+1)J(J+1)}{8I(2I-1)J(2J-1)}. \quad (2.18)$$

Taking into account the isotope shift, Eq. 2.6, as well, the laser photon energy E must be equal to

$$E = h\nu = h\nu_0 + h\delta\nu_{MS}^{A,A'} + h\delta\nu_{FS}^{A,A'} - \Delta E_{HFS_l} + \Delta E_{HFS_u} \quad (2.19)$$

where $h\nu_0$ is the energy of the fine structure transition of the reference isotope, and l and u denote the lower and upper level respectively.

2. Given an allowed fine structure transition, the transition between the two hyperfine levels must be allowed. As a photon carries one unit of angular momentum, this means a $F = 0$ to $F = 0$ transition is forbidden, and for dipole transitions $\Delta F = 0, \pm 1$.

Measuring the laser frequencies that lead to excitation of the atom, e.g. by recording the de-excitation photons, thus provides a hyperfine spectrum. From this, information on the A - and B -parameters for one or both levels of the transition can be obtained. This allows the extraction of the nuclear moments μ and Q_s using a precise calculation of the relevant electromagnetic fields or, more commonly, extracting the ratio of the nuclear moments of a pair of isotopes using the relationships (see Eq. 2.2 and 2.3)

$$\frac{A}{A'} \simeq \frac{\mu}{\mu'} \frac{I'}{I} \quad \frac{B}{B'} \simeq \frac{Q_s}{Q'_s} \quad (2.20)$$

where A , B , μ , Q_s and I are the hyperfine and nuclear properties for a reference isotope, and A' , B' , μ' , Q'_s and I' for an isotope newly measured (using the same atomic level). Knowledge of the moments of a reference isotope, measured for example using Nuclear Magnetic Resonance (NMR) [12], thus allows for an approximate determination of the unknown moments. It is approximate as it relies on the assumption of a constant B_0 and V_{zz} for all isotopes, meaning no differential change in the distribution of nuclear magnetism and charge. For electric quadrupole moments, so far no experiments have seen any differential changes [32]. It has been noticed in the determination of magnetic dipole moments across isotopic chains however that deviations can exist. These deviations are collectively known as hyperfine anomalies ${}^A\Delta^{A'}$. The relation in Eq. 2.20, only valid for point-like nuclei, is then written as $\frac{A}{A'} = \frac{\mu I'}{\mu' I} (1 + {}^A\Delta^{A'})$. Usually, the hyperfine anomaly is very small, on the 10^{-4} level, but for specific cases it can be on the order of a few percent [33].

The difference between the centroids of the hyperfine spectra gives the isotope shift. If the atomic field and mass shift factors can be calibrated, e.g. by the King plot technique described in section 2.2.3, $\delta\langle r^2 \rangle^{A,A'}$ can be extracted from the isotope shift independent of nuclear models. This is an important advantage compared to the non-optical methods. Only changes in mean-square charge radii can be measured however, so in order to obtain absolute radii, results from a non-optical method must be available for at least one (stable) reference isotope. Isotope shifts with respect to this reference isotope must then be measured by recording the hyperfine spectrum of the reference in conjunction with the spectra of the isotopes of interest.

2.3.2 Spectral line shape

The resonance peaks in the hyperfine spectrum have a minimal linewidth due to Heisenberg's uncertainty principle, called the natural linewidth. It is determined by the limited lifetime τ of an excited atomic state according to

$$\Delta\nu_0 = \frac{\Delta E}{h} = \frac{1}{2\pi\tau}, \quad (2.21)$$

and is described by a Lorentzian lineshape. It is very difficult to obtain this natural linewidth in experiments however, as the width and shape of the peaks are influenced by several other broadening mechanisms. One such mechanism is power broadening, which increases the linewidth of the Lorentzian profile to

$$\Delta\nu_P = \Delta\nu_0 \sqrt{1 + \frac{I}{I_s}} \quad (2.22)$$

where I is the applied laser intensity and I_s the saturation intensity, given by

$$I_{sat} = \frac{\pi\hbar c}{3\lambda^3\tau}, \quad (2.23)$$

with λ the laser wavelength. Power broadening is due to stimulated emission induced by the laser photons, as this decreases the lifetime of the excited state compared to a scenario with only spontaneous decay. As the laser power increases, so does the stimulated emission rate, which subsequently leads to shorter lifetimes and thus an increased linewidth.

The observed transition linewidth can also be affected by Doppler broadening. If an atom is moving with a velocity v with respect to the observer, the non-relativistic shifted frequency is

$$\nu = \nu_0 \left(1 \pm \frac{v}{c}\right) \quad (2.24)$$

with the positive sign applied when the emitter moves towards the observer and the negative sign in the opposite case. In thermal equilibrium, the velocity distribution of the atoms is described by the Maxwell-Boltzmann distribution. Combining this with the Doppler effect leads to a Gaussian profile with a linewidth of

$$\Delta\nu_D = \nu_0 \sqrt{\frac{2k_B T}{mc^2}}. \quad (2.25)$$

To obtain the line shape of a power- and Doppler-broadened peak, a convolution of a saturated Lorentzian and a Gaussian profile has to be performed. This convolution of a Lorentzian and Gaussian is known as the Voigt profile which can be evaluated numerically, and its linewidth can be approximated by [34]

$$\Delta\nu_V = 0.5346\Delta\nu_L \sqrt{0.2166\Delta\nu_L^2 + \Delta\nu_G^2} \quad (2.26)$$

with $\Delta\nu_L$ and $\Delta\nu_G$ the Lorentzian and Gaussian linewidth, respectively.

Furthermore, broadening due to collisions between atoms can be observed. Similar to power broadening, this broadening arises due to a reduction of the upper state lifetime [35]. In this work however, so-called collisional or pressure broadening will not be discussed further. More details on this, and spectral line shapes in general, can be found in e.g. [35].

2.4 Nuclear theory

The fundamental constituents of atomic nuclei are quarks, grouped together in protons and neutrons. The strong interaction, the force between quarks mediated by gluons, is described using the Quantum Chromodynamics (QCD) theory. QCD cannot be applied to nuclei however, as quarks and gluons are not appropriate degrees of freedom on the energy scale of nuclear physics phenomena. Instead, a variety of effective theories have been developed with the aim of solving the nuclear many-body problem. These include *ab initio* based methods, microscopic-macroscopic models, configuration interaction techniques such as the phenomenological shell-model, and density functional theory as well as other mean-field based models. The microscopic-macroscopic semi-classical approach is the most intuitive, being based on a (macroscopic) liquid-drop model corrected with microscopic aspects from the shell model. An overview of the applicability of the other three methods throughout the nuclear chart can be seen in Fig. 2.2.

Ab initio methods start from first principles, which means using protons and neutrons as degrees of freedom, and a realistic interaction deduced from nucleon-nucleon scattering data and other few-body observables [38–43]. In principle, this should allow the nuclear structure (and reactions) to be computed for any nucleus. In practice however, available computing power limits the application of *ab initio* methods to nuclei up to $Z \approx 28$ [44] and some medium-mass nuclei close to shell closures [45, 46].

In the phenomenological shell-model approach, this limitation is partially overcome by defining an inert core and a valence space above [47]. Only the particles inside the valence space are active, while particles in the inert core do not participate in the dynamics and orbitals above the valence space are kept empty. Commonly, the valence space is taken to be a set of orbitals between two shell closures and the used interaction is phenomenologically adjusted to the chosen valence space. For most heavy nuclei and mid-shell regions, the valence space is however still too large to be computationally feasible [48].

Nuclear Density Functional Theory (DFT) can be applied throughout the whole

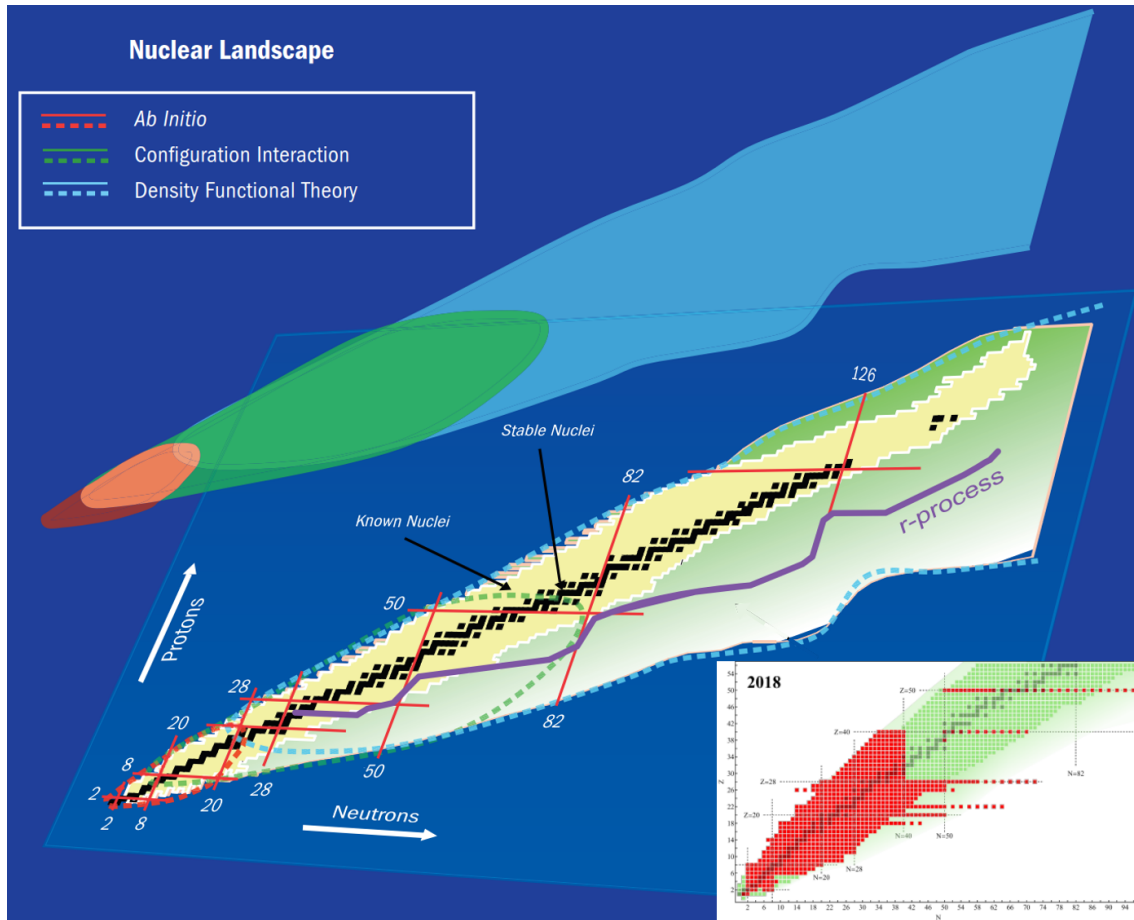


FIGURE 2.2 Main theoretical approaches to solving the nuclear many-body problem up to 2007, from [36]. The red lines denote the magic numbers. *Ab initio* based methods have by now been extended to $Z \approx 28$ and around the $Z = 40, 50$ shell closures, as shown in red in the bottom inset, taken from [37] based on work by H. Hergert [38]. Reproduced with permission of the authors, W. Nazarewicz and K. Hebeler, respectively.

nuclear chart. As this is the method used to compare to the experimental results obtained in this work, it will be discussed in some more detail in the following sections.

2.4.1 Nuclear mean field

As explained in the previous section, an approach to the nuclear many-body problem where all nucleons can interact with any other nucleon is unfeasible for most nuclei. A simplified picture is needed as a starting point, and to this end the concept of a mean field can be introduced, which is widely used in physics (and physical chemistry) for different kinds of many-fermion systems. The basic underlying assumption in the case of nuclei is that the nucleons move independently in an average potential created by other nucleons.

The first application of this idea was in the development of the shell model [49],

aimed at reproducing the experimentally observed *magic numbers* of protons and/or neutrons where nuclei are more stable. The mean-field potential in the shell model consists of the Woods-Saxon potential [50] with spin-orbit coupling and a Coulomb interaction term for protons.

Instead of this phenomenological approach however, the mean field can also be calculated self-consistently, in which the mean-field potential is obtained from the underlying nucleon-nucleon interaction. The so-called Hartree-Fock (HF) method [51, 52] allows the Schrödinger equation of the system to be solved via a variational principle in which the trial wave functions are Slater determinants Φ , composed of single-particle wave functions ϕ_i . This leads to a set of equations determining the single-particle energies ϵ_i , which in coordinate space can be written as

$$\left[-\frac{\hbar^2}{2m} \nabla^2 + \Gamma_H(\mathbf{r}) \right] \phi_i(\mathbf{r}) + \int d\mathbf{r}' \Gamma_{Ex}(\mathbf{r}, \mathbf{r}') \phi_i(\mathbf{r}') = \epsilon_i \phi_i(\mathbf{r}), \quad (2.27)$$

omitting spin and isospin degrees of freedom. Here the direct (Γ_H) and exchange (Γ_{Ex}) potentials constitute the mean field, and depend on the matter density ρ and the nucleon-nucleon interaction $V(\mathbf{r}, \mathbf{r}')$. The density in turn depends on the single-particle wave functions, which are the solutions of the HF equations. The mean field obtained in this way is said to be self-consistent as it depends on its own solution. The iteration to minimise the binding energy of the system, given by the HF energy $E_{HF} = \langle \Phi | H | \Phi \rangle$, starts with an initial guess for the mean field Γ . This leads to the single-particle wave functions ϕ_i which determine the density ρ and energy E_{HF} . The obtained solution is then used to construct a new mean field Γ until the iteration converges to minimal binding energy.

In order to approximate pairing correlations in the HF method, the Bardeen, Cooper and Schrieffer (BCS) method [53] can be used. More commonly used nowadays is the full Hartree-Fock-Bogoliubov (HFB) approach [54], to account properly for pairing correlations.

2.4.2 Nuclear density functional theory

By introducing a density-dependent effective nucleon-nucleon interaction in the HF method, the HF energy can be written in terms of an Energy Density Functional (EDF). In a general way, this can be written as

$$E = \langle \Phi | H[\rho] | \Phi \rangle = \int \mathcal{E}(\mathbf{r}) d^3\mathbf{r} \quad (2.28)$$

where \mathcal{E} is the EDF, a function of local densities. In the DFT picture, the EDF encodes complicated many-body correlations into the form of nucleonic densities and currents. One commonly used effective nucleon-nucleon interaction is the

zero-range Skyrme force [55]

$$\begin{aligned}
V_{Skyrme}(\mathbf{r}_{12}) = & t_0(1 + x_0P_\sigma)\delta(\mathbf{r}_{12}) + \frac{1}{2}t_1(1 + x_1P_\sigma) \left(\mathbf{k}^{\dagger 2}\delta(\mathbf{r}_{12}) + \delta(\mathbf{r}_{12})\mathbf{k}^2 \right) \\
& + t_2(1 + x_2P_\sigma)\mathbf{k}^\dagger \cdot \delta(\mathbf{r}_{12})\mathbf{k} + \frac{1}{6}t_3(1 + x_3P_\sigma)\delta(\mathbf{r}_{12})\rho^\alpha \\
& + iW_0(\boldsymbol{\sigma}_1 + \boldsymbol{\sigma}_2) \cdot (\mathbf{k}^\dagger \times \delta(\mathbf{r}_{12})\mathbf{k})
\end{aligned} \tag{2.29}$$

where $\mathbf{r}_{12} = \mathbf{r}_1 - \mathbf{r}_2$, $\mathbf{k} = -i(\nabla_1 - \nabla_2)/2$ is the relative momentum operator, P_σ is the spin-exchange operator, $\boldsymbol{\sigma}_i$ are the Pauli spin matrices, and t_i , x_i , W_0 are 10 free parameters. Using this force as a generator to obtain the Skyrme EDF leads to the total binding energy given by [56]

$$E^{Sk} = E_{kin} + \int d^3r \mathcal{E}_T^{Sk} + E_{Coul} + E_{pair}, \tag{2.30}$$

composed of the sum of the kinetic energy, the Skyrme energy density functional, the Coulomb energy, and the pairing energy. The time-even part of the Skyrme EDF can be written in terms of the particle density ρ_T , kinetic density τ_T , and spin-orbit current \mathbf{J}_T

$$\mathcal{E}_T^{Sk,even} = C_T^\rho(\rho)\rho_T^2 + C_T^\tau\rho_T\tau_T + C_T^{\Delta\rho}\rho_T\Delta\rho_T + C_T^{\nabla J}\rho_T\nabla \cdot \mathbf{J}_T + C_T^J\mathbf{J}_T^2 \tag{2.31}$$

with C_T^i free parameters that need to be fitted to empirical input. The time-even part is the only one contributing to stationary calculations of even-even nuclei. The time-odd part contains all dependencies on the spin density \mathbf{s} , current density \mathbf{j} , and spin kinetic density \mathbf{T} . These time-odd terms need to appear in bilinear form to render the full functional time-reversal invariant. Each part in itself consists of an isoscalar part with isospin $T = 0$ and an isovector $T = 1$, $\mathcal{E}_T^{Sk} = \mathcal{E}_0^{Sk} + \mathcal{E}_1^{Sk}$. Isoscalar densities are total densities (e.g. $\rho_0 = \rho_n + \rho_p$), while isovector densities account for proton-neutron differences (e.g. $\rho_1 = \rho_n - \rho_p$).

Typical experimental input to constrain the free parameters in Eq. 2.31 includes nuclear binding energies, charge radii, odd-even staggering values for the pairing gap, and single-particle energies. Different types of observables are required to constrain the model parameters, because if some quantities are neglected, the resulting EDF may have poorer predictive power for these quantities. Several parameter sets have been developed over the years, such as SKM* [57], SLy4 [58] and SV-min [59]. There are also the UNEDF Skyrme models, where the original UNEDF0 [60] has been improved for large deformation with the UNEDF1 parameterisation [61], and further adjustments for shell structure were done in UNEDF2 [62].

Another often used effective interaction to generate an EDF is the finite-range Gogny force [63], constructed from two Gaussians, a density-dependent contact term and spin-orbit interaction term. This interaction has 14 free parameters that

need to be adjusted. Several parameterisations exist for this class of EDFs as well, such as D1S [64], D1N [65], and D1M [66].

A density-dependent force is just one way to generate an energy functional however. An EDF can also be directly parameterised in terms of local densities, without any reference to an underlying interaction. This goes back to the original way DFT was introduced, by the Hohenberg-Kohn theorem [67] and Kohn-Sham equations [68]. Originally these theorems were introduced for the electronic structure, but nowadays they are widely used in the field of quantum many-body physics, including nuclear physics. The Hohenberg-Kohn theorem states that the ground-state properties of a many-electron system are uniquely determined by the density, and there exists a function of the density which reproduces the ground-state energy exactly. The same function works for any electronic system. The Kohn-Sham equations map the problem to a non-interacting system, in which particles move independently in the effective Kohn-Sham potential which is obtained from a variation of the energy density. This is now in essence equivalent to the HF picture.

One class of EDFs that are not directly based on an underlying effective force is the Fayans functionals. In general, the total binding energy can be written as [69]

$$E^{Fy} = E_{kin} + \int d^3r \mathcal{E}^{Fy} + E_{Coul} + E_{pair} \quad (2.32)$$

with the Fayans EDF composed of three terms, a volume term, a surface term and a spin-orbit term:

$$\mathcal{E}^{Fy} = \mathcal{E}^v + \mathcal{E}^s + \mathcal{E}^{ls}. \quad (2.33)$$

Compared to Skyrme functionals, Fayans EDFs have a more complex dependency on particle densities. The kinetic energy and Coulomb terms in Eq. 2.32 are exactly the same as in the Skyrme model. The pairing energy however is determined by a pairing energy density functional which contains a density-gradient term not present in Skyrme models. This term is supposed to effectively account for the coupling to surface vibrations and is essential for explaining the odd-even staggering of charge radii [70,71]. Besides the original form and parameterisation FaNDF⁰ [69], slightly different versions and parameterisations have been developed, such as DF3 [71,72] and DF3-a [73]. Recent developments have led to the introduction of Fy(std) [74] and Fy(Δr , HFB) [75].

It must be mentioned that only the non-relativistic treatment has been discussed here. There exist self-consistent relativistic mean-field models (also known as covariant EDF models), where the mean field is solved from the Dirac equation. As these were not used in this work, they will not be considered here, but an overview can be found in [76].

3 FREQUENCY DETERMINATION AND STABILISATION USING FABRY-PÉROT INTERFEROMETERS AND SATURATED ABSORPTION SPECTROSCOPY

In any laser spectroscopy experiment, determination of the laser frequency, and possibly frequency stabilisation, are crucial to be fully controlled and any related systematic uncertainties to be understood. In this technical chapter, extensive work to this end for the laser spectroscopy experiments conducted at IGISOL, using in-source/in-gas-cell resonance ionisation and collinear laser spectroscopy, is presented. This work was mainly based on a saturated absorption spectroscopy setup and several Fabry-Pérot Interferometers (FPIs).

The chapter starts with an explanation of the saturated absorption spectroscopy technique, and subsequently a description of the setup. The third section, on FPI free spectral range calibration required for reliable frequency determination, is largely a summary of the work done in included Article [PI]. The next section is a follow-up from this work, and details the effort to temperature stabilise an FPI in order to reduce systematic errors. Lastly, frequency stabilisation of a continuous-wave laser was investigated, as this is necessary for collinear laser spectroscopy.

3.1 Saturated absorption spectroscopy technique

Saturated absorption spectroscopy is one of many high-resolution laser spectroscopy techniques, described in e.g. [77]. It is a so-called *Doppler-free* technique as the effect of Doppler broadening on the achievable atomic transition linewidth can be eliminated. This is done by the use of two counter-propagating laser beams;

a relatively high intensity pump beam and a weak probe beam, with the same frequency ν (usually originating from the same laser). When passing through an atomic vapour with a Maxwell-Boltzmann velocity distribution, the probe beam will be absorbed by atoms with a longitudinal velocity component of

$$v_z = \frac{(\nu - \nu_0)c}{\nu_0} \quad (3.1)$$

in the non-relativistic limit, with ν_0 the transition frequency. The pump beam will be absorbed by atoms of the opposite velocity class. At $\nu = \nu_0$ however, both beams are absorbed by the same atoms with $v_z = 0$, which move perpendicular to the laser beams. The strong pump beam will excite many atoms, approximately until the point of saturation (defined by an equal number of atoms in the ground and excited state), causing a decreased population of the ground state. This so-called *hole burning* in the ground state population leads to a drop in the total absorption of the probe beam at ν_0 called the *Lamb dip*, which is the main feature detected in saturated absorption spectroscopy. A simple illustration of the hole burning and Lamb dip can be seen in Fig. 3.1. The linewidth of the Lamb dip is mainly dependent on the power broadening caused by the pump and probe beam, and can approach the natural linewidth of the transition, see Eq. 2.22.

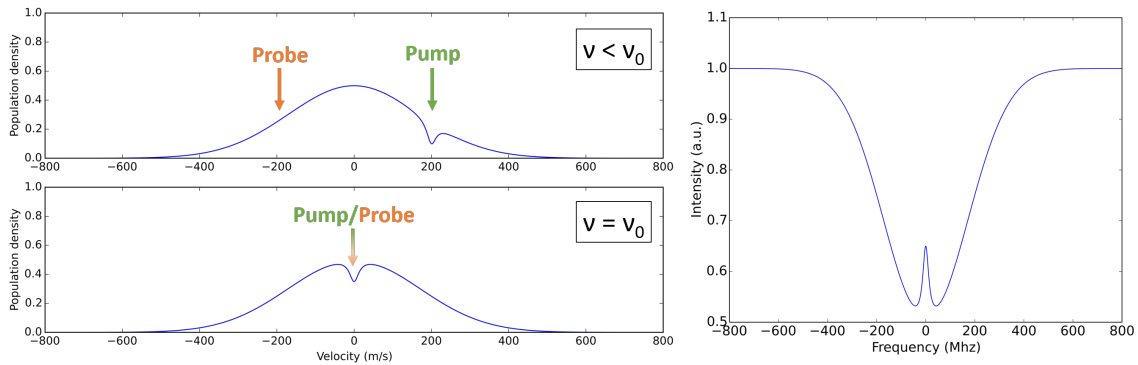


FIGURE 3.1 Hole burning in the ground state population (left) and the resulting (Doppler-broadened) absorption spectrum of the probe beam showing the Lamb dip (right).

In order to account for fluctuations in overall laser power, a third beam with an equal power fraction as the probe beam can be split off, called the reference beam. This beam goes through the atomic vapour without overlapping the pump beam. Subtracting the reference signal from the probe signal yields a saturation spectrum with only the Lamb dips visible.

In a system with more than two atomic states, so-called crossover lines can occur when two Doppler-broadened transitions with a common lower or upper level partially overlap. At a laser frequency of $\nu_{12} = \frac{\nu_1 + \nu_2}{2}$, atoms with a longitudinal velocity of $v_z = \frac{(\nu_2 - \nu_1)c}{2\nu_{12}}$ are resonant with the pump beam on transition 1, and with the probe on transition 2. This yields a crossover signal at ν_{12} in addition to the saturation signals at ν_1 and ν_2 [77].

In the case of a hyperfine structure with several atomic level splittings and corresponding transitions, the small scale of the splittings can give rise to many crossover signals, possibly with optical pumping effects in between levels [78,79]. This may lead to increased absorption of the probe beam instead of decreased absorption at crossover frequency points, showing up as negative peaks in the saturation spectrum. An example of this can be seen in Fig. 3.2, which shows the saturated absorption spectrum of the D2 line at 780.24 nm in natural rubidium, i.e. ^{85}Rb and ^{87}Rb , recorded with a lock-in amplifier. The fit to the saturated absorption spectrum (in orange) exhibits excellent agreement with literature values for the hyperfine parameters [80,81]. In the right-most multiplet, the high-frequency multiplet of ^{87}Rb , a negative crossover peak at an intensity of $-0.25(5)$ V can be seen. The occurrence of these crossover signals and optical pumping effects complicates the spectrum, which is why either laboratory conditions are controlled to have a handle on this (e.g. magnetic shielding), or transitions with less closely spaced hyperfine levels are chosen for certain applications. For example, the D1 line in Rb was used for the Free Spectral Range (FSR) calibration of a Fabry-Pérot Interferometer (FPI) discussed in the next section.

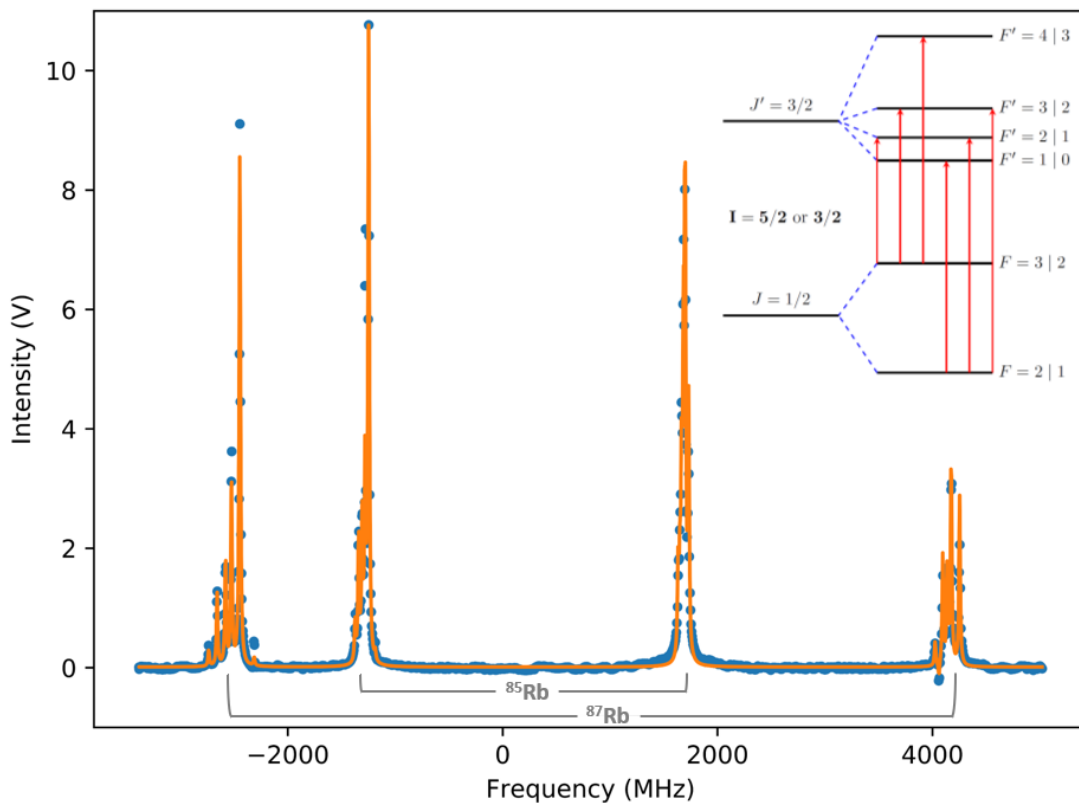


FIGURE 3.2 Hyperfine structure with crossover signals on the D2 line of ^{85}Rb (middle multiplets) and ^{87}Rb (outer multiplets) recorded with a lock-in amplifier (output in volts). Fit to the saturated spectrum in orange. Inset shows a schematic of the transitions, with the splittings not to scale. Of note is the negative crossover peak in the right-most multiplet.

Saturated absorption spectroscopy has been used in the past for the determination of transition frequencies, isotope shifts and hyperfine structure constants, see e.g. [82,83]. It is now mainly used to provide precise and stable frequency standards to be used for frequency calibration or stabilisation of lasers [84].

3.2 Setup

A schematic of the most recent version of the cw laser cabin setup can be seen in Fig. 3.3. A detailed description of most components can be found in included Article [PI], which is focused on activities with this setup. The work was started as part of a M.Sc thesis [85], with optimisation and application during this PhD thesis. In this section a short overview will be given, as well as some updates that were added after the work of Article [PI].

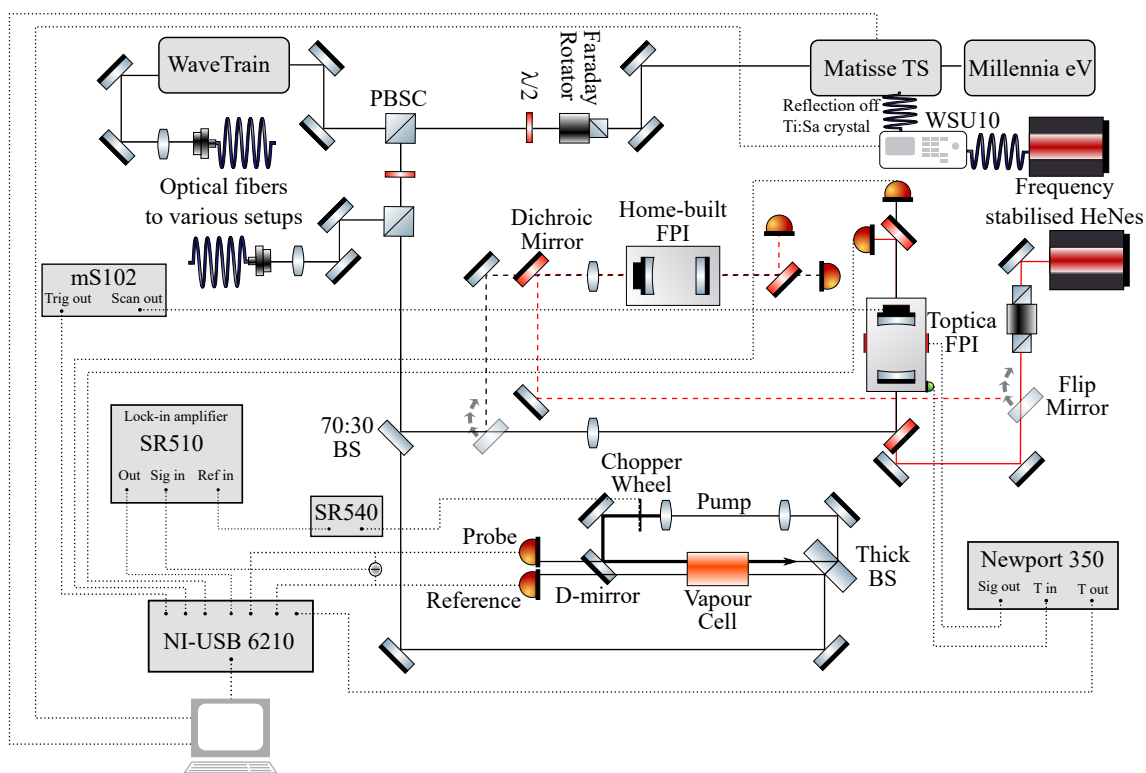


FIGURE 3.3 Schematic of the cw laser system, the saturated absorption spectroscopy setup and two FPIs, with accompanying data acquisition system. The ramp generator (Miniscan 102) and photodiodes can be connected to either FPI as required. The additions since Article [PI] are the WaveTrain 2 doubling unit, WSU-10 wavemeter with frequency-stabilised HeNe and the temperature stabilisation of the Toptica FPI.

The main laser is a continuous wave (cw) Ti:sapphire laser (Sirah Matisse TS) pumped by a 6W Millennia eV laser. A reflection off the Ti:sapphire crystal is used as an input for the HighFinesse WSU-10 wavemeter (specified 10 MHz absolute

uncertainty), which has a frequency-stabilised HeNe laser (Thorlabs HRS015B) fiber coupled for continuous calibration. The Ti:sapphire output is split up in three beams by two polarising beam splitter cubes (PBSC) with the power fraction controlled by $\lambda/2$ waveplates. One of the beams is fiber coupled to serve e.g. as a master laser for an injection-locked pulsed Ti:sapphire laser [86]. Another beam can be frequency-doubled with the use of the frequency doubling unit, a WaveTrain 2.

The last beam is sent to the experimental setup, being split up again, with 70% going to the saturated absorption spectroscopy setup and 30% to the FPIs. As mentioned in the previous section, a pump, probe and reference beam are needed for saturated absorption spectroscopy, which are created here with the use of an uncoated thick glass beam splitter. The atomic vapour in the vapour cell consists of either natural rubidium (72.168% ^{85}Rb and 27.835% ^{87}Rb) or cesium (^{133}Cs). When Rb is used, a heating controller is installed around the vapour cell to avoid the considerable condensation present at room temperature.

Probe and reference beams are recorded using photodiodes, and their electronically generated difference is used as an input for the lock-in amplifier. In conjunction with the lock-in amplifier, modulation of the pump beam by a chopper wheel is required. The lock-in amplifier [87] and chopper wheel were installed to provide background-free saturated absorption spectra, as previously there had been issues with background noise due to power fluctuations and imbalances in the photodiodes. Typical used chopper frequencies are on the order of 400 Hz, at the low end of the minimum noise regime identified in the lab [88].

The 30% fraction of the Ti:sapphire laser beam is sent to one of two scanning FPIs together with a frequency-stabilised HeNe laser (Melles Griot, 25-STP-912-230). One FPI is home-built [89] and the other is a confocal commercial Toptica FPI-100-0750-1 with an FSR of ~ 1 GHz and a Finesse of < 400 . A ramp generator (Toptica, Miniscan 102) provides voltage scanning of the piezo mirror for both FPIs. Dichroic mirrors are used to combine and split up the Ti:sapphire and HeNe beams, which are then detected on photodiodes. A temperature controller (Newport model 350) is used to stabilise the temperature of the Toptica FPI using Peltier elements. More details on the temperature stabilisation follow in section 3.4.

Seven signals in total are connected to the data acquisition hardware module (NI USB-6210): the photodiode signals from both probe and reference beam, the FPI photodiode signals of the HeNe and Ti:sapphire, the lock-in amplifier output, the temperature readout from the temperature controller and the trigger signal of the ramp generator. Data acquisition and real-time visualisation are handled in LabVIEWTM.

As a test of the setup, with a focus on the newest installations discussed here, saturated absorption spectroscopy was performed on the 387.92 nm transition in ^{133}Cs from the ground state $6s^2S_{1/2}$ to the $8p^2S_{3/2}$ state, using the WaveTrain to generate the second harmonic of the 775.84 nm Ti:sapphire beam. A total of 21 spectra were taken, using the WSU-10 wavemeter for wavelength recording and the lock-in amplifier to maximise the signal-to-noise. All spectra were binned and averaged together to create the spectrum seen in Fig. 3.4. Many spectra were needed as this is a rather weak transition, $A = 3.86 \cdot 10^5$ 1/s [90]. This is also reflected in the Lorentzian linewidth of the saturated absorption spectrum, which is 11 MHz. Due to the small hyperfine parameters of the upper state and the crossover signals the components are still not fully resolved however. Therefore the hyperfine B parameter of the upper state was fixed to the literature value of 0.14 MHz [91]. The fitted hyperfine A parameters show good agreement with literature: $A_{l,fit} = 2299.4(3)$ MHz compared to $A_{l,lit} = 2298.158$ MHz [92]; $A_{u,fit} = 8.1(1)$ MHz compared to $A_{u,lit} = 7.42(6)$ MHz [91]. An attempt was made to measure the hyperfine structure of this transition with the collinear laser spectroscopy setup (see next chapter), however the transition proved too weak to detect.

3.3 FPI Free Spectral Range calibration

One of the main purposes of the saturated absorption spectroscopy setup built at the IGISOL facility was the determination of the FSR of FPIs, currently a home-built FPI and a commercial Toptica FPI. These FPIs can be used for reliable wavelength determination in laser spectroscopy experiments when laser frequency scanning is involved, e.g. in-source or in-gas-jet resonance ionisation spectroscopy. To measure these frequency changes accurately the FSR of the interferometers must be determined as precisely as possible. The most common method is via calibration against an atomic transition with a well-known hyperfine structure; in this work provided by the saturated absorption spectroscopy setup.

The full calibration procedure and results of the FSRs of the home-built and commercial FPI are described in Article [PI]. In short, the first step is to convert the recorded time to a scale in number of FSR. This is realised by identifying the HeNe and Ti:sapphire fringe positions in each FPI scan, the scans being separated by ramp trigger signals. A linearising fit (third degree polynomial) is applied to the HeNe fringe positions to account for the non-linearity of the piezo scanning. The fit results are then used to convert the Ti:sapphire fringe positions to the number of FSRs scanned. Several Ti:sapphire fringes per FPI scan are tracked over the span of a full spectrum, including jumps in the transmission order when a Ti:sapphire fringe moves by more than half an FSR from its reference HeNe fringe.

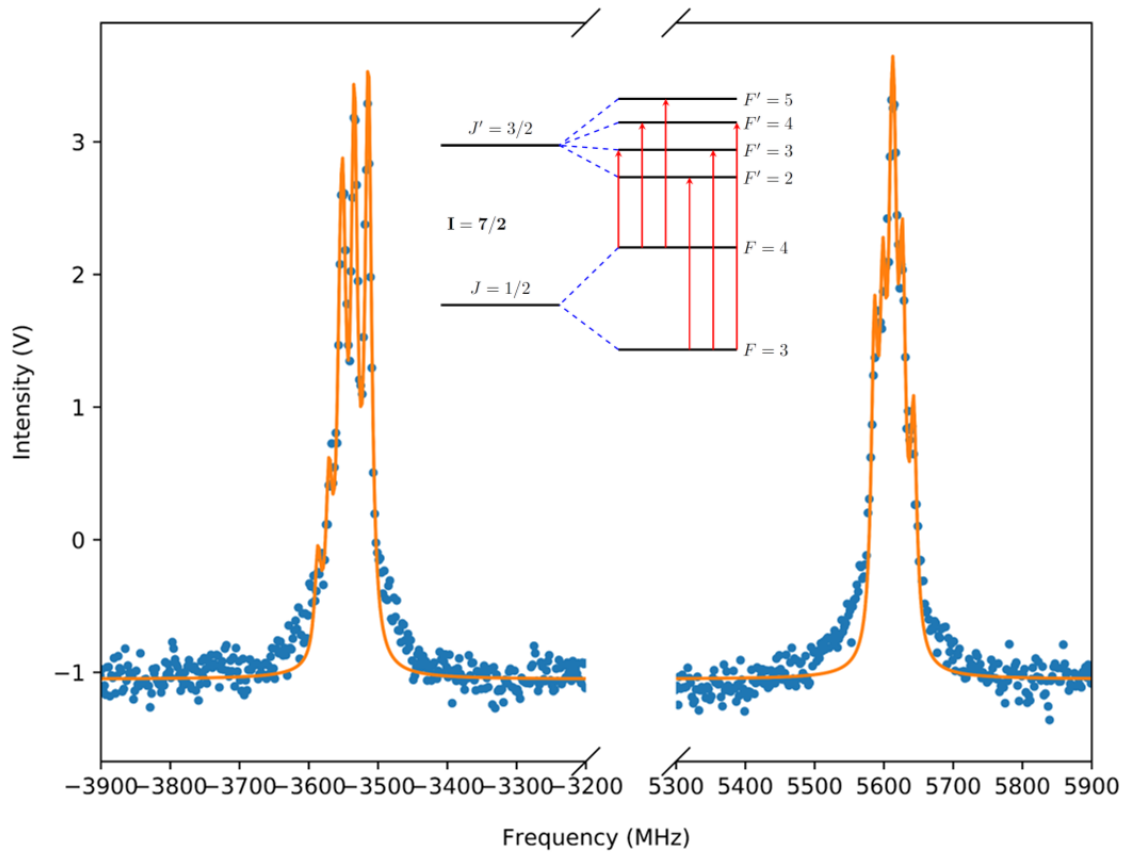


FIGURE 3.4 Saturated absorption spectrum of ^{133}Cs on the 387.92 nm transition, $6s^2S_{1/2} \rightarrow 8p^2S_{3/2}$. Inset shows a schematic of the transition, splittings not to scale. Hyperfine structure fit including crossover signals is shown in orange. The Doppler-broadened pedestal creating wings on the multiplets, arising due to minimal interaction of the pump with the reference beam, is not included in the fit.

A hyperfine spectrum can then be plotted from the lock-in amplifier signal versus the obtained number of scanned FSRs. The hyperfine structure is fitted with all hyperfine parameters fixed to the well-known literature values but multiplied by a free-running common scaling factor. The inverse of this scaling factor is an accurate measure of the value of the FSR in frequency units.

This procedure resulted in a measured FSR of 0.998836(13)[4000] GHz for the Toptica FPI and 3.46571(5)[500] GHz for the home-built FPI. The calibrated Toptica FPI has been used in high-resolution resonance ionisation spectroscopy of copper using a new pulsed injection-locked Ti:sapphire laser [86].

3.4 Temperature stabilisation

A remaining issue noticed during the FSR calibration was the rather large systematic uncertainty on the FSR of both FPIs (4 and 5 MHz) due to temperature fluctuations within the laser cabin. The systematic errors are related to the uncompensated non-linearity. They are quantified using the difference between the number of FSRs obtained for each Ti:sapphire fringe from the linearising cubic polynomial fit, which should be equal to one, but deviates due to the remaining non-linearity (see Fig. 6 in Article [PI]). The average of these deviations for each FPI scan is assigned to the spectrum, and the overall average of the values for the used spectra is assigned as the systematic error on the FSR. The more unstable the HeNe fringe positions are, the less reliable the linearisation becomes and thus the larger the remaining residuals. In Fig. 3.5 the effect of the temperature on the FPI fringe locations is clearly visible, with a periodic fluctuation of about $0.2\text{ }^{\circ}\text{C}$ due to the air conditioning unit in the laser cabin. This leads to a 50 ms periodic fluctuation in the fringe locations.

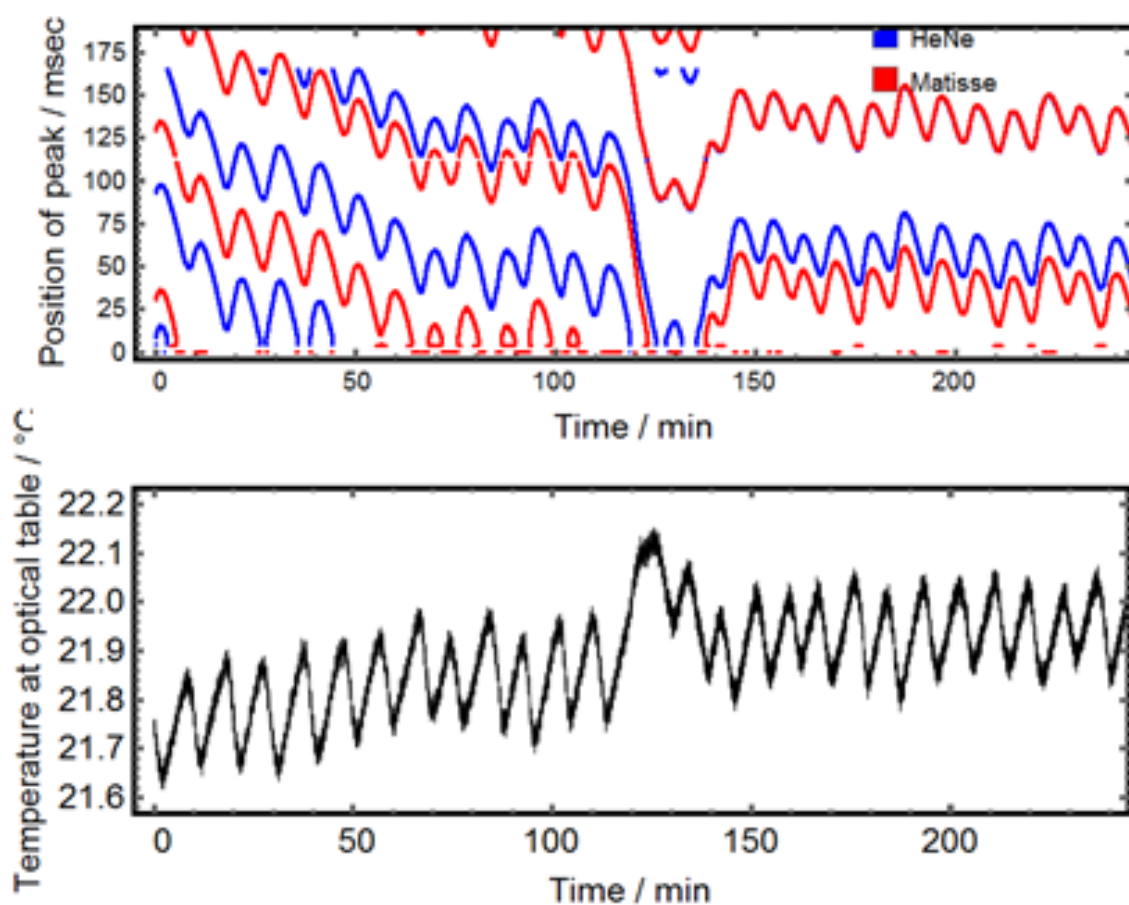


FIGURE 3.5 Effect of the room temperature on the FPI peak locations. Upper panel shows the position of both the HeNe and Ti:sapphire fringe locations, bottom panel the recorded room temperature. Figure courtesy of R. Terabayashi.

In order to try to isolate the FPI from the environment, a setup was built using a metal box surrounding the commercial 1 GHz Toptica FPI with two Thorlabs TEC3-6 Peltier elements attached on either side of the box, which was then shielded with insulation foam. A Thorlabs TH10K thermocouple was directly attached to the FPI, and the readout was used for the feedback loop provided by the Newport model 350 temperature controller (see Fig. 3.3). This maintains a temperature stability within ± 0.01 °C or better, as can be seen in the upper panel of Fig. 3.6. Following this implementation, there no longer appears to be any correlation between the cabin temperature and the HeNe fringe position, so the remaining drifting is likely to be due to other effects such as small pressure differences. Instability of the HeNe laser frequency would also cause drifting, but this can be ruled out as the spacing between the Ti:sapphire and HeNe fringes stayed constant, as seen in the bottom panel of Fig. 3.6, meaning both are drifting identically.

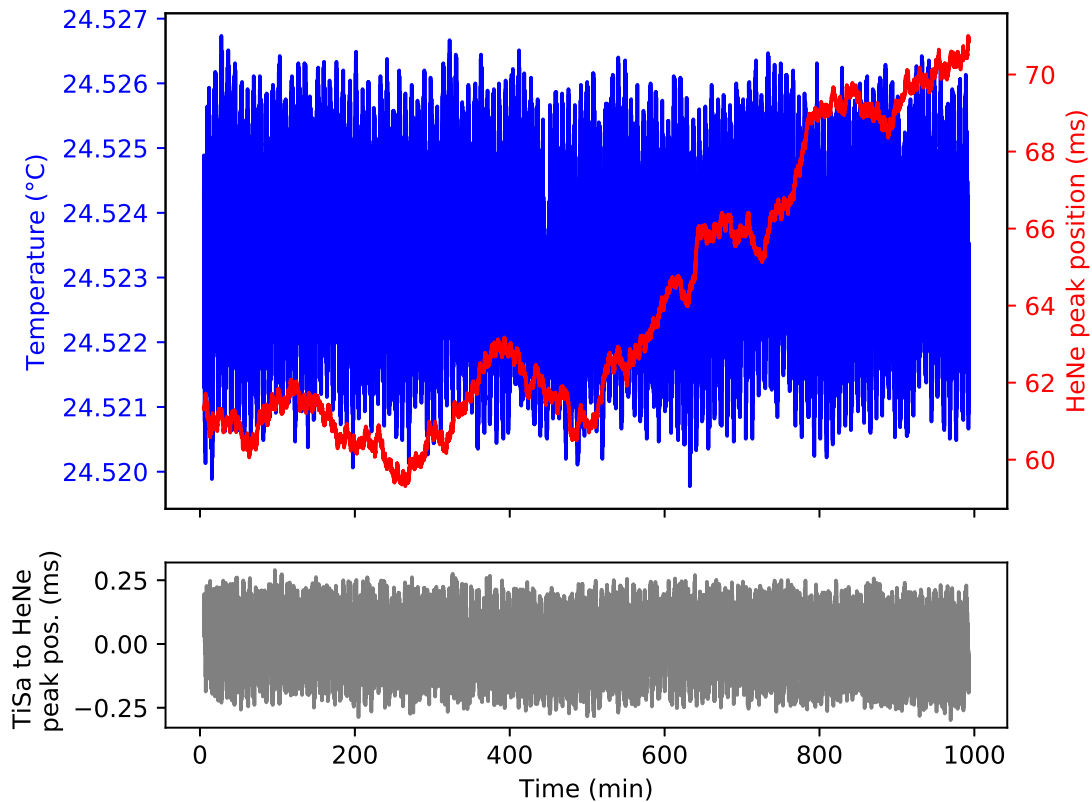


FIGURE 3.6 Stabilised temperature of the Toptica FPI, recorded position of one HeNe fringe (upper) and relative position of a Ti:sapphire fringe to the HeNe fringe (lower) over about 16.5 hours. The temperature is stable to within ± 0.004 °C.

Comparing figures 3.5 and 3.6 show that from a periodic fluctuation with an amplitude of about 50 ms and additional long-term drifts, the fluctuation is reduced to only about 10 ms over a longer time period. The FSR was remeasured using the same procedure described in section 3.3, leading to the same absolute value but with a reduced systematic error of 1.9 MHz instead of 4 MHz without temperature

stabilisation. This remaining systematic uncertainty is thought to now be fully dominated by non-linearities in the scanning of the piezo mirror of the FPI, and no longer by (large) changes in the fringe positions due to temperature instabilities.

3.5 Frequency stabilisation

The saturated absorption spectroscopy setup was also used to investigate long-term frequency stabilisation of the Matisse Ti:sapphire laser. This was done in preparation for use of the Ti:sapphire laser for collinear laser spectroscopy. Side-of-fringe locking was used, which utilises the slope on either side of a reference peak to convert frequency fluctuations of the laser into amplitude fluctuations. Here the reference peak was chosen to be the strongest component in the ^{85}Rb hyperfine structure of the D1 line, with the setpoint at half the peak height, as is shown on the left of Fig. 3.7. The difference between the setpoint value and the photodiode readout after lock-in amplification is then converted to a feedback voltage fed to the piezo mirror of the Matisse reference cavity via a PID loop. This was set up using a self-written LabVIEWTM programme, which then communicates with the Matisse control through the Matisse Commander software which is also LabVIEWTM based¹.

The LabVIEWTM standard PID algorithm used to implement the voltage feedback loop $V(t)$ is

$$V(t) = K_c \left(e + \frac{1}{T_i} \int_0^t e dt + T_d \frac{de}{dt} \right) \quad (3.2)$$

where e is the error signal, i.e. the difference between the setpoint and the lock-in signal in volts, and K_c , T_i and T_d are the adjustable PID parameters [93]. Besides these parameters, there is also an adjustable loop time to determine the feedback frequency, and an average for the number of readout points used. The effect of all these parameters on the stability and resulting frequency spread of the lock was investigated to find the optimal set of parameters. The result can be found in Table 3.1. The critical parameter to the overall intensity of the feedback loop is K_c , the proportional parameter which also converts the error signal to the appropriate scale for the piezo mirror (from volts to millivolts). T_i , controlling the integral part, was also observed to be important to the linewidth of the lock, while T_d controlling the derivative part did not have a noticeable effect and was thus kept at zero. Increasing the average did not have a noticeable effect either, and was thus kept at 1. The loop time was optimized to obtain the most stable locking.

In Fig. 3.8 the resulting stability and linewidth of the lock can be seen. A comparison to the stability without stabilisation is made to demonstrate the drifting

¹ To be found at sirah.com/laser/cw-ring-lasers/matisse-commander-software

TABLE 3.1 Optimised parameters for locking the Matisse TS to a Rb hyperfine component using the PID loop described in Eq. 3.2.

Parameter	Optimal value
K_c	10^{-6}
T_i	0.04
T_d	0
Time	200 ms
Average	1

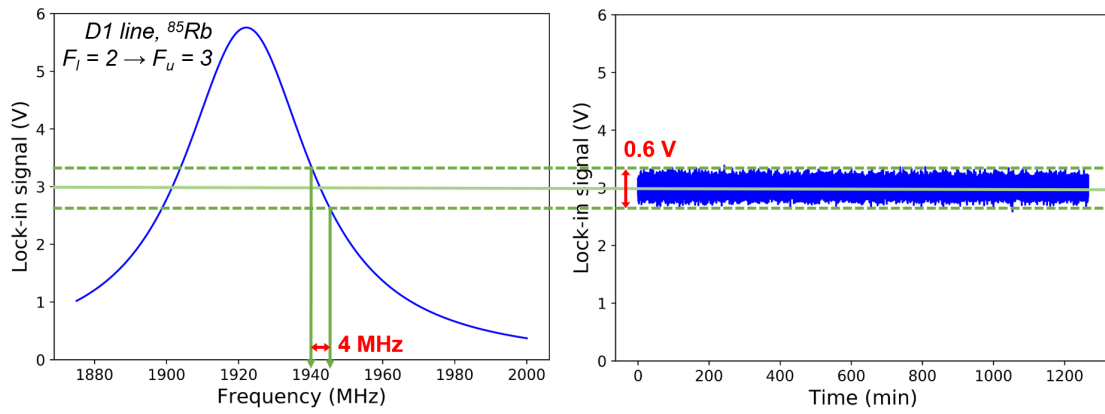


FIGURE 3.7 Illustration of the side-of-fringe locking and the conversion of the stability in volts to frequency.

that needs to be compensated. This drifting is due to environmental effects on the Matisse reference cavity which ensures only short-term stability, involving counteracting fast perturbations to reduce the effective laser linewidth. Using the read-out from the Toptica FPI, the voltage deviation can be converted to a frequency, as is illustrated in Fig. 3.7. A stability of ± 0.3 V is equal to ± 2 MHz.

The long-term frequency stabilisation was also studied using the WSU-10 wavemeter. The Matisse Commander software includes a plug-in named Counterdrift which communicates with HighFinesse wavemeters and implements a PID loop for frequency stabilisation. Optimisation of the PID parameters, at $I = 3$ and $P = D = 0$, i.e. fully integral controlled, led to a stable lock within ± 1 MHz, as can be seen in Fig. 3.9.

To test the accuracy and stability of the WSU-10 wavemeter, a cross-check of the two frequency stabilisation methods was performed. In a first test, the Ti:sapphire laser was stabilised to the wavemeter at a frequency on the side of a ^{85}Rb hyperfine peak. Any fluctuation in the wavemeter would be mirrored in the Ti:sapphire frequency and thus in the signal from the lock-in amplifier. The result can be seen in Figures 3.10a, 3.10b. Over a period of more than 24 hours, the signal shifted by only 1 V, which corresponds to about 3.2 MHz when calculating the frequency

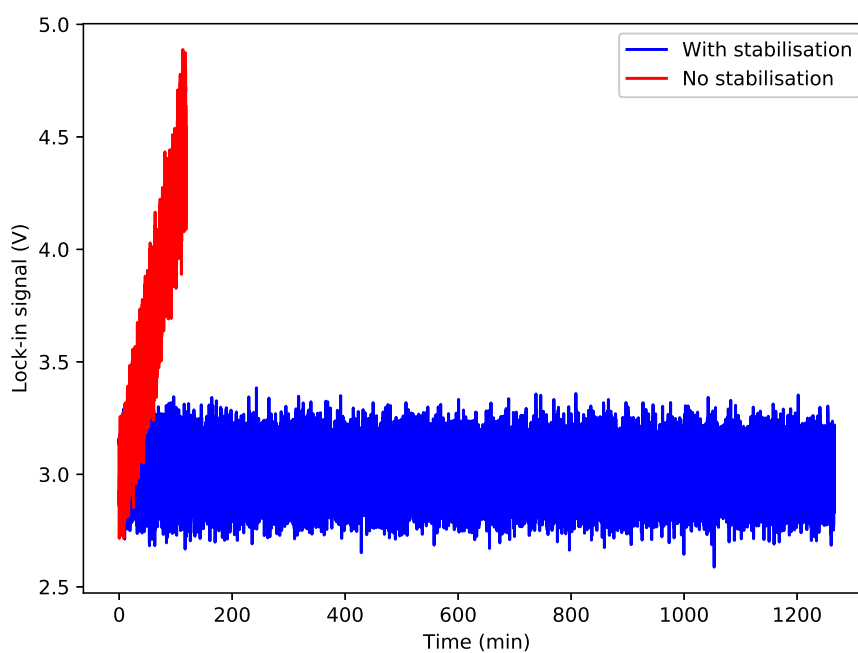


FIGURE 3.8 Comparison of laser frequency evolution with and without long-term frequency stabilisation to a ^{85}Rb transition.

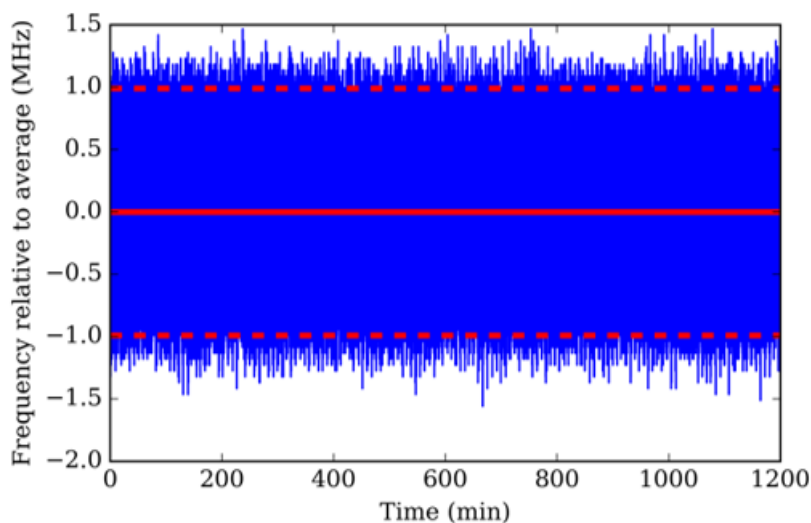


FIGURE 3.9 Best achieved long-term frequency stability when stabilising the Ti:sapphire laser to the WSU-10 wavemeter. The dotted lines at ± 1 MHz denote the 3σ band.

with the FPI. The opposite was also tested, i.e. stabilise the Matisse to a ^{85}Rb hyperfine peak and look for any drifts in the wavemeter readout. In Figures 3.10c, 3.10d the test where the largest shift was seen is shown, which is about 4 MHz over 24 hours.

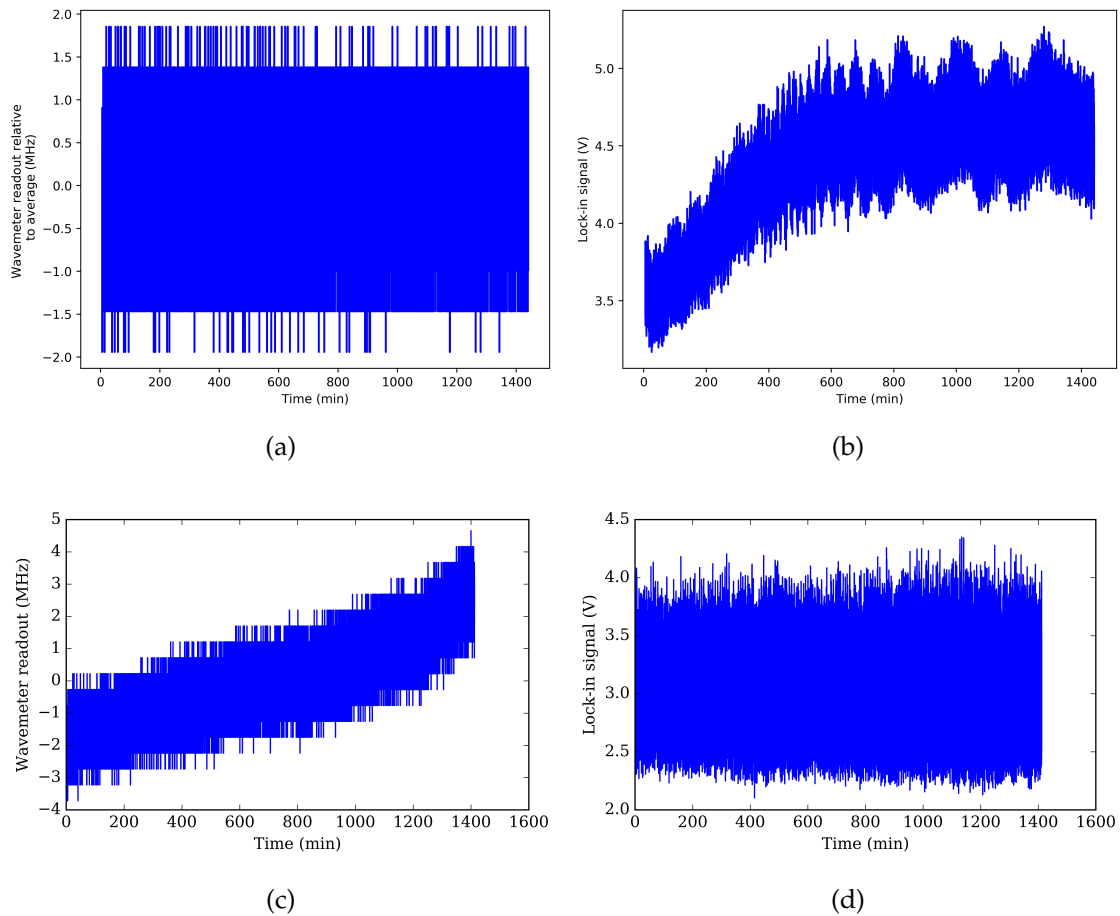


FIGURE 3.10 Monitoring of the wavemeter (left) and the saturated spectroscopy photodiode signals after lock-in amplification (right) when (a)-(b) the Ti:sapphire laser is stabilised to the wavemeter; (c)-(d) the Ti:sapphire laser is stabilised to a ^{85}Rb hyperfine peak. 1 V on the y-scale on the right corresponds to about 3.2 MHz. The apparent settling time in (b) is most likely a coincidence, as different patterns were seen in other tests and no correlation with e.g. time of day could be found.

3.6 Summary and outlook

This chapter presented extensive testing of frequency determination and stabilisation methods routinely used at IGISOL. The FSR of two scanning FPIs was measured, with a good understanding of the systematic errors involved. The excellent agreement with literature of hyperfine parameters in Rb, Cs (this work) and Cu [86] using the calibrated Toptica FPI puts further trust in the FSR determination. The Toptica FPI will continue to be used for experiments involving the injection-locked Ti:sapphire laser, while the home-built FPI is suitable for future in-source spectroscopy using e.g. a dual-etalon pulsed laser [94].

The frequency stabilisation tests were mainly done with an eye towards collinear laser spectroscopy experiments, where the laser frequency is kept fixed. The

Matisse cw Ti:sapphire laser and the WSU-10 wavemeter are part of a recent upgrade to the collinear laser spectroscopy laser system, which will be discussed in the next chapter. The experiments presented here give confidence in the stability and precision of the wavemeter for use in the stabilisation of cw laser systems.

As the frequency-stabilised HeNe lasers are crucial as a frequency reference in all these applications, a measurement of their long-term stability was performed with the wavemeter, see Fig. 3.11. The Melles Griot 05-STP-912 HeNe laser, used in the work of Article [PI], is stable to within about ± 4 MHz over 24 hours (specified: 1-8 hours ± 1 MHz, 8 hours ± 2 MHz, 1 month ± 3 MHz). The Thorlabs HRS015B HeNe laser acquired together with the WSU-10 wavemeter is stable to within 1.5 MHz over 20 hours (specified: 1 min ± 1 MHz, 1 hour ± 2 MHz, 8 hours ± 3 MHz). The Melles Griot HeNe laser will continue to be used mainly in conjunction with the FPIs, while the Thorlabs HeNe laser will serve as a calibration source for the wavemeter and other applications in the collinear laser spectroscopy laser cabin.

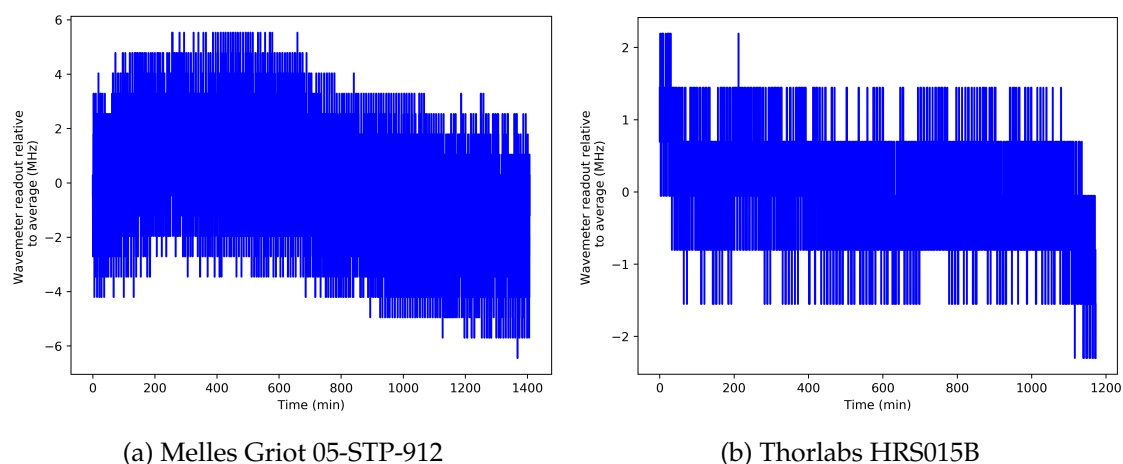


FIGURE 3.11 Monitoring of the frequency-stabilised HeNe lasers used in the cw laser cabin, illustrated in Fig. 3.3.

As the Thorlabs HeNe laser still shows some drifting, an even more stable frequency reference would be desirable. With this in mind, some tests will be done in the near future in the collinear laser cabin using the saturated absorption spectroscopy setup. The Matisse cw Ti:sapphire laser stabilised to a Rb hyperfine component will serve as a reference for the wavemeter and transfer cavities (see next chapter) instead of the frequency-stabilised HeNe laser. If possible, a diode laser will be acquired for use with the saturated absorption spectroscopy setup, and thus act as a frequency reference when stabilised to a Rb hyperfine peak, replacing the Matisse cw Ti:sapphire laser which will be in use for collinear laser spectroscopy.

4 COLLINEAR LASER SPECTROSCOPY AT IGISOL

Collinear laser spectroscopy of neutron-rich Pd isotopes formed the main experiment of this work. In this chapter, firstly the collinear laser spectroscopy technique is explained. Then an overview of the experimental setup is given, consisting of sections on the production of radioactive ion beams at the IGISOL facility, the collinear laser spectroscopy beamline, and the laser system. Finally, several tests of the recently upgraded laser system are presented.

4.1 Collinear laser spectroscopy technique

Collinear laser spectroscopy is a high-resolution technique, which can be applied at radioactive ion beam facilities to study nuclear ground state properties over a wide range of elements [31]. Similar to saturated absorption spectroscopy, it is also a Doppler-free technique, the Doppler broadening being overcome by the use of accelerated beams. A schematic representation can be seen in Fig. 4.1. The energy spread of the ions,

$$\delta E = \delta \left(\frac{1}{2} m v^2 \right) = m v \delta v, \quad (4.1)$$

stays constant under acceleration, which means a higher velocity v results in a smaller longitudinal velocity spread δv and hence a reduced Doppler width. Using Equations 2.24, 4.1 and $m v^2 / 2 = e V_{acc}$, the Doppler width in frequency space in this case is given by

$$\delta \nu_D = \nu_0 \frac{\delta v}{c} = \nu_0 \frac{\delta E}{\sqrt{2 e V_{acc} m c^2}} \quad (4.2)$$

with ν_0 the transition frequency in the rest frame and V_{acc} the acceleration voltage. This shows that, using a typical value of about 1 eV for the original energy spread,

an acceleration voltage of 30 kV reduces the Doppler width to close to the natural linewidth (\sim tens of MHz).

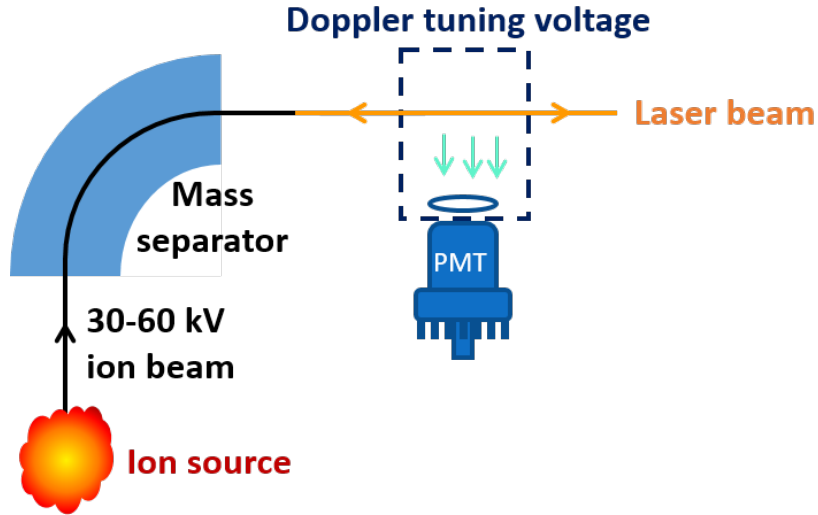


FIGURE 4.1 Figurative representation of the collinear laser spectroscopy technique. The two directions of the laser beam denote the collinear (in the direction of the ion beam) and anti-collinear geometries.

For calculating the frequency observed by the accelerated ions in the relativistic approach, Eq. 2.24 is adapted to

$$\nu = \nu_L \frac{1 \pm \beta}{\sqrt{1 - \beta^2}} \quad (4.3)$$

in a collinear ($-$) or anti-collinear ($+$) geometry (see Fig. 4.1). Here β is the relativistic Lorentz factor

$$\beta = \frac{v}{c} = \sqrt{1 - \frac{m^2 c^4}{(eV_{acc} + mc^2)^2}}. \quad (4.4)$$

The frequency in the reference frame of the ions can thus be changed by applying an additional tunable acceleration voltage, typically \pm several kV which is added to the original V_{acc} . This method of frequency scanning is called Doppler tuning, and allows the laser frequency in the laboratory frame to be locked to a precise reference frequency. This is advantageous as it eliminates systematic uncertainties related to frequency scanning (see e.g. chapter 3), and the acceleration voltage can be changed faster and more reliably than the laser frequency.

4.2 Experimental setup

4.2.1 Ion beam production at IGISOL-4

Two main techniques are in use worldwide for the production of radioactive ion beams: in-flight fragmentation and isotope separation on-line (ISOL). The in-flight method is in use e.g. at NSCL (in the USA) [95], GSI (Germany) [96] and RIBF (Japan) [97], and requires high-energy heavy-ion primary beams impinging on a thin target to form fission/fragmentation projectiles which are separated by a combination of electric and magnetic fields. The ISOL technique is used e.g. at ISOLDE, CERN [98] and the ISAC facility at TRIUMF [99], and typically employs thick targets. These thick targets and the need for a separate ion source to produce the beams make the ISOL technique rather slow and sensitive to chemical reactions in the source, which prohibits access to certain elements (e.g. refractory elements). To overcome these limitations, the gas-cell based ion-guide method was developed at the University of Jyväskylä in the early 1980s [100]. The Ion Guide Isotope Separator On-Line (IGISOL) facility has seen many developments and upgrades, an overview of which (up to 2013) can be found in [101], where also the latest upgrade to IGISOL-4 is described.

At the IGISOL-4 facility, radioactive ions can be produced either via fission or fusion reactions, the former induced by protons and the latter by light to medium-heavy beams from the K130 or MCC30 cyclotron impinging on a thin target. A schematic of the front end of the facility can be seen in Fig. 4.2. The reaction products are stopped in a gas cell filled with helium, guided by gas flow through an exit hole, and extracted using a sextupole ion guide SPIG [102]. They are then electrostatically accelerated to $30q$ keV, with the most common charge state q equal to +1.

The layout of the whole facility can be seen in Fig. 4.3. In addition to the ion guide method for ion beam production, stable beams can also be produced using the offline station on the second floor which was recently commissioned [103]. Two ion sources are available, a surface ion source and a glow discharge ion source. The ion beam produced either at the front end or in the offline station is mass separated using a 55° dipole magnet with a resolving power of $M/\Delta M \sim 500$. It is then transported to either the cesium atom trap station [104], the radio-frequency quadrupole (RFQ) cooler-buncher [105] or the decay spectroscopy line from the electrostatic switchyard. When going to the cooler-buncher, the ions are decelerated to ~ 50 V below the 30 kV of the IGISOL High Voltage (HV) platform, before entering.

Helium buffer gas is used to cool the ions in the cooler-buncher, and a radiofrequency electric field is applied to four segmented quadrupole rods to contain

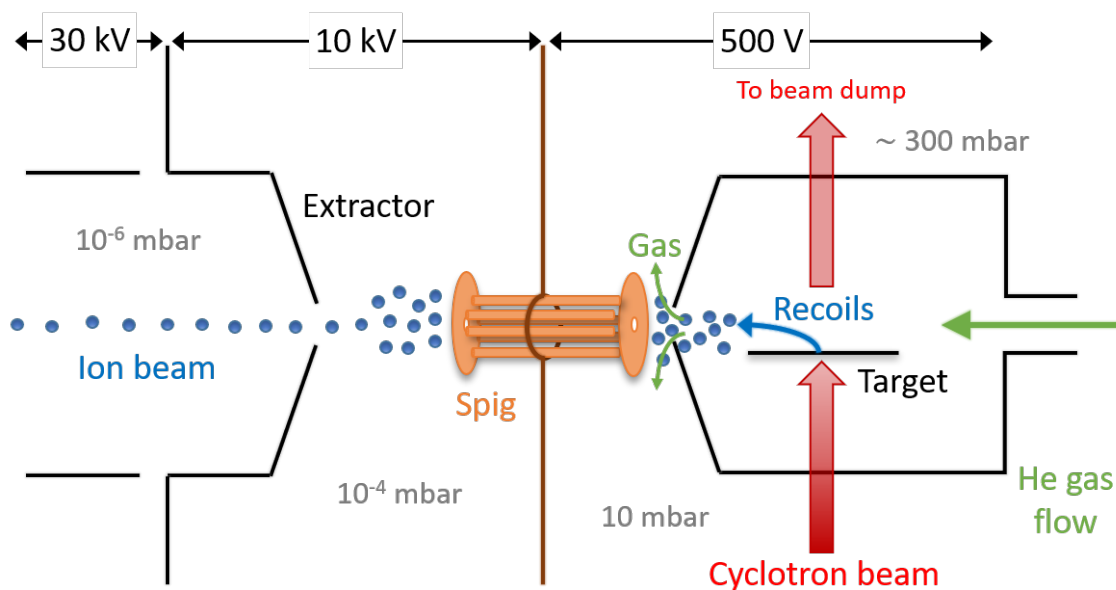


FIGURE 4.2 Schematic of the IGISOL ion guide and extraction of the ion beam.

them. After a holding time of ~ 100 ms, the ions are released as short bunches, typically $10 - 15 \mu\text{s}$ in width, at an energy of 800 eV. The cooled beams have a lower energy and emittance, both of advantage for collinear laser spectroscopy as the former reduces the Doppler broadening and the latter makes overlap with a narrower laser beam feasible. In addition, bunching allows for photon background suppression by a factor of ~ 10000 by gating the photo-multiplier tube signal. The optimal holding time in the RFQ cooler-buncher for collinear laser spectroscopy is a trade-off between better signal-to-background and decay losses due to the half-lives of isotopes under study at longer times. Exiting the cooler-buncher, ion bunches can be transported to either the JYFLTRAP [106] double Penning trap or to the collinear laser spectroscopy setup.

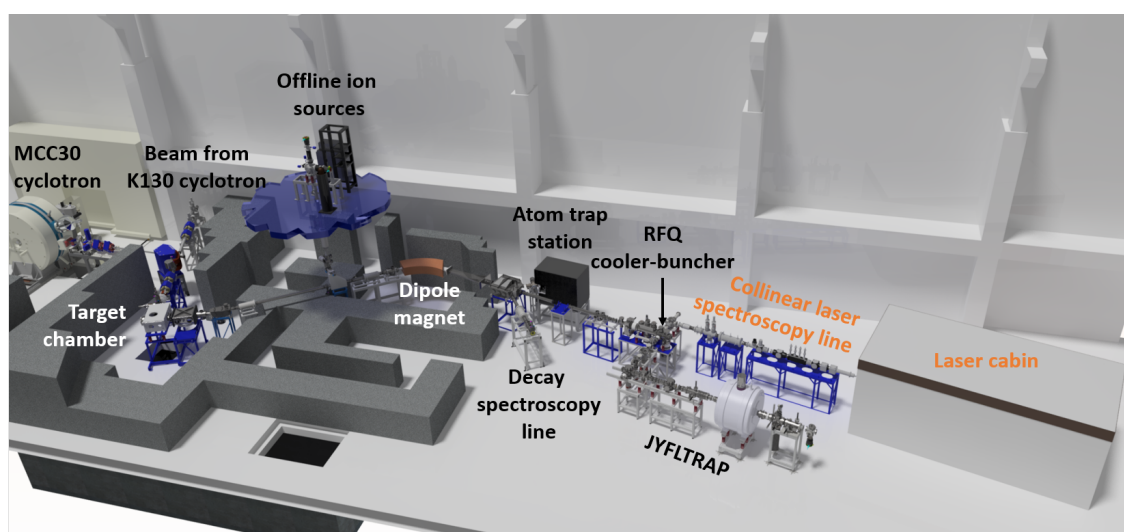


FIGURE 4.3 Layout of the IGISOL-4 facility.

4.2.2 Collinear laser spectroscopy beamline

The ion bunches are injected into the collinear beamline via two 90-degree quadrupole benders and then accelerated to 30 kV. An overview of the recently upgraded [107] beamline is shown in Fig. 4.4. Electrostatic steerers guide the ions along the beamline, towards the Charge-Exchange Cell (CEC) and Light Collection Region (LCR). The beam is focused in front of the segmented Photo-Multiplier Tube (PMT) in the LCR using a quadrupole triplet. The charge-exchange cell is used to neutralise the ions when needed via electron-capture reactions and is removable. Neutralisation is required for elements where laser spectroscopy on the atom is more advantageous, usually due to the lack of suitable optical transitions in the ionic state. This cell and its vacuum chamber were originally designed for the collinear beamline at the TRIGA facility in Mainz, Germany [108]. The cylinder in the cell is filled with a neutralising element, typically either potassium or sodium, and is electrically heated using a variable AC power supply to create a vapour. To ensure the (alkali) vapour does not escape into the beamline, the ends of the cell are kept at a fixed temperature below the melting point of the alkali using a Lauda RA-8 oil circulator. Thermocouples attached to the top of the cell and to the ends are used to monitor the temperature. The ions that are not neutralised are removed from the atom beam using a pair of electrostatic deflector plates. Particle and laser beams are then overlapped in a counter-propagating manner by tuning both through a retractable 0.9 mm aperture. The adjustable acceleration voltage required for Doppler tuning is applied to the platform supporting the charge-exchange cell and LCR, which is electrically insulated from the housing chamber.

The beamline contains several diagnostics for beam tuning and monitoring. There are two insertable Faraday cups, used to optimise the transport efficiency of stable ions, and a silicon detector for transport optimisation of radioactive ions. At the end of the beamline, an off-axis Micro-Channel Plate (MCP) detector and a MagneTOF mini-detector mounted on a linear actuator are installed. Both of these are used for beam tuning and monitoring the neutralisation efficiency.

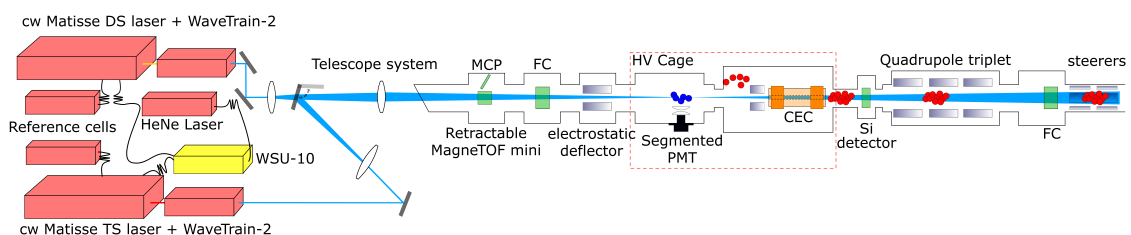


FIGURE 4.4 Schematic view of the light collection region and laser systems of the collinear beamline at IGISOL from Article [PIII]. The ion bunches (red) enter the beamline from the right.

A new data acquisition system was taken into use in 2018 [107]. The main recorded elements are signals from the PMT segments, the RFQ cooler platform voltage, the tunable acceleration/deceleration voltage and the wavemeter readout. A fast timing amplifier is used to amplify the PMT signals, and a constant-fraction discriminator to discriminate them. These signals are then time-stamped by a Time-to-Digital Converter (TDC) with four channels with a 500 ps single-shot resolution. The Doppler tuning voltage is generated by amplifying a voltage between -4 and 4 V, from one of the analogue outputs of the data acquisition board, a thousand times with a high-voltage amplifier. After every scan, this voltage is calibrated over the scanning range by reading it out with a Keysight digital multimeter after a 1:1000 voltage divider. The cooler platform voltage is continuously read out using either a voltmeter or a second Keysight multimeter with a 1:10000 voltage divider. The laser frequency is monitored using the WSU-10 wavemeter. Both the cooler platform voltage and laser frequency are recorded for each scan at the same time as the voltage calibration. The control software, written in Python, is integrated into the Python and EPICS-based control for the whole IGISOL facility. A pulse generator is used to trigger the TDC card, cooler-buncher release, and the digital multimeter to ensure synchronisation.

4.2.3 Laser system

Up until recently, all collinear laser spectroscopy experiments were conducted using a Spectra Physics 380 dye laser with long-term frequency stabilisation ensured via an iodine absorption cell [109,110]. This was replaced by a new laser system based on two Sirah Matisse 2 continuous wave (cw) lasers pumped by a 20 W Spectra Physics Millennia eV laser, also shown in Fig. 4.4. One cw laser is a newly acquired dye DS laser, and the other one the Ti:sapphire TS laser which has been moved from the cabin containing the saturated absorption spectroscopy setup (Fig. 3.3) to the collinear laser cabin. The WaveTrain 2 frequency doubling unit was also moved, and a new one bought to accompany the cw dye laser.

The optical layout of the Matisse 2 TS laser can be seen in Fig. 4.5. The layout of the DS laser is almost identical, the only differences being the dye jet as a lasing medium, and a parallel displacement rhomb placed in the laser beam path to account for the slight offset of the path compared to the Ti:sapphire laser. Each laser comes with different mirror sets coated for specific wavelength ranges, which already make a selection out of the full intrinsic emission spectrum of the lasing medium. The selection of a single frequency mode in the laser is then accomplished by consecutively scanning the birefringent filter and the thin etalon. The birefringent filter consists of multiple birefringent plates with different thicknesses, and frequency selection takes place by rotating the plates. To achieve single-mode operation two etalons are needed, a solid-state etalon (Thin Etalon) to

further narrow the frequency range, and a piezo-driven Fabry-Pérot interferometer (Thick Etalon) to select the final frequency mode. A unidirectional device ensures the clockwise running mode of the laser. The laser frequency can be scanned by adjusting the cavity length via the piezo-driven tuning mirror.

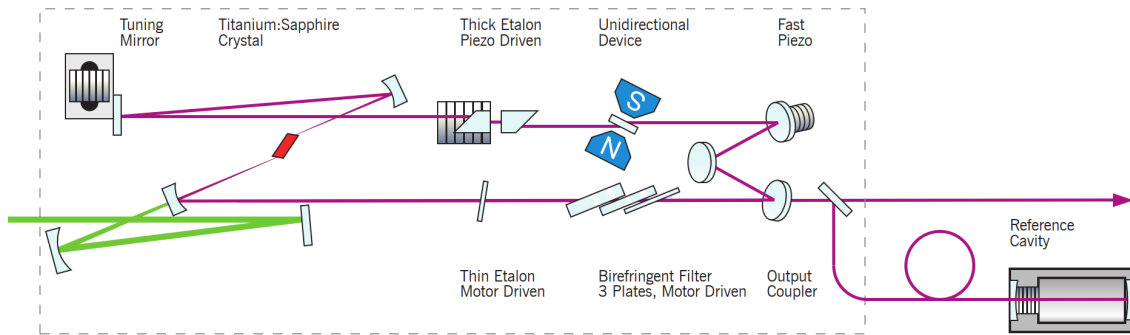


FIGURE 4.5 Optical layout of the Sirah Matisse 2 TS cw Ti:sapphire laser [111]. The pump beam enters the resonator from the left (green line).

To ensure short-term stability, i.e. a narrow linewidth, both Matisse lasers have an external reference cavity which is coupled to the fast piezo cavity mirror via a feedback loop. If long-term frequency stability is required, the reference cavities can in turn be locked to the WSU-10 wavemeter, or to a frequency-stabilised HeNe laser using a transfer cavity which will be discussed in section 4.3.2.

For the majority of studied elements, frequency-doubled light is required, hence the use of the WaveTrain 2 doubling units. These units are based on a triangle-shaped enhancement cavity containing a temperature stabilised nonlinear crystal, which generates the second harmonic of the fundamental frequency from the Matisse laser. The (frequency-doubled) laser light is then focused into a 1 mm spot in front of the PMT using a telescope system. Typical background rates due to scattered laser light are about 100 Hz per 100 μ W of laser light.

4.3 Systematic tests

4.3.1 Wavemeter tests

In collaboration with three other institutes, an in-depth investigation of the reliability of wavemeters has been performed. The results were split in two parts, Part 1 as Article [PII] and Part 2 in [112]. Here the contribution by Jyväskylä to Part 1, which was done as part of this thesis work, will be described in more detail. The underlying motivation for this work and more generally at all facilities was the disagreement noticed between the readout of commercial wavemeters and

several reference sources, such as an FPI and a frequency comb. More specifically, reproducible periodic patterns in the frequency comparisons to an FPI were seen when testing HighFinesse WS7-60(-IR) (quoted absolute uncertainty of 60 MHz at 3σ) and WSU-30 (absolute uncertainty 30 MHz) wavemeters.

Due to this, similar measurements were performed at IGISOL using the HighFinesse WSU-10 (absolute uncertainty 10 MHz) wavemeter. Using the saturated absorption spectroscopy setup described in chapter 3, six scans over the hyperfine structure of ^{85}Rb and ^{87}Rb on the D1 line were performed. The wavemeter readout was then compared to the frequency calculated using the Toptica FPI. A periodic fluctuation was noticed, with an amplitude of about ± 5 MHz, but it was not the same in every scan nor did it resemble a function that could be fitted, as can be seen in Fig. 4.6. As the resolution of the WSU-10 wavemeter is better than the WS7-60 and WSU-30, the pattern could be masked by other fluctuations, for example non-linearities in the scanning of the FPI. Another indication that the amplitude of the effect is likely much smaller in the WSU-10 wavemeter, is that no deviations from literature larger than 1-2 MHz were seen when measuring the hyperfine parameters using the wavemeter, on either the atomic D1 or D2 line in Rb or the D2 line in Cs, as mentioned in chapter 3.

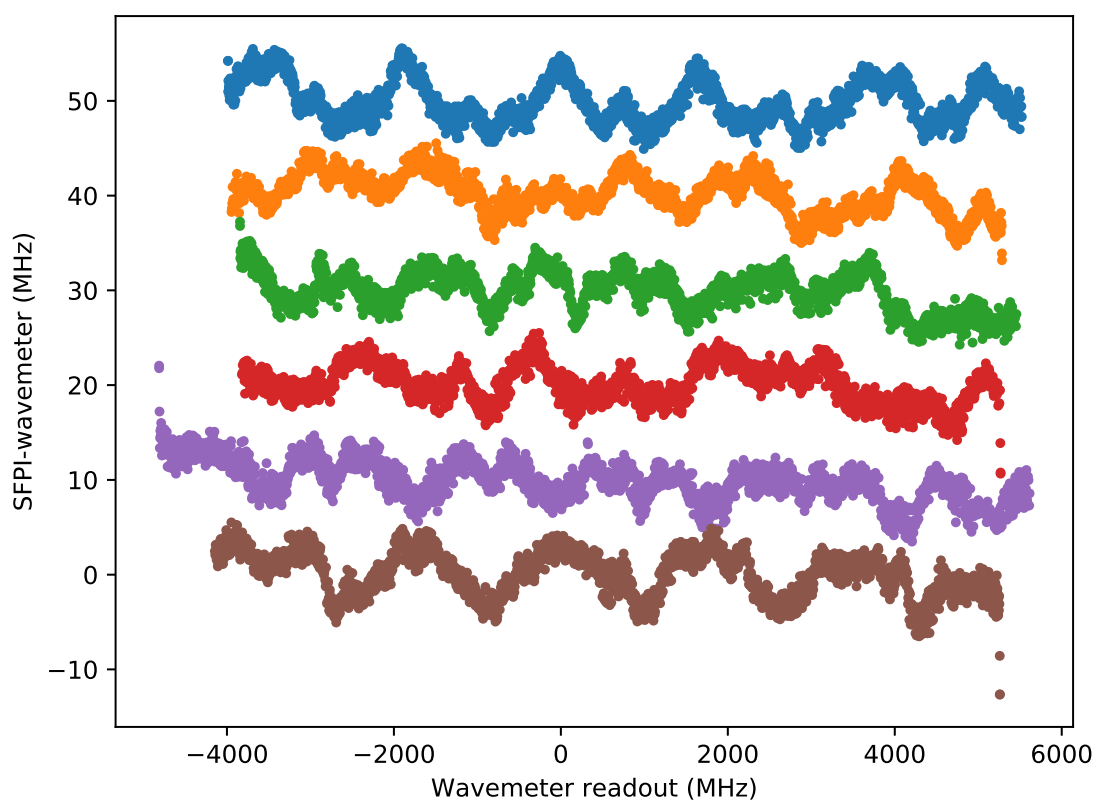


FIGURE 4.6 Difference between wavemeter readout and frequency calculated using the Toptica Scanning FPI (SFPI) in six different Rb hyperfine scans. Each scan is offset by 10 MHz on the y-axis for clarity.

In order to test for any periodic pattern more precisely, a comparison of the WSU-10 to an atomic resonance provided by collinear laser spectroscopy was performed. Stable yttrium (^{89}Y) was chosen as large beams can easily be produced using the spark discharge source. The 363.4157-nm transition from the ionic ground state was used, with the laser light provided by the cw Ti:sapphire laser which was stabilised to the wavemeter at a fixed frequency here called the stabilisation setpoint. To probe for systematic discrepancies between the WSU-10 and the centroid of the hyperfine structure, the stabilisation setpoint was changed in steps of 0.02 cm^{-1} , and for each setpoint a spectrum with sufficient statistics (> 1000 counts on peak) was collected.

The resulting ^{89}Y hyperfine spectrum consists of an unresolved doublet, which was fitted using the Statistical Analysis Toolbox for Laser Spectroscopy (SATLAS) package [113], fixing the hyperfine parameter of the upper state to the literature value of 32.6(1) MHz [114]. The fitted centroid frequency at each laser setpoint can be seen in Fig. 4.7. Based on the patterns seen at other facilities, a triangular wave function was fitted to the data, using the equation

$$\Delta_{triangle}(v) = \frac{4A}{T} \left((v + S) - \frac{T}{2} \left\lfloor \frac{2(v + S)}{T} + \frac{1}{2} \right\rfloor \right) \cdot (-1)^{\left\lfloor \frac{2(v+S)}{T} + \frac{1}{2} \right\rfloor} \quad (4.5)$$

with A the amplitude, T the period, S the shift, and the symbol $\lfloor x \rfloor$ denoting the floor function of x . This resulted in a peak-to-peak amplitude of 1.6(3) MHz and a period of 2.07 (12) GHz. The amplitude is about five times smaller than that observed for the WS7-60 and WSU-30 (see Table 1 in Article [PII]), and agrees well with the ± 2 MHz reported for another WSU-10 compared to a frequency comb in [112]. The period is also consistent with the ≈ 2 GHz FSR of the most precise interferometer in the wavemeter, as noticed for all other tested wavemeters.

A procedure to correct for the periodic effect is described in Article [PII]. Because of the large errors on the fitted parameters and the small amplitude of the effect for the WSU-10, this correction will not be applied at IGISOL. For future collinear laser spectroscopy experiments the transfer cavity stabilisation technique will be used instead of the wavemeter, discussed in the next section. For other experiments involving scanning of the laser frequency, for example in-source or in-gas-jet resonance laser ionisation, a conservative systematic error of 10 MHz, according to the wavemeter specifications, will be taken into account. However, other errors, statistical and/or systematic, will almost certainly dominate in these experiments. If better accuracy would be required at any stage in the future, the characterisation to a frequency comb as described in [112] could be considered.

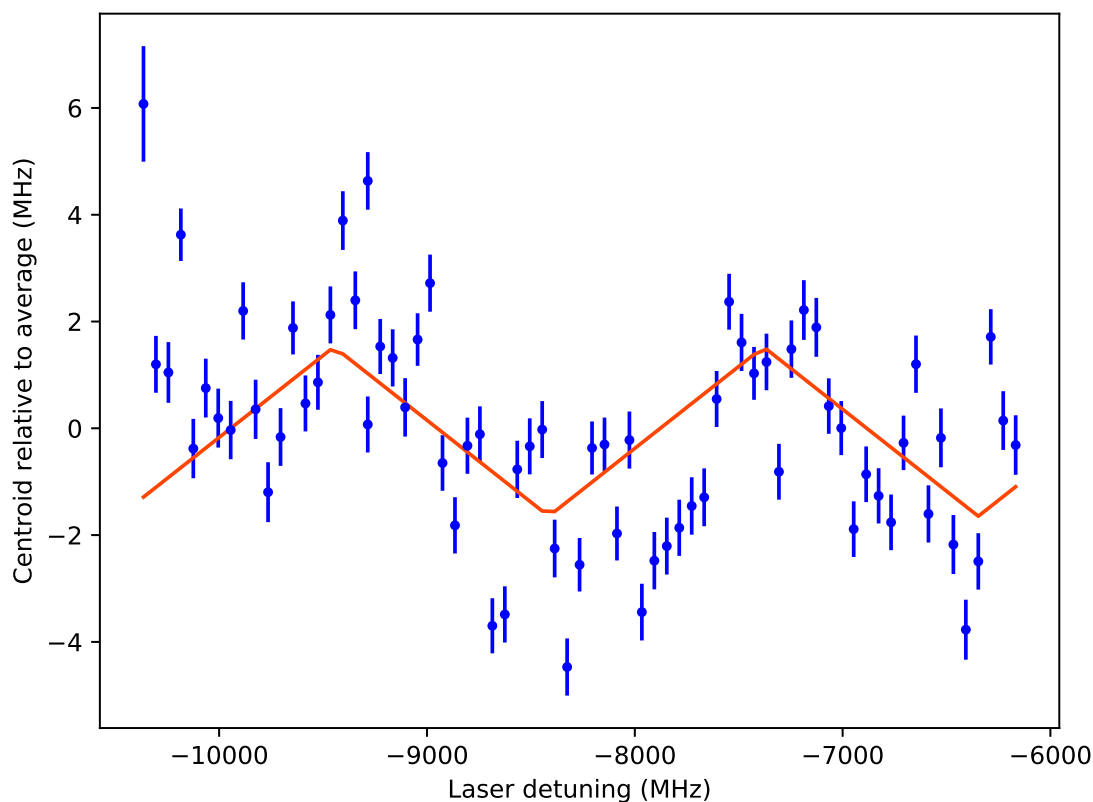


FIGURE 4.7 The fitted centroid of the ^{89}Y hyperfine structure at changing laser stabilisation setpoints using the WSU-10 wavelength meter (blue). A triangular wave function was applied to the resulting data (red solid line). Updated from Fig. 5 in Article [PII].

4.3.2 Frequency stabilisation

To further reduce the systematic uncertainties on the long-term stabilisation of the cw lasers, especially when changing stabilisation setpoints, it was decided to bypass the wavemeter by switching to a transfer cavity where the absolute frequency stability of a stable laser (master) is transferred to a second laser (slave). This was set up using the frequency-stabilised Thorlabs HeNe laser as master laser, and with the reference cell of the Matisse Ti:sapphire laser (slave laser) as the transfer cavity. A schematic implementation can be seen in Fig. 4.8.

Both laser beams are superimposed in front of and separated again behind the reference cell by dichroic cold mirrors (Thorlabs M254C45). A Thorlabs PDA36A-EC photodiode is used to measure the transmitted HeNe laser light while the intensity of the Matisse is observed by the original photodiode of the reference cell. A digital plugin of the Matisse control software uses the intensity measured by the HeNe photodiode, read out with a data acquisition hardware module from National Instruments (NI USB-6000), to stabilise the reference cell length with a side-of-fringe locking method. A shortpass filter for 700 nm (Thorlabs FES0700) is placed in front of the HeNe photodiode so as to prevent unwanted feedback

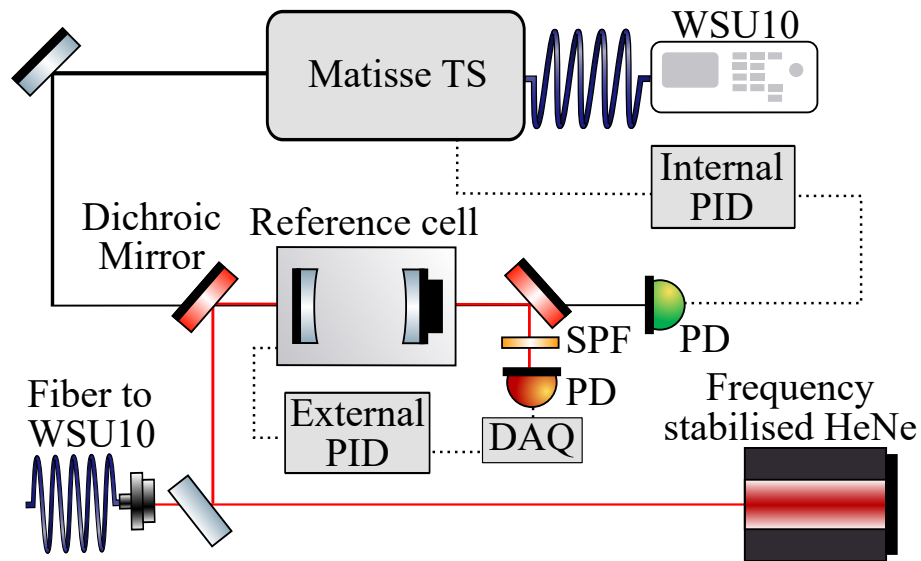


FIGURE 4.8 Schematic of the transfer cavity implementation for the cw Ti:sapphire laser. PD = Photodiode, SPF = Shortpass Filter.

due to reflected/scattered Ti:sapphire light, which would result in scanning of the Ti:sapphire frequency. Since the Ti:sapphire laser is still stabilised to its reference cell, the absolute frequency stability is now directly related to the frequency stability of the HeNe laser.

In order to compare stabilisation to the wavemeter with stabilisation to the transfer cavity, collinear laser spectroscopy on ytterbium was performed. Ytterbium was chosen as it has seven stable isotopes, can be produced by the spark discharge source, and has an easily accessible ionic transition at 369.524 nm. Spectra for all even-even isotopes were taken at six different frequency setpoints, once with stabilisation to the wavemeter and once with stabilisation to the transfer cavity. All spectra were fitted with a Voigt profile to determine the centroid. The scatter on the fitted centroids for each isotope, quantified by the 1σ confidence level, was reduced from 4.6 MHz when stabilised via the wavemeter, to 3.8 MHz via the transfer cavity, as can be seen in Fig. 4.9. This establishes the wavelength meter as a possible source of systematic uncertainty. As mentioned at the end of the previous chapter, there are plans to replace the HeNe laser by a laser stabilised to a saturated absorption spectrum, further reducing the uncertainty in the frequency stability of the cw lasers over time.

For interest, a comparison of the frequency spread of all stabilisation methods tested in this work has been made. This was done both for the old Spectra Physics 380 dye laser, as well as the Matisse cw Ti:sapphire laser. The Spectra Physics dye laser was stabilised via the wavemeter and via an iodine absorption line. The result can be seen in Fig. 4.10. The frequency spread was improved by about a factor two when stabilising via the wavemeter instead of the iodine absorption line.

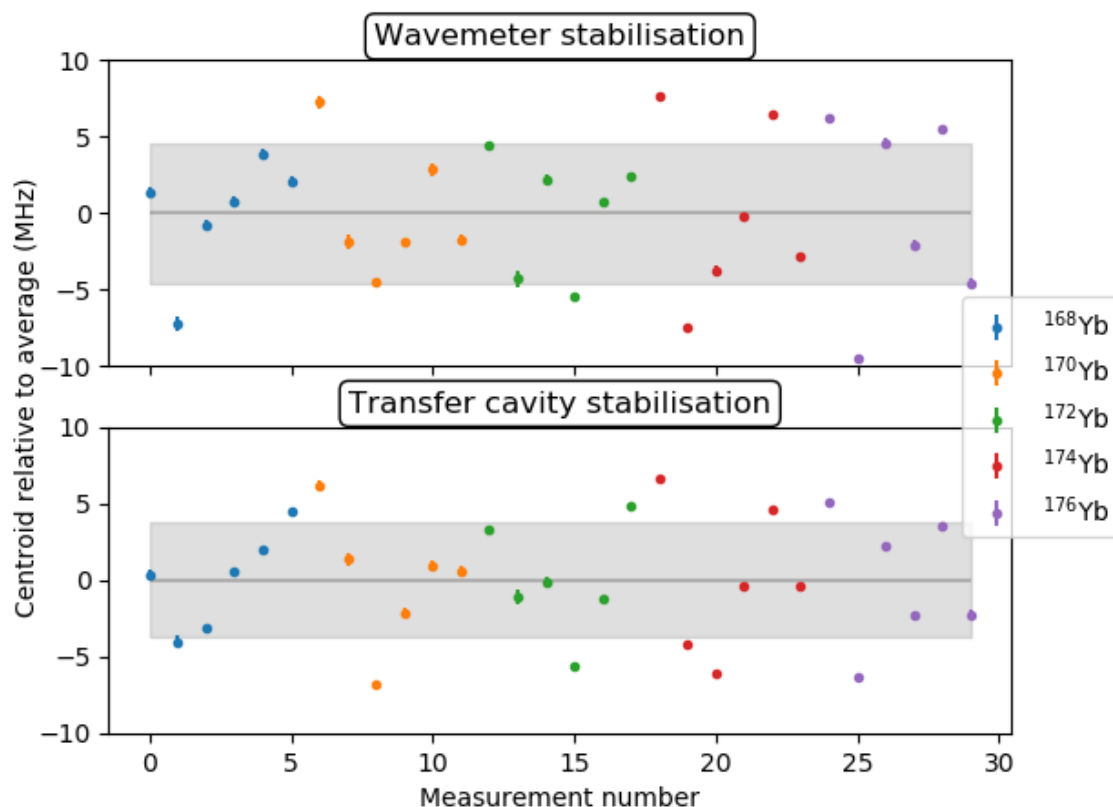
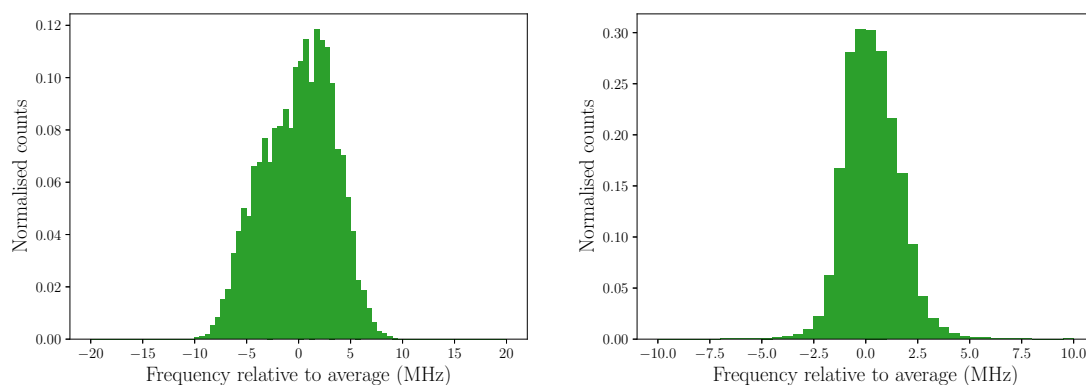


FIGURE 4.9 The fitted centroids of the even-even Yb resonances at changing laser stabilisation setpoints using the WSU-10 wavemeter (upper) and the transfer cavity (lower). The shaded areas denote the 1σ spread. Updated from Fig. 6 in Article [PII].



(a) Stabilised via an iodine absorption line

(b) Stabilised via the wavemeter

FIGURE 4.10 Frequency spread of the Spectra Physics 380 dye laser over about two hours.

The same comparison can be made for the Matisse cw Ti:sapphire laser, with either stabilisation via the wavemeter, the transfer cavity, or a Rb hyperfine peak. The resulting histograms can be seen in Fig. 4.11. All techniques reach a frequency spread on the order of 1 MHz, with the stabilisation to the wavemeter having the smallest spread. The small increases for the other two methods is likely due to

hardware or software limitations, e.g. the DAQ sample rate. A summary of the different methods and their resulting frequency spread can be seen in Table 4.1.

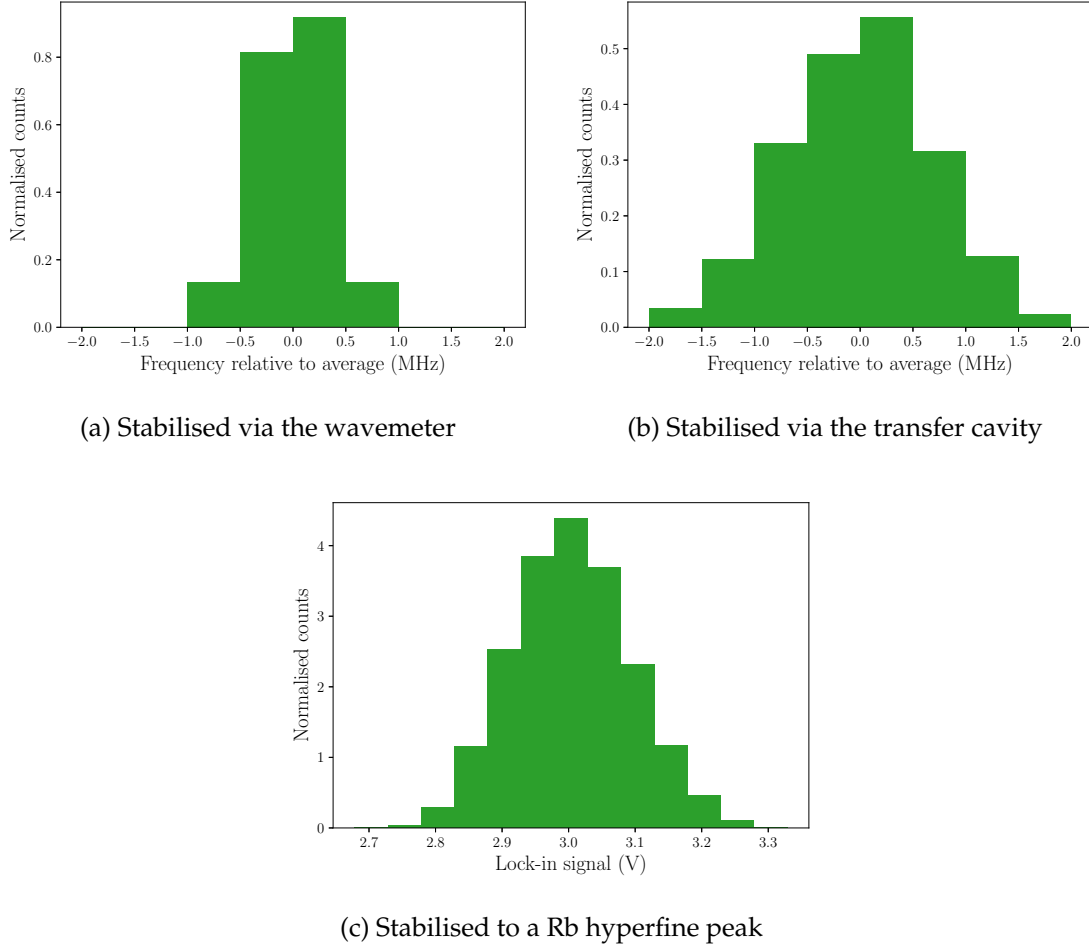


FIGURE 4.11 Frequency spread of the Matisse TS Ti:sapphire laser over many hours. In (c): $0.2 \text{ V} \approx 1.2 \text{ MHz}$

TABLE 4.1 Frequency stabilisation methods for cw lasers and the resulting frequency spread.

Method	Frequency spread (FWHM) (MHz)
Spectrophysics + iodine	8.2
Spectrophysics + wavemeter	3.1
Matisse TS + wavemeter	0.8
Matisse TS + transfer cavity	1.7
Matisse TS + Rb hyperfine peak	$0.21 \text{ V} \approx 1.25 \text{ MHz}$

5 MEAN-SQUARE CHARGE RADII OF NEUTRON-RICH PALLADIUM ISOTOPES

In this thesis work, collinear laser spectroscopy of palladium isotopes was performed, resulting in the first determination of changes of mean-square charge radii for neutron-rich even- A isotopes $^{112-118}\text{Pd}$. This chapter consists of the motivation for this experiment, the preparation using stable isotopes, the experimental details and data analysis, the results and discussion, and finally an outlook.

5.1 Motivation

Figure 5.1 shows the changes in the mean-square charge radii for the isotopic chains below (left) and above (right) palladium. As already mentioned in section 2.2, changes in mean-square charge radii extracted from isotope shifts are very sensitive to deformation (Eq. 2.16). This is obvious in Fig. 5.1, as parabolic trends in the change in mean-square radii are observed in the Sn [115, 116], In [117], Cd [118, 119] and Ag [120] chains, expected when the deformation evolves smoothly. This parabolic behaviour is related to quadrupole contributions in a core polarisation model [121]. On the other hand, below the Pd isotopic chain, the measurements show evidence of a dramatic shape change observed at $N = 60$, maximised and centered around yttrium [114]. In the transitional area between both regions, i.e. the Tc, Ru, Rh and Pd isotopes, no optical spectroscopic information is available for radioactive nuclei. This is in part due to the refractory character of these nuclei, which makes their production challenging for many facilities, but also due to their complex atomic structure. This region can be explored at IGISOL thanks to the chemical insensitivity of the ion-guide method and the installation of the charge-exchange cell in the collinear beamline.

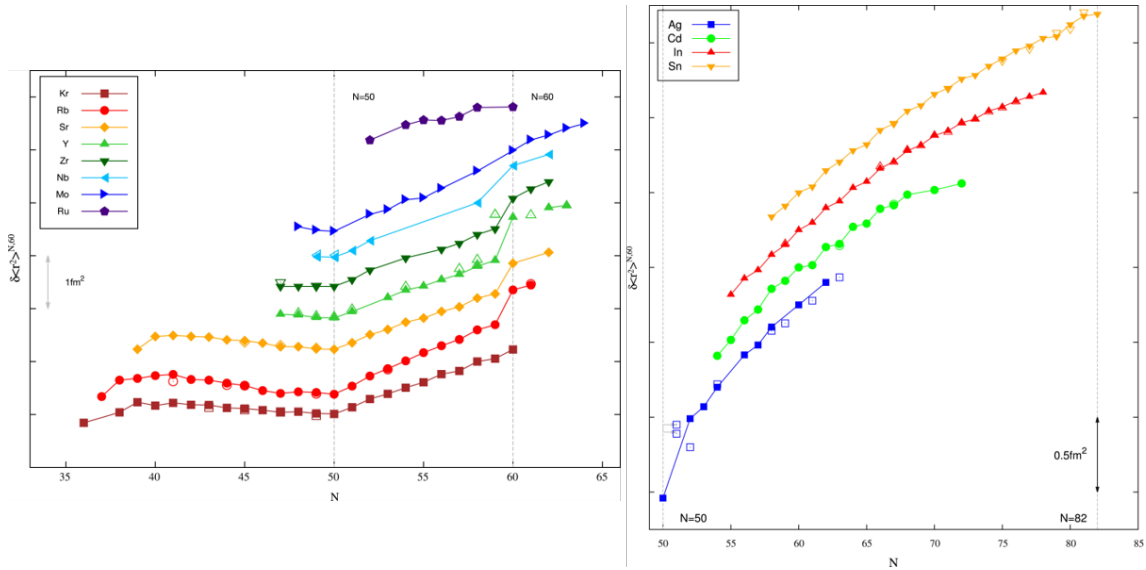


FIGURE 5.1 Changes in mean-square charge radii as a function of neutron number. Left: Region below Pd chain. Right: Region above Pd chain. Reprinted from P. Campbell, I.D. Moore, M.R. Pearson, Laser spectroscopy for nuclear structure physics, Prog. Part. Nucl. Phys., 86, 127-180, Copyright (2016), with permission from Elsevier and I.D. Moore [31].

So far most experimental nuclear structure information on the Pd chain has come from decay spectroscopy studies. The majority of the early experiments on Pd isotopes were conducted by studying spontaneous fission fragments produced by ^{252}Cf and ^{248}Cm sources or by fusion-fission reactions of different primary beams and a ^{238}U target. These experiments focused on prompt gamma spectroscopy [122–130], and provided access to valuable information on excited states of these neutron-rich nuclei. Work on β -decay spectroscopy either from the Rh parent nuclei [124, 131–134] or from the Pd isotopes themselves [135] further completed the experimental picture. An overview of β -decay experiments in the region conducted at IGISOL can be found in [136].

In addition several theoretical studies have been devoted to the region around the Pd chain. Calculations using the deformed proton-neutron quasiparticle random-phase approximation, with an underlying SLy4 Skyrme functional, were performed for neutron-rich Ge, Se, Kr, Sr, Ru, and Pd isotopes [137]. These calculations show that the potential energy curves for even-even Pd isotopes exhibit oblate and prolate minima in the lighter isotopes ($A = 114 - 117$) and a gradual transition into spherical shapes when approaching the $N = 82$ shell closure, and predict the corresponding deformation parameters and charge radii for the studied isotopes. Other theoretical research using a shell-model approach predict a change from prolate to oblate deformation in the region [138], based on the protons and neutrons have reinforcing effects favouring oblate deformation at approximately $70 \leq N < 82$ and $40 \leq Z < 50$. This change of deformation has been reported in the ^{110}Mo [139] and ^{111}Tc [140, 141] isotopes.

Disagreement on the origin and character of the (possible) change in deformation in the Pd isotopes can be found in the experimental work. From early experiments it was suggested that $^{110-116}\text{Pd}$ presents a decay pattern compatible with a γ -soft rotor [133]. In later gamma-spectroscopy work, one study interpreted the spectra of $^{112,114,116}\text{Pd}$ as being caused by the oblate-driving proton $(g_{9/2})_2$ quasiparticle alignment, suggesting an oblate-deformed core [127]. Another study however interpreted the ground state of the Pd isotopes from $A = 109$ to $A = 123$ to be of prolate nature, with a decreasing deformation parameter with increasing mass number, leading to spherical ^{128}Pd [126]. This is supported by work in [130] indicating ^{118}Pd still maintains a prolate shape. The sphericity of ^{128}Pd has been confirmed by the observation of the 8^+ seniority isomer [142] resembling that of ^{130}Cd [143]. The possibility of a prolate to oblate shape change at ^{115}Pd has also been suggested, due to the change in ground-state spin assignment of the odd- A isotopes from $5/2^+$ for $^{105-113}\text{Pd}$ to $1/2^+$ for $^{115-117}\text{Pd}$ [125, 132, 134]. Other studies place the shape change from prolate to oblate at ^{116}Pd [128] or suggest a more complicated picture involving triaxial shapes, with a triaxial oblate shape already at ^{112}Pd [129].

The systematics of the low-lying states in the odd- A Pd isotopes are shown in Fig. 5.2. An interesting feature is the presence of isomeric states, which feature a large hindrance factor for the isomeric transition, in comparison to neighbouring nuclei [131, 134]. This large observed hindrance factor at $^{107-111}\text{Pd}$ has been attributed to a strong change of deformation between isomer and ground state, while for heavier systems, i.e. $^{113-115}\text{Pd}$, the hindrance factor gets reduced. This would point to smaller shape differences [132]. On the one hand oblate deformation for the negative parity isomeric states was predicted in [126] for $^{111,113,115}\text{Pd}$ isotopes, while in [123] prolate deformation was proposed based on the observed band crossing of the negative parity bands built on the $11/2^-$ isomeric states, which is supported by work in [122]. Moreover, while an $11/2^-$ spin and parity has been assigned to the isomeric levels, an inversion with respect to the $9/2^-$ and $7/2^-$ for heavier systems has been suggested, but unambiguous determinations could not be performed.

Collinear laser spectroscopy is especially well suited to clarify many of these outstanding disagreements on the nuclear structure in the Pd chain. The ground state and isomer properties, determined in a model-independent way, are important to underpin the results from the decay spectroscopy work, e.g. with respect to spin assignments. The changes in mean-square charge radii, and possibly the nuclear quadrupole moments, can clarify the evolution of the deformation along the isotopic chain.

From a general viewpoint, charge radii have attracted quite some interest over the past years as they provide an ideal testing ground for various nuclear models, especially *ab initio* methods and DFT approaches, leading to several combined

predict significantly higher final populations for the ground state and low-lying metastable states using potassium, which was thus chosen as a neutraliser as the most convenient transitions found in literature are from these states.

The five different transitions ultimately selected for testing were chosen based on several considerations: the level populations predicted by charge-exchange calculations, the expected transition strength, the atomic spins involved, and the available wavelength range of the laser system. An overview of the transitions can be seen in Fig. 5.3. All collected spectra were fitted using the SATLAS Python package [113], developed for analysing laser spectroscopy data. For three out of five transitions hyperfine parameters of ^{105}Pd could be determined, which show good agreement with literature values (see Table 1 in Article [PIII]).

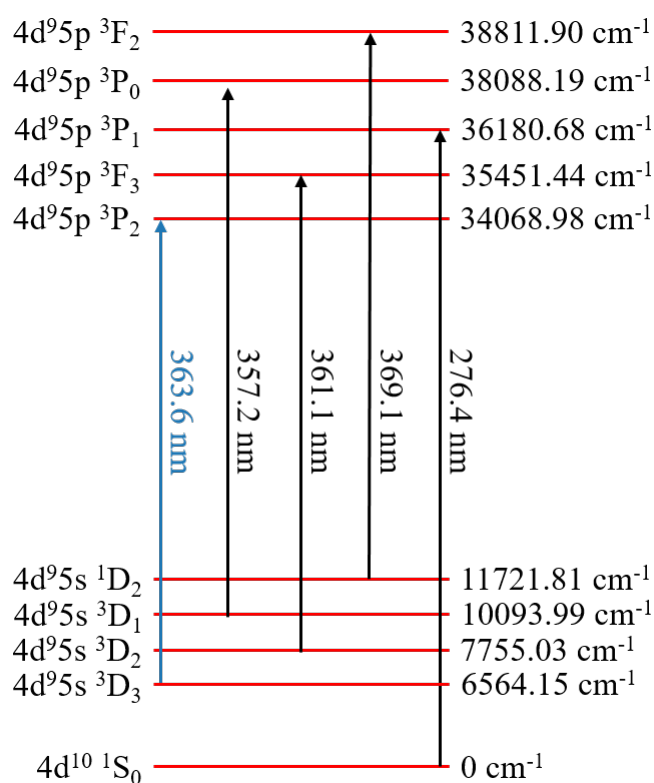


FIGURE 5.3 Overview of studied transitions in the Pd atom, with the selected transition for online use highlighted in blue. Figure adapted from Fig. 3 in Article [PIII]. Wavelengths are in vacuum [149].

A comparison was made between the measured peak intensities and the predicted level populations, using the particle current and laser power recorded for each scan. As detailed in Article [PIII], the charge-exchange calculations provide a good starting point to choose transitions, but do not reproduce the observed populations for Pd exactly.

Four transitions proved efficient enough to collect spectra of sufficient isotopes to

allow a King plot analysis using the measured isotope shifts and known charge radii obtained from the combined analysis of muonic X-ray and elastic electron scattering data [18]. This procedure to determine the atomic mass and field shift factors is described in section 2.2.3. Similar mass and field shift factors were found for all four transitions, as expected from the similar electron configurations involved.

The 363.6 nm transition from the 6564.15 cm^{-1} metastable level showed to be the most efficient and thus the optimal choice for use in collinear laser spectroscopy on radioactive isotopes. The atomic factors for this transition determined via the King plot are the field shift $F = -2.9(5) \text{ GHz/fm}^2$ and mass shift $M = 845(669) \text{ GHz amu}$.

5.3 Experimental details and data analysis

All data was acquired during a one-week experiment using proton-induced fission of a thorium target to produce neutron-rich Pd isotopes, with a proton beam intensity of $\sim 10 \mu\text{A}$. The fission fragments were stopped in the helium-filled fission ion guide and extracted as described in section 4.2.1. Figure 5.4 shows on the left the expected mass-separated yield based on the independent yield measurements presented in [150], scaled to the typical yields of ^{112}Rh that have been observed in previous fission runs at the IGISOL. The right side of Fig. 5.4 shows what percentage of the total fission yield at each mass is expected to be palladium, to indicate the approximate level of contamination from fission isobars. The yield of ^{112}Rh measured during this experiment was $\sim 40000 \beta/\text{s}$, in other words $\sim 130000 \text{ ions/s}$ assuming a Si detector efficiency of about 30%. Holding times in the RFQ cooler of either 100 ms or 200 ms were used, and a bunch width of $\sim 15 \mu\text{s}$ was obtained.

The charge-exchange cell was heated to $140 \text{ }^\circ\text{C}$ as measured on top of the cell, so the temperature in the cell was likely higher. A neutralisation efficiency of about 40 % was observed, determined as the ratio of the total detected beam on the MagneTOF mini detector to that when a voltage is applied to the electrostatic deflector (Fig. 4.4). Rates on the order of 5000 atoms/s were measured at $A = 116$ at the end of the collinear beamline, while at $A = 118$ it was about 3200 atoms/s. During the first part of the experiment, focused on the even- A isotopes, regular scans of ^{108}Pd were taken as a reference using the offline source. Due to technical difficulties with the offline source, the reference was changed to ^{116}Pd during the latter part of the experiment which focused on the odd- A isotopes. The Matisse TS laser was stabilised to the wavemeter, with changes in the stabilisation setpoint depending on which isotope was under investigation. This change in setpoint

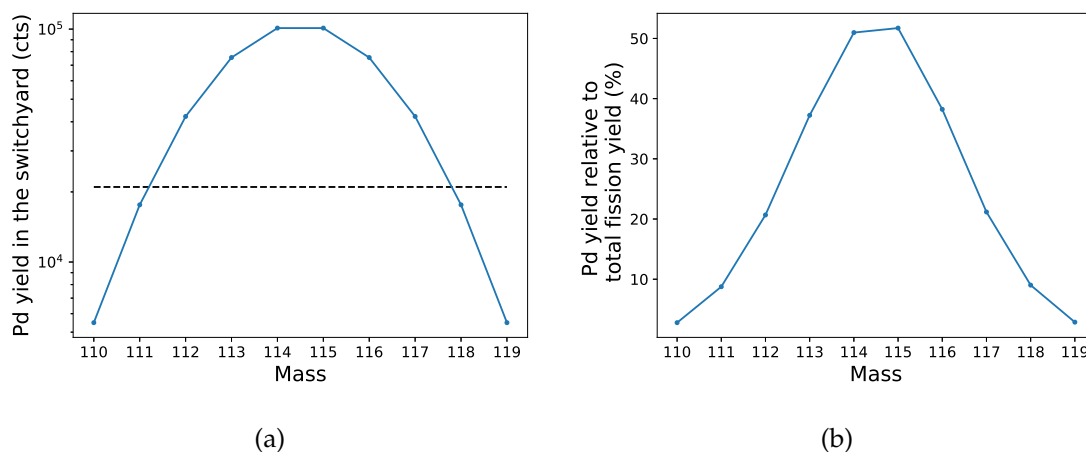


FIGURE 5.4 Left: Expected experimental yields of palladium using proton-induced fission on a Th target in the IGISOL switchyard at $10 \mu\text{A}$ proton beam intensity. The horizontal line denotes the approximate yield previously needed for collinear laser spectroscopy experiments on neutron-rich silver isotopes, studied at IGISOL in 2018. Right: Percentage of total fission yield expected to be palladium isotopes at each mass, not including any possible feeding from the beta decay parent.

was required as the range of the tuning voltage applied to the charge-exchange and light collection region housing was limited due to beam steering issues. This meant that when applying large voltages, a reduction in beam transmission was seen. Stabilisation via the transfer cavity was not possible as it was not arranged for easy and rapid changes in stabilisation setpoint.

Due to the atomic and nuclear spins involved, and the presence of isomers, the odd- A spectra obtained for $^{113,115}\text{Pd}$ are complex. The uncertainty on the nuclear spins of both ground state and isomeric states, and on the shape and degree of deformation, make it difficult to make a priori assumptions of the hyperfine structure. Full analysis and interpretation of these has not (yet) been possible, only a short discussion will be given here. The focus is however on the even- A isotopes $^{112,114,116,118}\text{Pd}$, which will be discussed in detail afterwards.

5.3.1 Status of odd- A data

Figure 5.5 shows the (partial) statistics obtained so far for three odd- A isotopes, one the stable ^{105}Pd isotope studied during the offline period, and the $^{113,115}\text{Pd}$ isotopes studied during the fission experiment. The ground state spin of $A = 113$ is predicted to be $5/2^+$, while the isomeric state has a tentative spin assignment of $9/2^-$ and a lifetime of 300 ms (see Fig. 5.5). This would lead to a total hyperfine structure with 29 resonances, 14 from the ground state and 15 from the isomer. Due to the low number of observed peaks and low statistics, it has so far not been possible to determine anything about the hyperfine structure(s). The analysis

of these spectra is still ongoing. The total scanned region spanned from -3700 to 4500 MHz on the scale of Fig. 5.5, with the expected ground-state centroid around -840 MHz based on the measured $^{112,114}\text{Pd}$ centroids, but only the regions with (tentative) peaks are shown. It is possible only one state is seen, due to low population of the other state in the fission production process and/or due to decay losses of the isomer in the RFQ cooler with a holding time of 200 ms.

The ground state of $A = 115$ is predicted to be $1/2^+$, which would give rise to 3 resonances in the combined spectrum, with the isomer predicted as $7/2^-$ contributing 15 resonances. In this spectrum more peaks have been observed, but no definite match to the hyperfine structure(s) has been possible yet. The total scanned region here spanned from -7700 to 3200 MHz, with the ground-state centroid predicted around -990 MHz based on the measured $^{114,116}\text{Pd}$ centroids.

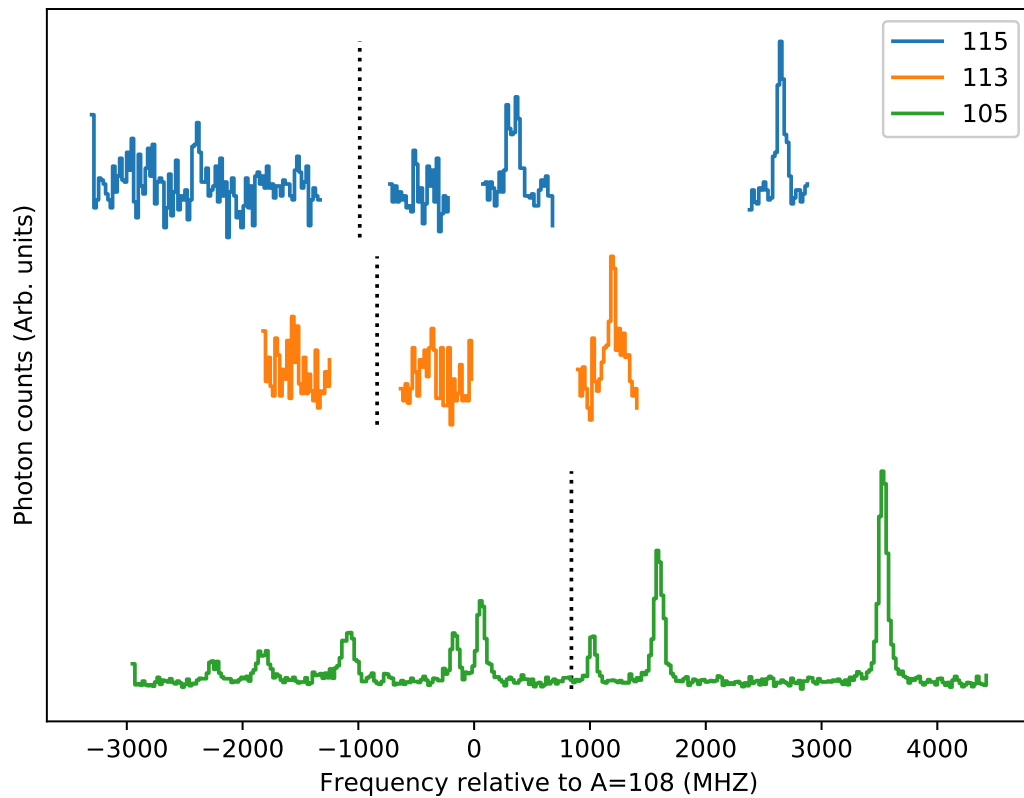


FIGURE 5.5 Overview of the collected spectra for the stable ^{105}Pd and the radioactive $^{113,115}\text{Pd}$. The dotted lines denote the fitted centroid for ^{105}Pd , and the estimated centroids of the ground state structure for $^{113,115}\text{Pd}$ based on the measured $^{112,114,116}\text{Pd}$ centroids.

5.3.2 Data handling

For $A = 112, 114$ two scans per isotope were collected, while for $A = 116$, 28 scans were recorded as it was used as a reference. For each scan, the calibrated voltage

was converted to frequency using Eq. 4.3, with the recorded laser frequency and RFQ cooler voltage, adding an offset of 15 V to the latter which is needed for proper beam energy calibration [107]. The resulting spectrum was then fitted with a Voigt profile (see Eq. 2.26) using the chisquare fitting method from the SATLAS package. The statistical error on the centroid for each scan was determined using a bootstrapping algorithm for $A = 112, 114$ (see next section) due to low number of scans. For $A = 116$ the statistical error on the centroid for each scan was taken as the standard fit error scaled with the reduced chi-square. The final value for the centroid of each isotope was calculated as the weighted mean:

$$\bar{\nu} = \frac{1}{\sum_i^N 1/\sigma_i^2} \sum_i^N \frac{\nu_i}{\sigma_i^2} \quad (5.1)$$

with σ_i the statistical errors. The error on the weighted mean σ was calculated for a dispersion-corrected weighted mean. In this case, σ is scaled with the reduced chi-square

$$\sigma^2 = \frac{1}{\sum_i 1/\sigma_i^2} \cdot \frac{1}{N-1} \sum_i^N \frac{(\nu_i - \bar{\nu})^2}{\sigma_i^2}. \quad (5.2)$$

For $A = 118$ six scans were recorded, but single scans have too low number of counts to be able to fit reliably. Thus in this case, all scans were binned in (calibrated) voltage space, using a bin size of 2 V which was also the used scanning step size (corresponding to ~ 22 MHz), and summed together. The resulting spectrum was fitted with a Voigt profile, and the statistical error determined via bootstrapping. The total statistics collected on all neutron-rich even- A nuclei can be seen in Fig. 5.6.

As asymmetric Voigt profiles, with a tail on the low frequency side, are common in atomic spectra due to inelastic channels in the charge-exchange process [151], spectra of the stable isotopes were checked to investigate if this occurs in this work. An example of a ^{108}Pd spectrum with symmetric Voigt fit and the residuals can be seen in Fig. 5.7. No asymmetry is discernible in the fit or the residuals, and the reduced chi-square of 1.3 gives confidence in the symmetric Voigt profile describing the spectra accurately. The absence of asymmetry might point to a rather low vapour pressure in the charge-exchange cell.

Nine spectra of $A = 108$ were taken over the course of the measurements focused on the even- A isotopes, about one scan after two radioactive ones, as a reference to determine the isotope shifts. These were all fitted separately in the same manner as the neutron-rich isotopes. The final adopted reference frequency is the weighted mean of all the resulting centroids, with the statistical error taken as the dispersion-corrected error on the weighted mean. Isotope shifts were calculated subtracting the resulting centroid of $A = 108$ from the $A = 112, 114, 116, 118$ centroids, using standard error propagation to calculate the statistical errors on the isotope shifts.

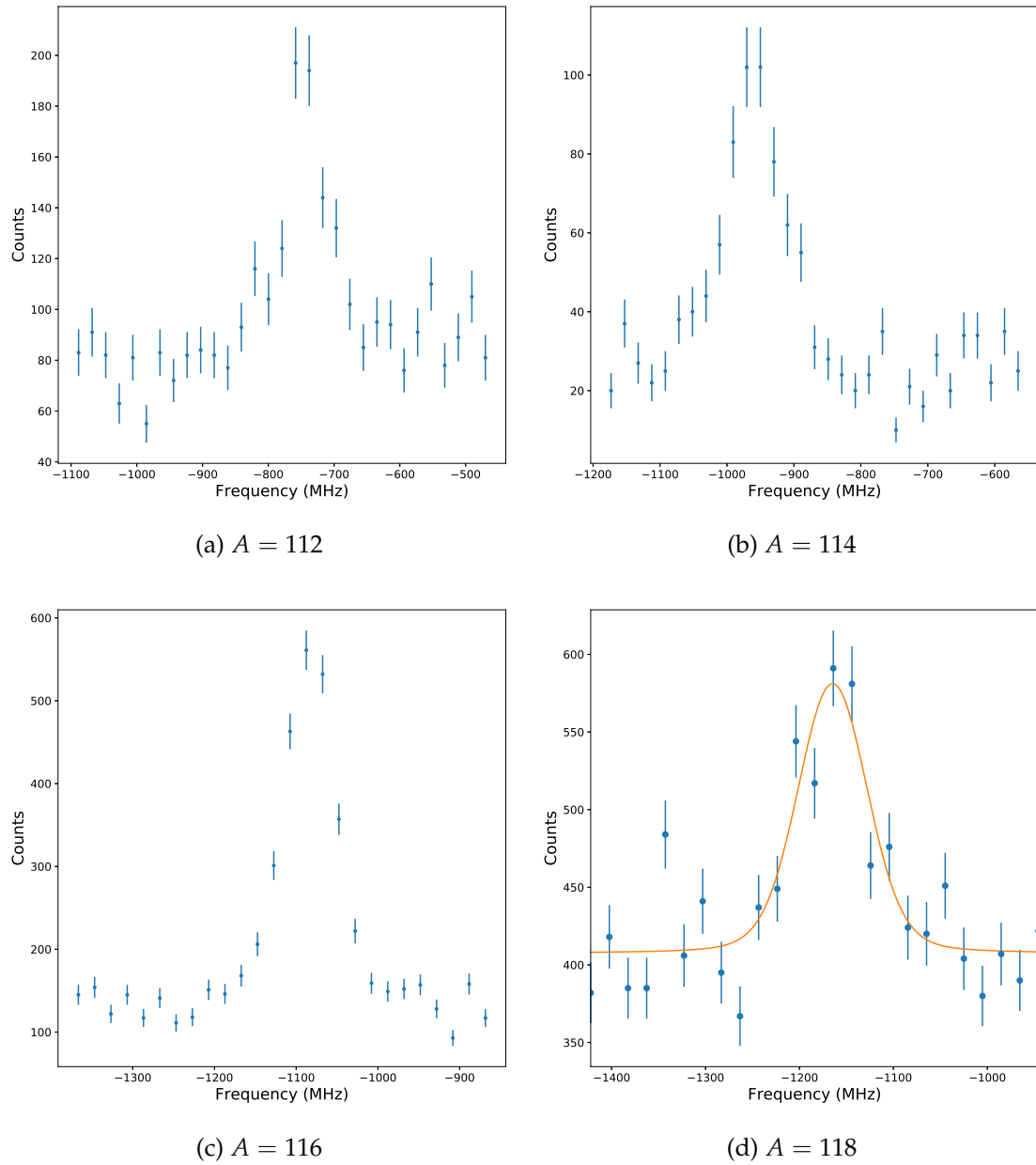


FIGURE 5.6 Overview of total statistics collected for each neutron-rich even- A isotope. Only for $A = 118$ the fit was performed on the summed spectrum, shown in orange. For other isotopes the fit was performed on each separate scan, hence it is not shown here.

Calculating the changes in mean-square charge radii from the isotope shifts is done via Eq. 2.11, using the atomic field and mass shift factors determined via the King plot procedure using the stable isotopes described in section 5.2.

5.3.3 Bootstrapping analysis

In order to assign reliable statistical uncertainties to the determined centroids, a bootstrapping analysis was performed. In statistics, bootstrapping is any test or

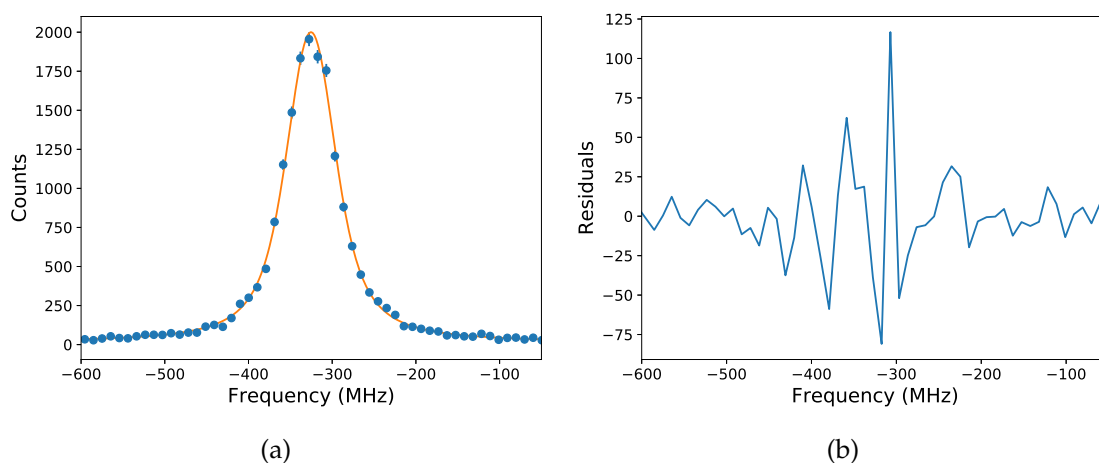


FIGURE 5.7 Spectrum of ^{108}Pd with symmetric Voigt profile fit on the left, and the resulting residuals on the right.

metric that relies on random sampling with replacement. It is an alternative to the ideal case of repeating the experimental measurements many times, in order to find the underlying distribution of parameters. In this case, for an experimental scan with N data points, the algorithm is constructed as follows:

1. Sample N random points from the total data set. Note that this means the same data point can be selected several times.
2. Perform a Voigt profile fit of the randomly sampled data points, and store the resulting fit parameters.
3. Repeat step 1-2 as often as reasonable, here 5000 times.
4. The mean and variance of the fit parameters, e.g. the centroid, can now be estimated from the mean and standard deviations of all stored sample values.

A particular advantage of this approach, is the way outlier points that would normally skew the fit are handled. These outliers, in this case bins with unusually high or low counts, will only infrequently be part of the bootstrap samples, and the final parameter estimate will therefore not be skewed. Parameter estimation using the distribution of the bootstrapped samples is therefore more robust than standard parameter estimation. It also gives the ability to detect asymmetric error bars.

5.3.4 Systematic errors

There are two sources of systematic error on the centroids, one being the wavemeter readout and the other the voltage determination. A systematic error due to the wavemeter needs to be included for the neutron-rich isotopes as not all spectra

were taken at the same laser frequency stabilisation setpoint. This is a fixed 10 MHz error, which is the quoted accuracy according to the 3σ criterion set in the specifications of the wavemeter.

The second source of systematic error is the voltage determination, both of the RFQ cooler and the tuning voltage in the light collection region. The uncertainties on the voltage measurement can be propagated to the fitted centroids in frequency space using the following formula [152, 153]

$$\begin{aligned} \Delta_{\text{sys}}(\delta\nu^{108,A}) &= \nu_L \sqrt{\frac{eV_{\text{RFQ}}}{2m_{108}c^2}} \left[\frac{1}{2} \left(\frac{\delta V_{\text{RFQ}}}{V_{\text{RFQ}}} + \frac{\delta m}{m_{108}} \right) \underbrace{\frac{\Delta V_{\text{RFQ}}}{V_{\text{RFQ}}}}_{10^{-3}} + \frac{\delta V_{\text{LCR}}}{V_{\text{RFQ}}} \underbrace{\frac{\Delta \delta V_{\text{LCR}}}{\delta V_{\text{LCR}}}}_{10^{-4}} + \frac{\Delta m_{108} + \Delta m_A}{m_{108}} \right] \\ &= \nu_L \sqrt{\frac{eV_{\text{RFQ}}}{2m_{108}c^2}} \left[\frac{1}{2} \left(\frac{\delta V_{\text{RFQ}}}{V_{\text{RFQ}}} + \frac{\delta m}{m_{108}} \right) \times 10^{-3} + \frac{\delta V_{\text{LCR}}}{V_{\text{RFQ}}} \times 10^{-4} + \frac{\Delta m_{108} + \Delta m_A}{m_{108}} \right] \end{aligned} \quad (5.3)$$

with V_{RFQ} being the voltage of the RFQ, δV_{LCR} the difference in post-acceleration voltage of the light collection region between isotope A and 108 when on resonance, and $\delta m = |m_A - m_{108}|$ with all masses being the atomic masses and their uncertainties Δm taken from [15]. According to [154, 155], $\Delta V_{\text{RFQ}}/V_{\text{RFQ}} = 10^{-3}$ and $\Delta \delta V_{\text{LCR}}/\delta V_{\text{LCR}} = 10^{-4}$, respectively. In order to obtain $\delta V_{\text{LCR}} = |V_{\text{LCR}}^{108} - V_{\text{LCR}}^A|$, the spectra were fitted as a function of tuning voltage, only for accessing the uncertainty.

These systematic errors are propagated to the changes in mean-square charge radii. The errors on the atomic field and mass shift factors from the linear King plot fit introduce a final systematic error on the changes in mean-square charge radii. The slope (yielding the field shift) and intercept (containing the mass shift) are heavily correlated in the linear fit, with a correlation of -0.999, which is also taken into account when calculating the error on the changes in mean-square charge radii.

5.4 Results and discussion

In Table 5.1 all measured isotope shifts and resulting changes in mean-square charge radii can be found. The total charge radius is also given, calculated using the known radius of ^{108}Pd determined from the combined analysis of muonic X-ray and elastic electron scattering data, $r_{108} = 4.556(3)$ fm [18]. Statistical and systematic errors due to the voltage determination, the wavemeter readout and atomic factors were calculated as detailed in previous sections and are included where needed. As all spectra of the stable isotopes were taken at a fixed laser frequency, no systematic error due to the wavemeter needs to be included.

TABLE 5.1 Isotope shifts and resulting changes in mean-square charge radii for all studied isotopes. The total charge radius is also given based on the known charge radius of ^{108}Pd . Statistical errors in round brackets and systematic errors due to voltage determination in square brackets, systematic errors due to wavemeter readout in angled brackets, systematic errors due to atomic factors in curly brackets are provided.

Isotope	$\delta\nu^{108,A}$ (MHz)	$\delta\langle r^2 \rangle^{108,A}$ (fm ²)	r (fm)
102	1452.8(7)[190]	-0.6610(2)[66]{249}	4.4829(30)[7]{28}
104	958.1(6)[130]	-0.4351(2)[45]{168}	4.5080(30)[5]{19}
105	839.7(9)[100]	-0.3674(3)[35]{211}	4.5155(30)[4]{23}
106	494.7(6)[60]	-0.2220(2)[21]{99}	4.5316(30)[2]{11}
108	0.0	0.0	4.556(3)
110	-436.4(8)[60]	0.2000(3)[21]{68}	4.5779(30)[2]{7}
112	-738(13)[13]{10}	0.352(4)[4]{3}{6}	4.5944(30)[5]{4}{6}
114	-962(13)[13]{10}	0.475(5)[4]{3}{4}	4.6078(30)[5]{4}{5}
116	-1080(14)[12]{10}	0.560(5)[4]{3}{15}	4.6170(30)[4]{4}{16}
118	-1164(13)[18]{10}	0.632(5)[6]{3}{28}	4.6248(30)[7]{4}{31}

The changes in mean-square charge radii are plotted in Fig. 5.8. A smooth variation with N can be seen, except at $A = 105$ where there is a clear sign of OES. There is a parabolic curvature towards higher N , which corresponds to the picture seen in the higher- Z isotopic chains seen on the right of Fig. 5.1. As in the Cd chain, the parabolic trend seems to center around $N = 66$, the middle of the shell, where the largest degree of collectivity and deformation is expected. Measured $B(E2)$ values of Pd isotopes point towards maximum of rotational collectivity at $A = 114$ [156, 157]. No signs of sudden changes in deformation are apparent from the changes in mean-square charge radii.

The results for the even- A isotopes were compared to a range of available calculations using Skyrme EDFs, and newly performed calculations using Fayans functionals. The Skyrme calculations at HFB level were performed as part of the work in [158], and the results are freely available on massexplorer.frib.msu.edu. A comparison between the measured data and three ‘standard’ Skyrme functionals, SkM* [57], SLy4 [58] and SV-min [59], can be seen in Fig. 5.9. SkM* shows a good agreement with the measured changes in mean-square charge radii, while SV-min matches rather well above $A = 108$ but deviates below. SLy4 also deviates below $A = 108$, and strongly for $A = 112, 114$. The latter can be understood from the calculated ground state quadrupole deformation parameters, shown in Fig. 5.10a. SLy4 predicts a change in deformation from prolate to oblate for $A = 112, 114$, which is reflected in the calculated charge radii as well. It is interesting that the SkM* functional matches the total charge radii relatively well, while SV-min is consistently too low. The SkM* functional is a rather old functional, while the more recent SV-min was the Skyrme functional of choice in recent work on charge

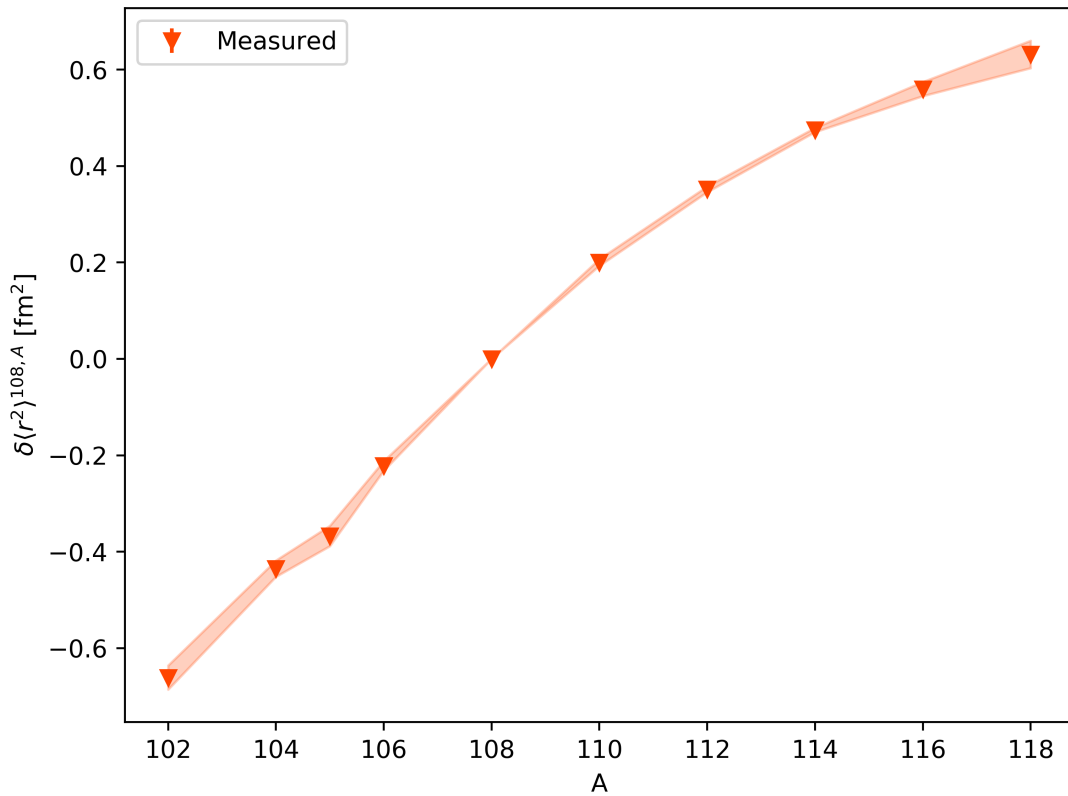


FIGURE 5.8 Changes in mean-square charge radii determined from isotope shifts measured in this work. The shaded area shows the systematic error due to the atomic factors.

radii from laser spectroscopy where it performed relatively well [75, 116, 119]. The discrepancy here might be because SV-min was adjusted to a variety of data on spherical nuclei only.

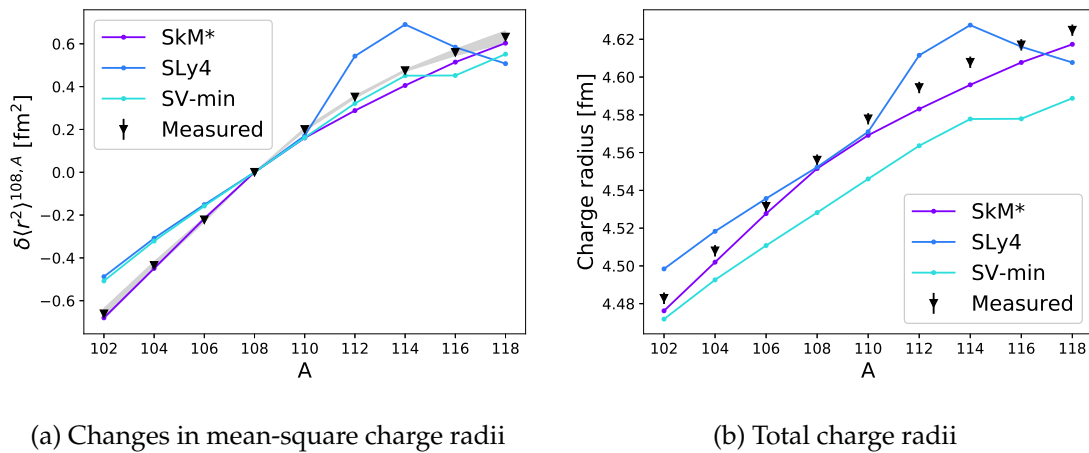


FIGURE 5.9 Comparison between the measured data and 'standard' Skyrme functionals.

The results were also compared to two versions of the Skyrme-type UNEDF functional. In Fig. 5.11 the comparison to the original form UNEDF0 [60], and the

second parameterisation optimised for large deformations using fission properties UNEDF1 [61], can be seen. Both parameterisations reproduce the changes in mean-square radius very well, but not unexpectedly UNEDF1 performs slightly better in calculating the total charge radii. Overall, comparing Figures 5.9, 5.11 and 5.10, there is a correlation between how well the functionals perform in calculating the total charge radii, and the calculated intrinsic deformation parameters. The functionals which perform best in calculating the total charge radii are largely the ones predicting the largest deformation parameters, and the smoothest/slowest transition to the spherical $A = 128$ isotope. It must be noted however that the deformation is not the only determining factor in calculating the charge radii. Other EDF properties, such as shell effects, saturation density and pairing effects, also play an important role.

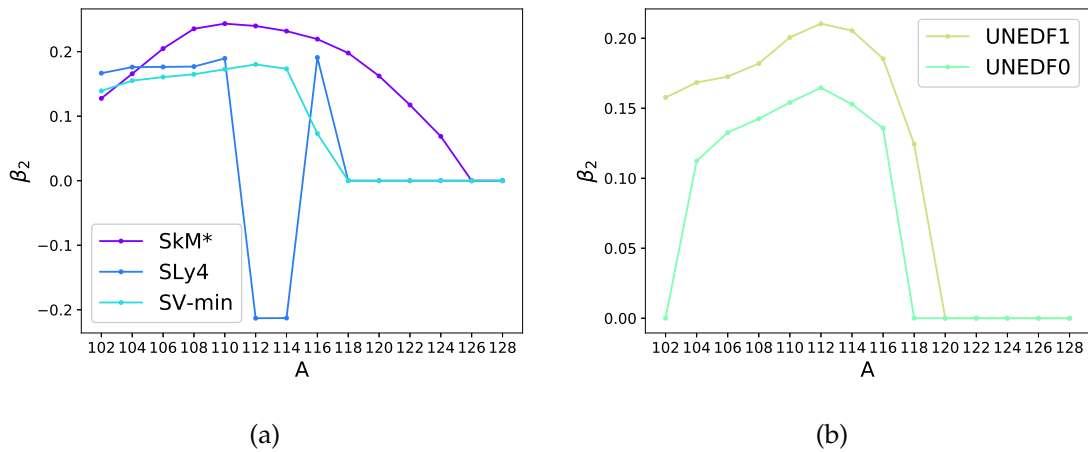


FIGURE 5.10 Calculated quadrupole deformation parameter β_2 up to $N = 82$ using Skyrme functionals. These are plotted beyond the measured data at $A = 118$ to show the evolution to the spherical $A = 128$, the $N = 82$ shell closure.

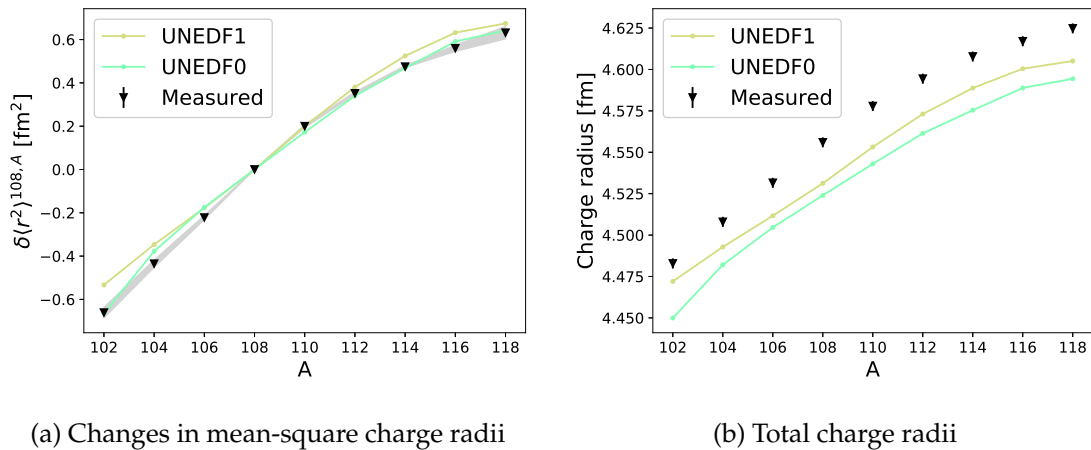


FIGURE 5.11 Comparison between the measured data and Skyrme UNEDF functionals.

Lastly, the results were compared to calculations using two forms of the Fayans functional, performed for this work by Dr M. Kortelainen, with the modified computer code HFBTHO [159], which solves HFB equations in an axially symmetric harmonic oscillator basis. The used EDFs are the Fayans functional $Fy(\text{std})$ introduced in [74], adjusted to spherical nuclei, and the $Fy(\Delta r, \text{HFB})$ parameterisation first used in [75] and discussed in more detail in [160]. As mentioned in section 2.4.2, Fayans functionals have a density gradient term in the pairing functional, but due to $Fy(\text{std})$ being adjusted to the same dataset as SV-min, this term is practically inactive in this parameterisation. To remedy this, a new parameterisation $Fy(\Delta r, \text{BCS})$ was developed, including differential charge radii of calcium isotopes in the parameter adjustment. This parameterisation performs excellently with respect to reproduction of OES of charge radii, as shown in [74, 119]. Both $Fy(\text{std})$ and $Fy(\Delta r, \text{BCS})$ use the BCS approximation to pairing however, so $Fy(\Delta r, \text{HFB})$ using the HFB approach was developed and applied successfully to (proton-rich) calcium isotopes in [75], and also gave excellent results reproducing the kink at the shell closure in Sn isotopes [116].

So far these functionals had not been applied to deformed nuclei such as the Pd isotopes studied in this work. The comparison between the new calculations and the measured data can be seen in Fig. 5.12, also including the calculated deformation parameters up to where calculations were performed at $N = 78$. Both functionals reproduce the changes in mean-square charge radii quite well, but only the $Fy(\Delta r, \text{HFB})$ reproduces the total charge radii properly. This shows the need to ‘activate’ the gradient term in the pairing functional in the case of deformed nuclei to properly reproduce their properties. Further evidence for this can be deduced from comparing the calculated deformation parameters by both Fayans EDFs (Fig. 5.12c) and by the Skyrme EDFs (Fig. 5.10). Even though $Fy(\Delta r, \text{HFB})$ predicts similar or smaller deformation than other functionals, it performs better, showing the importance of pairing in EDFs, and of the surface gradient term in particular.

As part of the DFT calculations, the minimal binding energy is found with respect to the deformation parameter to locate the ground state energy. These curves for Pd isotopes using $Fy(\Delta r, \text{HFB})$ can be seen in Fig. 5.13. Interesting to note is the appearance of a weak second local minimum in the binding energy curve on the oblate side from about $A = 110$ onwards. This might explain why some other calculations predict an oblate ground state, as the two minima are rather close in energy for some isotopes, and could easily be reversed in other theoretical approaches (e.g. the SLy4 EDF). In general the absolute minimum is rather broad for most isotopes, which would suggest the nuclei are fairly soft in deformation. To obtain more certainty on the magnitude and sign of the deformation, electric quadrupole moments extracted from the hyperfine structure of the odd- A neutron-rich cases would be needed.

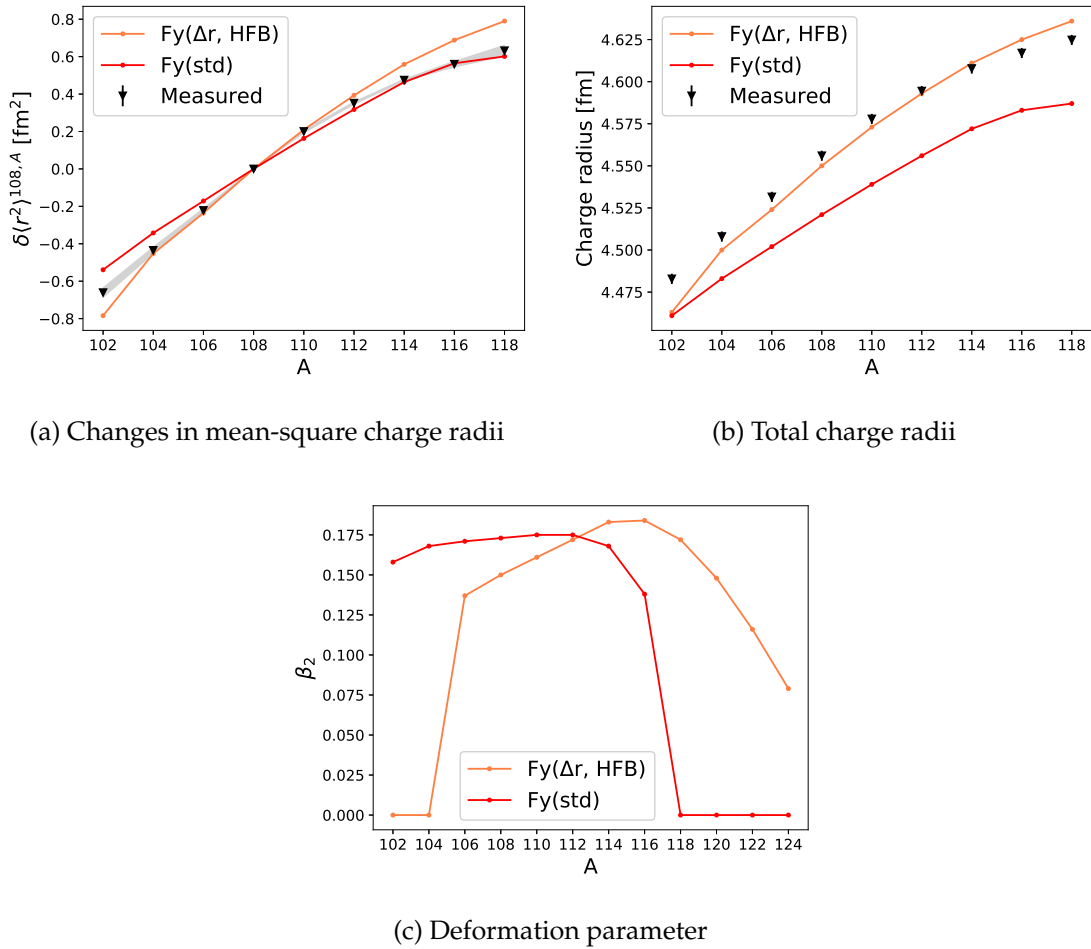


FIGURE 5.12 Comparison between the measured data and Fayans functionals, and the calculated quadrupole deformation parameters.

5.5 Outlook

The work presented here is the first time laser spectroscopy has been performed on radioactive Pd isotopes. The results and the comparison to the new Fayans EDF calculations will be prepared for publishing soon. Now that all the preparation and the first experiment is done, possibilities remain for further studies of the Pd chain at IGISOL. Additional beam time may be spent to fill in remaining gaps in the $A = 113, 115$ spectra, in order to try to determine nuclear charge radii, moments and spins. From the measured changes in mean-square charge radii in this work, it seems unlikely that there is a sudden change in deformation along the chain as predicted in the theoretical work [138] or deduced from decay spectroscopy studies [125, 128, 132, 134]. However, the electric quadrupole moments from the odd- A isotopes would be needed to verify, and to pin down the exact shape. Separately, an experimental proposal to study neutron-deficient isotopes using fusion-evaporation reactions has recently been submitted, with one of its aims the

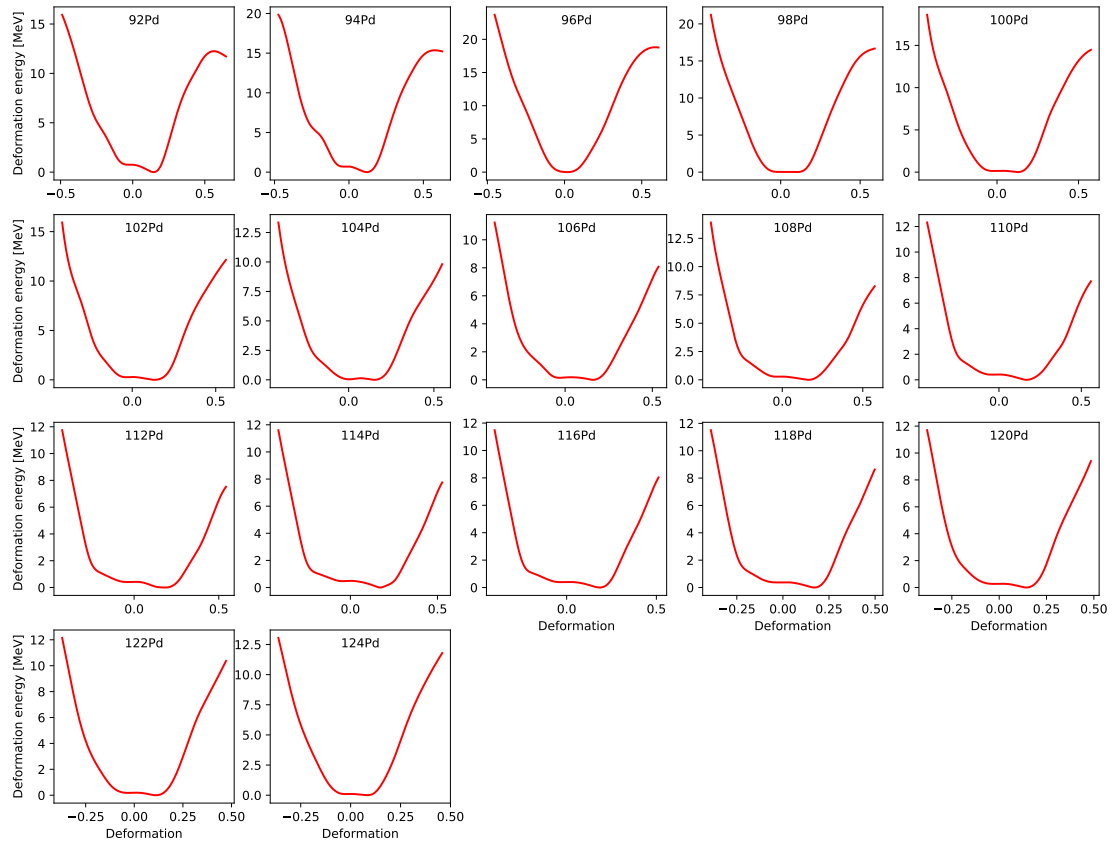


FIGURE 5.13 Calculated deformation energy curves, as a function of deformation, quantified by the intrinsic deformation parameter β_2 , for Pd isotopes using $Fy(\Delta r, \text{HFB})$. Zero energy corresponds to the HFB energy minimum. Figure courtesy of M. Kortelainen.

further study of the trend in charge radii.

Pushing out towards even more exotic isotopes both on the neutron-rich and neutron-deficient side of the valley of beta stability requires more sensitive techniques than collinear laser spectroscopy. There are plans to study the very neutron-deficient isotopes, towards the shell closure at $N = 50$, using resonant ionisation laser spectroscopy in a hot cavity. This technique was recently successfully applied to neutron-deficient Ag isotopes. On the neutron-rich side, the RAPTOR (RIS And Purification Traps for Optimised spectRoscopy) technique and setup currently under development could provide the opportunity to go further than $A = 118$. This would show if the changes in mean-square charge radii would start to decrease going towards the $N = 82$ shell closure, as is the case for lower- Z mid-shell nuclei when going towards the $N = 50$ shell closure (see left of Fig. 5.1). All of these results would allow even more stringent tests of state-of-the-art nuclear theory, such as the newly developed Fayans EDFs.

6 SUMMARY AND OUTLOOK

This thesis has presented various technical developments for high-resolution laser spectroscopy at the IGISOL facility. A saturated absorption spectroscopy setup was used to provide a frequency reference for the FSR calibration of two FPIs, characterising them, and investigating methods of frequency stabilisation. Frequency determination using the fully calibrated and characterised FPIs will be of importance for future experiments using a pulsed injection-locked Ti:sapphire laser and/or pulsed dual-etalon Ti:sapphire laser.

The work on frequency stabilisation was done for the purpose of collinear laser spectroscopy. Stabilisation to a Rb hyperfine peak and to the WSU-10 wavemeter was investigated. Frequency stabilisation using a transfer cavity was also set up and characterised. This was also linked to testing of the WSU-10 wavemeter in a collaboration with different institutes to better understand the performance and systematic errors of commercial wavemeters. Tests are planned using the saturated absorption spectroscopy setup to stabilise the Matisse cw Ti:sapphire laser to a Rb hyperfine peak, and have the stabilised Matisse cw Ti:sapphire laser replace the HeNe laser as reference for the transfer cavity. If this looks promising, a diode laser would be acquired to stabilise to the Rb hyperfine peak and act as a general frequency reference in the collinear laser laboratory.

In a broader context these technical developments towards accurate and precise frequency determination and stabilisation are crucial, as laser spectroscopy techniques are continuously improved to have higher resolution and better sensitivity. This will allow future high-resolution work on more exotic isotopes with low production yields, thus requiring long-term measurements, using both scanning of the laser frequency and frequency-stabilised lasers.

The developments on laser stabilisation, in combination with upgrades to the collinear laser spectroscopy beamline in general, especially the installation of the

charge-exchange cell, allowed the study of Pd isotopes. Preparatory work on stable isotopes was conducted on five different atomic transitions, which allowed a comparison with level population predictions from charge-exchange calculations. This then led to the first optical spectroscopy experiment on exotic Pd isotopes.

The experiment on neutron-rich Pd isotopes was largely motivated by the open questions on the nature of the deformation, its evolution and possible rapid shape changes or coexistence in the Pd chain, coming from decay spectroscopy studies. There is also a lack of firm spin assignments for both ground and isomeric states in the odd- A neutron-rich isotopes. In this thesis, the changes in mean-square charge radii for $^{112,114,116,118}\text{Pd}$ could be extracted from the measured isotope shifts using the atomic factors determined in the work on stable isotopes. These showed a smooth parabolic variation with N , with no clear signs of a rapid shape change. The total charge radii, calculated using the known charge radius of ^{108}Pd , were compared to literature results from various Skyrme-type EDFs, and new calculations using two recently developed Fayans EDFs, $Fy(\text{std})$ and $Fy(\Delta r, \text{HFB})$. The $Fy(\Delta r, \text{HFB})$ EDF reproduces the total charge radii excellently, showing the need for the surface gradient term in the pairing functional for proper calculations of charge radii.

Figure 5.1 has been updated with new results available since the publication of [31], see Fig. 6.1. In addition to the recent results on Cd [119] and Sn [116], and the results of Pd, it includes the preliminary results from IGISOL of neutron-rich Ag isotopes studied with collinear laser spectroscopy, and of neutron-deficient Ag isotopes studied with resonant laser ionisation spectroscopy in a hot cavity [161] combined with the mass purification capabilities of the JYFTRAP Penning trap and the detection of ions using the PI-ICR technique [162].

In Fig. 6.1 the transition from the almost linear trend in Sn to a more and more pronounced parabolic curvature towards Pd is clear. This shows the increase in core polarisation and deformation when moving away from the $Z = 50$ closed shell. The different slope of the Ag chain compared to the other chains is most likely due to inaccurate calculations of the atomic factors. Finalising the data analysis of the neutron-rich odd- A isotopes, possibly with extra data-taking using remaining beamtime, will hopefully allow information on the nuclear moments to be extracted from the hyperfine structure. In particular the electric quadrupole moments would be of interest, as they would give further information on the precise shape and the softness of the deformation in neutron-rich Pd isotopes. Additionally, the isotope shifts of the odd- A isotopes would give details on the OES in the changes of mean-square charge radii.

The planned experiment on neutron-deficient Pd isotopes, and the future plans going further neutron-rich with the RAPTOR setup, will support a firmer discernment in the trend in the changes in mean-square charge radii between the two

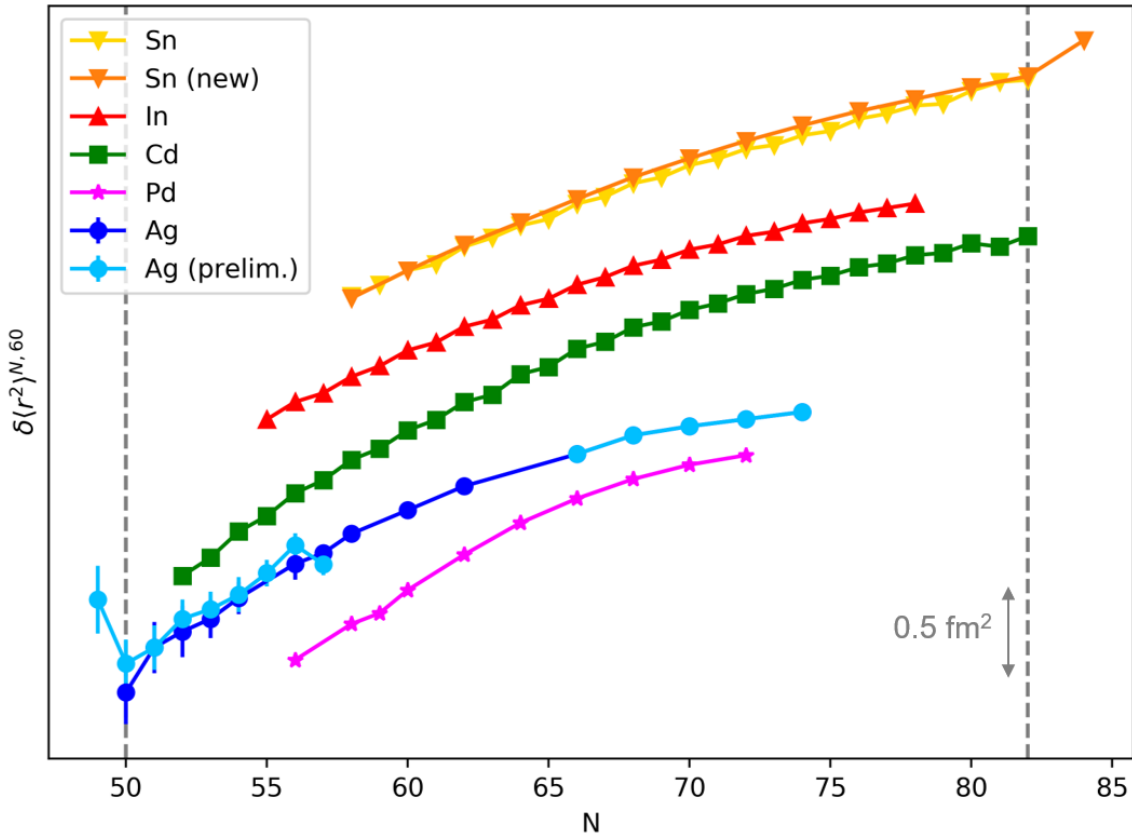


FIGURE 6.1 Overview of changes in mean-square charge radii as a function of neutron number in the Pd to Sn region. Figure updated from [31], with new data on Cd [119] and even Sn [116], preliminary results for Ag from IGISOL [163,164], and the Pd results from this work. Isotope chains have been offset by 0.5 fm^2 .

neutron shell closures at $N = 50$ and $N = 82$. Resonant laser ionisation in the hot cavity combined with the PI-ICR technique might enable the crossing of the $N = 50$ shell closure to investigate the possible occurrence of a kink as seen at $N = 82$ in Sn isotopes or at $N = 50$ in the preliminary Ag results. Most recently, an experimental proposal to study Tc isotopes at IGISOL has been submitted to the JYFL Programme Advisory Committee, in order to continue the research programme aimed at filling in the gap in optical spectroscopy data in this refractory region. Upgrades to the collinear laser spectroscopy beamline are planned to support this research, e.g. the installation of a new electrode based on the design in [165] to counteract the beam steering issues currently noticed when using the CEC.

REFERENCES

- [1] O. Sorlin and M.-G. Porquet. *Progress in Particle and Nuclear Physics*, **61**, 602 (2008). [doi:10.1016/j.pnpnp.2008.05.001](https://doi.org/10.1016/j.pnpnp.2008.05.001).
- [2] H. J. Wollersheim, H. Emling, H. Grein et al. *Nuclear Physics A*, **556**, 261 (1993). [doi:10.1016/0375-9474\(93\)90351-W](https://doi.org/10.1016/0375-9474(93)90351-W).
- [3] K. Heyde and J. L. Wood. *Rev. Mod. Phys.*, **83**, 1467 (2011). [doi:10.1103/RevModPhys.83.1467](https://doi.org/10.1103/RevModPhys.83.1467).
- [4] R. Neugart, J. Billowes, M. L. Bissell et al. *Journal of Physics G: Nuclear and Particle Physics*, **44**, 064002 (2017). [doi:10.1088/1361-6471/aa6642](https://doi.org/10.1088/1361-6471/aa6642).
- [5] T. E. Cocolios, R. P. de Groote, J. Billowes et al. *Nuclear Instruments and Methods in Physics Research Section B: Beam Interactions with Materials and Atoms*, **376**, 284 (2016). [doi:10.1016/j.nimb.2015.11.024](https://doi.org/10.1016/j.nimb.2015.11.024).
- [6] K. Minamisono, P. F. Mantica, A. Klose et al. *Nuclear Instruments and Methods in Physics Research Section A: Accelerators, Spectrometers, Detectors and Associated Equipment*, **709**, 85 (2013). [doi:10.1016/j.nima.2013.01.038](https://doi.org/10.1016/j.nima.2013.01.038).
- [7] A. Voss, T. J. Procter, O. Shelbaya et al. *Nuclear Instruments and Methods in Physics Research Section A: Accelerators, Spectrometers, Detectors and Associated Equipment*, **811**, 57 (2016). [doi:10.1016/j.nima.2015.11.145](https://doi.org/10.1016/j.nima.2015.11.145).
- [8] B. Maaß, P. Müller, W. Nörtershäuser et al. *Hyperfine Interactions*, **238**, 25 (2017). [doi:10.1007/s10751-017-1399-5](https://doi.org/10.1007/s10751-017-1399-5).
- [9] S. Franchoo, M. Cheikh Mhamed, R. Li et al. *EPJ Web Conf.*, **193**, 04012 (2018). [doi:10.1051/epjconf/201819304012](https://doi.org/10.1051/epjconf/201819304012).
- [10] W. Nörtershäuser and P. Campbell. *Hyperfine Interactions*, **171**, 149 (2007). [doi:10.1007/s10751-006-9492-1](https://doi.org/10.1007/s10751-006-9492-1).
- [11] M. Lewitowicz. *Journal of Physics: Conference Series*, **312**, 052014 (2011). [doi:10.1088/1742-6596/312/5/052014](https://doi.org/10.1088/1742-6596/312/5/052014).
- [12] G. Neyens. *Reports on Progress in Physics*, **66**, 633 (2003). [doi:10.1088/0034-4885/66/4/205](https://doi.org/10.1088/0034-4885/66/4/205).
- [13] C. Schwartz. *Phys. Rev.*, **97**, 380 (1955). [doi:10.1103/PhysRev.97.380](https://doi.org/10.1103/PhysRev.97.380).
- [14] W. H. King. *Isotope shifts in atomic spectra*. Plenum, New York (1984).
- [15] M. Wang, G. Audi, F. G. Kondev et al. *Chinese Physics C*, **41**, 030003 (2017). [doi:10.1088/1674-1137/41/3/030003](https://doi.org/10.1088/1674-1137/41/3/030003).

- [16] E. C. Seltzer. *Phys. Rev.*, **188**, 1916 (1969). [doi:10.1103/PhysRev.188.1916](https://doi.org/10.1103/PhysRev.188.1916).
- [17] B. Cheal, T. E. Cocolios and S. Fritzsche. *Phys. Rev. A*, **86**, 042501 (2012). [doi:10.1103/PhysRevA.86.042501](https://doi.org/10.1103/PhysRevA.86.042501).
- [18] G. Fricke and K. Heilig. *Nuclear Charge Radii*. Landolt-Börnstein/Springer, Berlin (2004).
- [19] R. B. Cakirli, R. F. Casten and K. Blaum. *Phys. Rev. C*, **82**, 061306 (2010). [doi:10.1103/PhysRevC.82.061306](https://doi.org/10.1103/PhysRevC.82.061306).
- [20] I. Angeli and K. P. Marinova. *Journal of Physics G: Nuclear and Particle Physics*, **42**, 055108 (2015). [doi:10.1088/0954-3899/42/5/055108](https://doi.org/10.1088/0954-3899/42/5/055108).
- [21] B. H. Sun, C. Y. Liu and H. X. Wang. *Phys. Rev. C*, **95**, 014307 (2017). [doi:10.1103/PhysRevC.95.014307](https://doi.org/10.1103/PhysRevC.95.014307).
- [22] P. H. Stelson and L. Grodzins. *Nuclear Data Sheets. Section A*, **1**, 21 (1965). [doi:10.1016/S0550-306X\(65\)80004-0](https://doi.org/10.1016/S0550-306X(65)80004-0).
- [23] I. Angeli and K. P. Marinova. *Atomic Data and Nuclear Data Tables*, **99**, 69 (2013). [doi:10.1016/j.adt.2011.12.006](https://doi.org/10.1016/j.adt.2011.12.006).
- [24] I. Angeli, Y. P. Gangrsky, K. P. Marinova et al. *Journal of Physics G: Nuclear and Particle Physics*, **36**, 085102 (2009). [doi:10.1088/0954-3899/36/8/085102](https://doi.org/10.1088/0954-3899/36/8/085102).
- [25] G. Ulm, S. K. Bhattacharjee, P. Dabkiewicz et al. *Zeitschrift für Physik A Atomic Nuclei*, **325**, 247 (1986). [doi:10.1007/BF01294605](https://doi.org/10.1007/BF01294605).
- [26] B. A. Marsh, T. D. Goodacre, S. Sels et al. *Nature Physics*, **14**, 1163 (2018). [doi:10.1038/s41567-018-0292-8](https://doi.org/10.1038/s41567-018-0292-8).
- [27] E. Verstraelen, A. Teigelhöfer, W. Ryssens et al. *Phys. Rev. C*, **100**, 044321 (2019). [doi:10.1103/PhysRevC.100.044321](https://doi.org/10.1103/PhysRevC.100.044321).
- [28] R. C. Barrett. *Reports on Progress in Physics*, **37**, 1 (1974). [doi:10.1088/0034-4885/37/1/001](https://doi.org/10.1088/0034-4885/37/1/001).
- [29] K. Tsukada, A. Enokizono, T. Ohnishi et al. *Phys. Rev. Lett.*, **118**, 262501 (2017). [doi:10.1103/PhysRevLett.118.262501](https://doi.org/10.1103/PhysRevLett.118.262501).
- [30] E. W. Otten, *Nuclear radii and moments of unstable isotopes*. In *Treatise on heavy ion science*, pages 517–638. Springer (1989).
- [31] P. Campbell, I. D. Moore and M. R. Pearson. *Progress in Particle and Nuclear Physics*, **86**, 127 (2016). [doi:10.1016/j.pnpnp.2015.09.003](https://doi.org/10.1016/j.pnpnp.2015.09.003).
- [32] N. J. Stone. *Hyperfine Interactions*, **230**, 7 (2015). [doi:10.1007/s10751-014-1094-8](https://doi.org/10.1007/s10751-014-1094-8).

- [33] J. R. Persson. *Atomic Data and Nuclear Data Tables*, **99**, 62 (2013). [doi:10.1016/j.adt.2012.04.002](https://doi.org/10.1016/j.adt.2012.04.002).
- [34] J. J. Olivero and R. L. Longbothum. *Journal of Quantitative Spectroscopy and Radiative Transfer*, **17**, 233 (1977). [doi:10.1016/0022-4073\(77\)90161-3](https://doi.org/10.1016/0022-4073(77)90161-3).
- [35] W. Demtröder. *Laser Spectroscopy 1: Basic Principles*. Springer, 5th edition (2014).
- [36] G. F. Bertsch, D. J. Dean and W. Nazarewicz. *SciDAC Review*, **6** (2007).
- [37] K. Hebel (2020). Preprint v1, [arXiv:2002.09548](https://arxiv.org/abs/2002.09548).
- [38] H. Hergert, S. K. Bogner, T. D. Morris, A. Schwenk and K. Tsukiyama. *Physics Reports*, **621**, 165 (2016). [doi:10.1016/j.physrep.2015.12.007](https://doi.org/10.1016/j.physrep.2015.12.007).
- [39] G. Hagen, T. Papenbrock, M. Hjorth-Jensen and D. J. Dean. *Reports on Progress in Physics*, **77**, 096302 (2014). [doi:10.1088/0034-4885/77/9/096302](https://doi.org/10.1088/0034-4885/77/9/096302).
- [40] B. R. Barrett, P. Navrátil and J. P. Vary. *Progress in Particle and Nuclear Physics*, **69**, 131 (2013). [doi:10.1016/j.ppnp.2012.10.003](https://doi.org/10.1016/j.ppnp.2012.10.003).
- [41] W. H. Dickhoff and C. Barbieri. *Progress in Particle and Nuclear Physics*, **52**, 377 (2004). [doi:10.1016/j.ppnp.2004.02.038](https://doi.org/10.1016/j.ppnp.2004.02.038).
- [42] D. Lee. *Progress in Particle and Nuclear Physics*, **63**, 117 (2009). [doi:10.1016/j.ppnp.2008.12.001](https://doi.org/10.1016/j.ppnp.2008.12.001).
- [43] S. C. Pieper and R. B. Wiringa. *Annual Review of Nuclear and Particle Science*, **51**, 53 (2001). [doi:10.1146/annurev.nucl.51.101701.132506](https://doi.org/10.1146/annurev.nucl.51.101701.132506).
- [44] J. D. Holt, S. R. Stroberg, A. Schwenk and J. Simonis (2019). Preprint v1, [arXiv:1905.10475](https://arxiv.org/abs/1905.10475).
- [45] G. Hagen, G. R. Jansen and T. Papenbrock. *Phys. Rev. Lett.*, **117**, 172501 (2016). [doi:10.1103/PhysRevLett.117.172501](https://doi.org/10.1103/PhysRevLett.117.172501).
- [46] T. D. Morris, J. Simonis, S. R. Stroberg et al. *Phys. Rev. Lett.*, **120**, 152503 (2018). [doi:10.1103/PhysRevLett.120.152503](https://doi.org/10.1103/PhysRevLett.120.152503).
- [47] L. Coraggio, A. Covello, A. Gargano, N. Itaco and T. T. S. Kuo. *Progress in Particle and Nuclear Physics*, **62**, 135 (2009). [doi:10.1016/j.ppnp.2008.06.001](https://doi.org/10.1016/j.ppnp.2008.06.001).
- [48] E. Teruya, K. Higashiyama and N. Yoshinaga. *Phys. Rev. C*, **93**, 064327 (2016). [doi:10.1103/PhysRevC.93.064327](https://doi.org/10.1103/PhysRevC.93.064327).
- [49] M. G. Mayer and J. H. D. Jensen. *Elementary Theory of Nuclear Shell Structure*. Structure of matter series. Wiley (1955).

- [50] R. D. Woods and D. S. Saxon. *Phys. Rev.*, **95**, 577 (1954). [doi:10.1103/PhysRev.95.577](https://doi.org/10.1103/PhysRev.95.577).
- [51] D. R. Hartree. *Mathematical Proceedings of the Cambridge Philosophical Society*, **24**, 111–132 (1928). [doi:10.1017/S0305004100011920](https://doi.org/10.1017/S0305004100011920).
- [52] V. Fock. *Zeitschrift für Physik*, **61**, 126 (1930). [doi:10.1007/BF01340294](https://doi.org/10.1007/BF01340294).
- [53] J. Bardeen, L. N. Cooper and J. R. Schrieffer. *Physical Review*, **106**, 162 (1957). [doi:10.1103/PhysRev.106.162](https://doi.org/10.1103/PhysRev.106.162).
- [54] N. N. Bogoliubov. *Soviet Physics JETP*, **34**, 41 (1958).
- [55] T. H. R. Skyrme. *Nuclear Physics*, **9**, 615 (1958). [doi:10.1016/0029-5582\(58\)90345-6](https://doi.org/10.1016/0029-5582(58)90345-6).
- [56] M. Bender, P.-H. Heenen and P.-G. Reinhard. *Rev. Mod. Phys.*, **75**, 121 (2003). [doi:10.1103/RevModPhys.75.121](https://doi.org/10.1103/RevModPhys.75.121).
- [57] J. Bartel, P. Quentin, M. Brack, C. Guet and H.-B. Håkansson. *Nuclear Physics A*, **386**, 79 (1982). [doi:10.1016/0375-9474\(82\)90403-1](https://doi.org/10.1016/0375-9474(82)90403-1).
- [58] E. Chabanat, P. Bonche, P. Haensel, J. Meyer and R. Schaeffer. *Nuclear Physics A*, **635**, 231 (1998). [doi:10.1016/S0375-9474\(98\)00180-8](https://doi.org/10.1016/S0375-9474(98)00180-8).
- [59] P. Klüpfel, P.-G. Reinhard, T. J. Bürvenich and J. A. Maruhn. *Phys. Rev. C*, **79**, 034310 (2009). [doi:10.1103/PhysRevC.79.034310](https://doi.org/10.1103/PhysRevC.79.034310).
- [60] M. Kortelainen, T. Lesinski, J. Moré et al. *Phys. Rev. C*, **82**, 024313 (2010). [doi:10.1103/PhysRevC.82.024313](https://doi.org/10.1103/PhysRevC.82.024313).
- [61] M. Kortelainen, J. McDonnell, W. Nazarewicz et al. *Phys. Rev. C*, **85**, 024304 (2012). [doi:10.1103/PhysRevC.85.024304](https://doi.org/10.1103/PhysRevC.85.024304).
- [62] M. Kortelainen, J. McDonnell, W. Nazarewicz et al. *Phys. Rev. C*, **89**, 054314 (2014). [doi:10.1103/PhysRevC.89.054314](https://doi.org/10.1103/PhysRevC.89.054314).
- [63] J. Dechargé and D. Gogny. *Phys. Rev. C*, **21**, 1568 (1980). [doi:10.1103/PhysRevC.21.1568](https://doi.org/10.1103/PhysRevC.21.1568).
- [64] J. F. Berger, M. Girod and D. Gogny. *Nuclear Physics A*, **428**, 23 (1984). [doi:10.1016/0375-9474\(84\)90240-9](https://doi.org/10.1016/0375-9474(84)90240-9).
- [65] F. Chappert, M. Girod and S. Hilaire. *Physics Letters B*, **668**, 420 (2008). [doi:10.1016/j.physletb.2008.09.017](https://doi.org/10.1016/j.physletb.2008.09.017).
- [66] S. Goriely, S. Hilaire, M. Girod and S. Péru. *Phys. Rev. Lett.*, **102**, 242501 (2009). [doi:10.1103/PhysRevLett.102.242501](https://doi.org/10.1103/PhysRevLett.102.242501).

- [67] P. Hohenberg and W. Kohn. *Phys. Rev.*, **136**, B864 (1964). [doi:10.1103/PhysRev.136.B864](https://doi.org/10.1103/PhysRev.136.B864).
- [68] W. Kohn and L. J. Sham. *Phys. Rev.*, **140**, A1133 (1965). [doi:10.1103/PhysRev.140.A1133](https://doi.org/10.1103/PhysRev.140.A1133).
- [69] S. A. Fayans. *Journal of Experimental and Theoretical Physics Letters*, **68**, 169 (1998). [doi:10.1134/1.567841](https://doi.org/10.1134/1.567841).
- [70] S. A. Fayans and D. Zawischa. *Physics Letters B*, **383**, 19 (1996). [doi:10.1016/0370-2693\(96\)00716-2](https://doi.org/10.1016/0370-2693(96)00716-2).
- [71] S. A. Fayans, S. V. Tolokonnikov, E. L. Trykov and D. Zawischa. *Nuclear Physics A*, **676**, 49 (2000). [doi:10.1016/S0375-9474\(00\)00192-5](https://doi.org/10.1016/S0375-9474(00)00192-5).
- [72] I. N. Borzov, S. A. Fayans, E. Krömer and D. Zawischa. *Zeitschrift für Physik A Hadrons and Nuclei*, **355**, 117 (1996). [doi:10.1007/BF02769674](https://doi.org/10.1007/BF02769674).
- [73] S. V. Tolokonnikov and E. E. Saperstein. *Physics of Atomic Nuclei*, **73**, 1684 (2010). [doi:10.1134/S1063778810100054](https://doi.org/10.1134/S1063778810100054).
- [74] P.-G. Reinhard and W. Nazarewicz. *Phys. Rev. C*, **95**, 064328 (2017). [doi:10.1103/PhysRevC.95.064328](https://doi.org/10.1103/PhysRevC.95.064328).
- [75] A. J. Miller, K. Minamisono, A. Klose et al. *Nature Physics*, **15**, 432 (2019). [doi:10.1038/s41567-019-0416-9](https://doi.org/10.1038/s41567-019-0416-9).
- [76] T. Nikšić, D. Vretenar and P. Ring. *Progress in Particle and Nuclear Physics*, **66**, 519 (2011). [doi:10.1016/j.pnpnp.2011.01.055](https://doi.org/10.1016/j.pnpnp.2011.01.055).
- [77] W. Demtröder. *Laser Spectroscopy 2: Experimental Techniques*. Springer, 5th edition (2014).
- [78] S. Nakayama. *Japanese Journal of Applied Physics*, **24**, 1 (1985). [doi:10.1143/jjap.24.1](https://doi.org/10.1143/jjap.24.1).
- [79] O. Schmidt, K.-M. Knaak, R. Wynands and D. Meschede. *Applied Physics B*, **59**, 167 (1994). [doi:10.1007/BF01081167](https://doi.org/10.1007/BF01081167).
- [80] D. A. Steck. *Rubidium 85 D line data*. <http://steck.us/alkalidata>. (revision 2.2.1, 21 November 2019).
- [81] D. A. Steck. *Rubidium 87 D line data*. <http://steck.us/alkalidata>. (revision 2.2.1, 21 November 2019).
- [82] D. M. Kane and M. H. Dunn. *Optics Communications*, **50**, 219 (1984). [doi:10.1016/0030-4018\(84\)90321-3](https://doi.org/10.1016/0030-4018(84)90321-3).
- [83] S. Bouazza, D. S. Gough, P. Hannaford, R. M. Lowe and M. Wilson. *Phys. Rev. A*, **63**, 012516 (2000). [doi:10.1103/PhysRevA.63.012516](https://doi.org/10.1103/PhysRevA.63.012516).

- [84] V. Bernard, C. Daussy, G. Nogues et al. *IEEE Journal of Quantum Electronics*, **33**, 1282 (1997). doi:10.1109/3.605548.
- [85] S. Geldhof. *Development of a saturated absorption spectroscopy setup at IGISOL*. Master's thesis, KU Leuven (2015).
- [86] V. Sonnenschein, I. D. Moore, S. Raeder et al. *Laser Physics*, **27**, 085701 (2017). doi:10.1088/1555-6611/aa7834.
- [87] W. C. Michels and N. L. Curtis. *Review of Scientific Instruments*, **12**, 444 (1941). doi:10.1063/1.1769919.
- [88] A. M. Ibrahim. *Saturation Absorption Spectroscopy on Cs Atoms*. Master's thesis, University of Eastern Finland (2016).
- [89] H. Khan. *Fabry-Perot Interferometer; construction, calibration and development*. Master's thesis, University of Jyväskylä (2015).
- [90] J. E. Sansonetti. *Journal of Physical and Chemical Reference Data*, **38**, 761 (2009). doi:10.1063/1.3132702.
- [91] S. B. Bayram, P. Arndt, O. I. Popov et al. *Phys. Rev. A*, **90**, 062510 (2014). doi:10.1103/PhysRevA.90.062510.
- [92] *Le Système international d'unités / The International System of Units ('The SI Brochure')*. Bureau international des poids et mesures, ninth edition (2019). URL bipm.org/en/publications/si-brochure/.
- [93] National Instruments. *LabVIEW 2018 Help - PID Algorithms* (2018). http://zone.ni.com/reference/en-XX/help/371361R-01/lvpidmain/pid_algs/.
- [94] V. Sonnenschein, I. D. Moore, H. Khan, I. Pohjalainen and M. Reponen. *Hyperfine Interactions*, **227**, 113 (2014). doi:10.1007/s10751-013-1000-9.
- [95] A. Gade and B. M. Sherrill. *Physica Scripta*, **91**, 053003 (2016). doi:10.1088/0031-8949/91/5/053003.
- [96] S. Hofmann and G. Münzenberg. *Rev. Mod. Phys.*, **72**, 733 (2000). doi:10.1103/RevModPhys.72.733.
- [97] Y. Yano. *Nuclear Instruments and Methods in Physics Research Section B: Beam Interactions with Materials and Atoms*, **261**, 1009 (2007). doi:10.1016/j.nimb.2007.04.174.
- [98] M. J. G. Borge and B. Jonson. *Journal of Physics G: Nuclear and Particle Physics*, **44**, 044011 (2017). doi:10.1088/1361-6471/aa5f03.
- [99] G. C. Ball, G. Hackman and R. Krücken. *Physica Scripta*, **91**, 093002 (2016). doi:10.1088/0031-8949/91/9/093002.

- [100] J. Ärje, J. Äystö, H. Hyvönen et al. *Nuclear Instruments and Methods in Physics Research Section A: Accelerators, Spectrometers, Detectors and Associated Equipment*, **247**, 431 (1986). doi:10.1016/0168-9002(86)90404-3.
- [101] I. D. Moore, P. Dendooven and J. Ärje. *Hyperfine Interactions*, **223**, 17 (2014). doi:10.1007/s10751-013-0871-0.
- [102] P. Karvonen, I. D. Moore, T. Sonoda et al. *Nuclear Instruments and Methods in Physics Research Section B: Beam Interactions with Materials and Atoms*, **266**, 4794 (2008). doi:10.1016/j.nimb.2008.07.022.
- [103] M. Vilén, L. Canete, B. Cheal et al. *Nuclear Instruments and Methods in Physics Research Section B: Beam Interactions with Materials and Atoms*, **463**, 382 (2020). doi:10.1016/j.nimb.2019.04.051.
- [104] A. Giatzoglou, T. Poomaradee, I. Pohjalainen et al. *Nuclear Instruments and Methods in Physics Research Section A: Accelerators, Spectrometers, Detectors and Associated Equipment*, **908**, 367 (2018). doi:10.1016/j.nima.2018.08.095.
- [105] A. Nieminen, J. Huikari, A. Jokinen et al. *Nuclear Instruments and Methods in Physics Research Section A: Accelerators, Spectrometers, Detectors and Associated Equipment*, **469**, 244 (2001). doi:10.1016/S0168-9002(00)00750-6.
- [106] T. Eronen, V. S. Kolhinen, V. V. Elomaa et al. *The European Physical Journal A*, **48**, 46 (2012). doi:10.1140/epja/i2012-12046-1.
- [107] R. P. de Groote, A. de Roubin, P. Campbell et al. *Nucl. Instrum. Methods Phys. Res. B*, **463**, 437 (2020). doi:10.1016/j.nimb.2019.04.028.
- [108] J. Ketelaer, J. Krämer, D. Beck et al. *Nuclear Instruments and Methods in Physics Research Section A: Accelerators, Spectrometers, Detectors and Associated Equipment*, **594**, 162 (2008). doi:10.1016/j.nima.2008.06.023.
- [109] B. Cheal and D. H. Forest. *Hyperfine Interactions*, **223**, 63 (2014). doi:10.1007/s10751-012-0608-5.
- [110] L. J. Vormawah, M. Vilén, R. Beerwerth et al. *Phys. Rev. A*, **97**, 042504 (2018). doi:10.1103/PhysRevA.97.042504.
- [111] Sirah. *Datasheet Matisse 2 TS* (2017). <http://www.sirah.com/wp-content/uploads/pdfs/Matisse-2-TS.pdf>.
- [112] K. König, P. Imgram, J. Krämer et al. *Applied Physics B*, **126** (2020). doi:10.1007/s00340-020-07433-4.
- [113] W. Gins, R. P. de Groote, M. L. Bissell et al. *Comput. Phys. Commun.*, **222**, 286 (2018). doi:10.1016/j.cpc.2017.09.012.

- [114] B. Cheal, M. D. Gardner, M. Avgoulea et al. *Physics Letters B*, **645**, 133 (2007). [doi:10.1016/j.physletb.2006.12.053](https://doi.org/10.1016/j.physletb.2006.12.053).
- [115] J. Eberz, U. Dinger, G. Huber et al. *Zeitschrift für Physik A Atomic Nuclei*, **326**, 121 (1987). [doi:10.1007/BF01283586](https://doi.org/10.1007/BF01283586).
- [116] C. Gorges, L. V. Rodríguez, D. L. Balabanski et al. *Phys. Rev. Lett.*, **122**, 192502 (2019). [doi:10.1103/PhysRevLett.122.192502](https://doi.org/10.1103/PhysRevLett.122.192502).
- [117] J. Eberz, U. Dinger, G. Huber et al. *Nuclear Physics A*, **464**, 9 (1987). [doi:10.1016/0375-9474\(87\)90419-2](https://doi.org/10.1016/0375-9474(87)90419-2).
- [118] F. Buchinger, P. Dabkiewicz, H.-J. Kluge, A. C. Mueller and E.-W. Otten. *Nuclear Physics A*, **462**, 305 (1987). [doi:10.1016/0375-9474\(87\)90550-1](https://doi.org/10.1016/0375-9474(87)90550-1).
- [119] M. Hammen, W. Nörtershäuser, D. L. Balabanski et al. *Phys. Rev. Lett.*, **121**, 102501 (2018). [doi:10.1103/PhysRevLett.121.102501](https://doi.org/10.1103/PhysRevLett.121.102501).
- [120] R. Ferrer, N. Bree, T. E. Cocolios et al. *Physics Letters B*, **728**, 191 (2014). [doi:10.1016/j.physletb.2013.11.055](https://doi.org/10.1016/j.physletb.2013.11.055).
- [121] I. Talmi. *Nuclear Physics A*, **423**, 189 (1984). [doi:10.1016/0375-9474\(84\)90587-6](https://doi.org/10.1016/0375-9474(84)90587-6).
- [122] T. Kutsarova, A. Minkova, M.-G. Porquet et al. *Phys. Rev. C*, **58**, 1966 (1998). [doi:10.1103/PhysRevC.58.1966](https://doi.org/10.1103/PhysRevC.58.1966).
- [123] X. Q. Zhang, J. H. Hamilton, A. V. Ramayya et al. *Phys. Rev. C*, **61**, 014305 (1999). [doi:10.1103/PhysRevC.61.014305](https://doi.org/10.1103/PhysRevC.61.014305).
- [124] J. Kurpeta, W. Urban, A. Płochocki et al. *Phys. Rev. C*, **90**, 064315 (2014). [doi:10.1103/PhysRevC.90.064315](https://doi.org/10.1103/PhysRevC.90.064315).
- [125] D. Fong, J. K. Hwang, A. V. Ramayya et al. *Phys. Rev. C*, **72**, 014315 (2005). [doi:10.1103/PhysRevC.72.014315](https://doi.org/10.1103/PhysRevC.72.014315).
- [126] M. Houry, R. Lucas, M.-G. Porquet et al. *The European Physical Journal A-Hadrons and Nuclei*, **6**, 43 (1999). [doi:10.1007/s100500050315](https://doi.org/10.1007/s100500050315).
- [127] R. Aryaeinejad, J. D. Cole, R. C. Greenwood et al. *Phys. Rev. C*, **48**, 566 (1993). [doi:10.1103/PhysRevC.48.566](https://doi.org/10.1103/PhysRevC.48.566).
- [128] H. Hua, C. Y. Wu, D. Cline et al. *Physics Letters B*, **562**, 201 (2003). [doi:10.1016/S0370-2693\(03\)00569-0](https://doi.org/10.1016/S0370-2693(03)00569-0).
- [129] Y. X. Luo, J. O. Rasmussen, J. H. Hamilton et al. *Nuclear Physics A*, **919**, 67 (2013). [doi:10.1016/j.nuclphysa.2013.10.002](https://doi.org/10.1016/j.nuclphysa.2013.10.002).
- [130] X. Q. Zhang, J. H. Hamilton, A. V. Ramayya et al. *Phys. Rev. C*, **63**, 027302 (2001). [doi:10.1103/PhysRevC.63.027302](https://doi.org/10.1103/PhysRevC.63.027302).

- [131] H. Penttilä, T. Enqvist, P. P. Jauho et al. *Nuclear Physics A*, **561**, 416 (1993). [doi:10.1016/0375-9474\(93\)90019-T](https://doi.org/10.1016/0375-9474(93)90019-T).
- [132] J. Kurpeta, W. Urban, A. Płochocki et al. *Phys. Rev. C*, **82**, 027306 (2010). [doi:10.1103/PhysRevC.82.027306](https://doi.org/10.1103/PhysRevC.82.027306).
- [133] J. Äystö, C. N. Davids, J. Hattula et al. *Nuclear Physics A*, **480**, 104 (1988). [doi:10.1016/0375-9474\(88\)90387-9](https://doi.org/10.1016/0375-9474(88)90387-9).
- [134] J. Kurpeta, A. Płochocki, W. Urban et al. *Phys. Rev. C*, **98**, 024318 (2018). [doi:10.1103/PhysRevC.98.024318](https://doi.org/10.1103/PhysRevC.98.024318).
- [135] H. Penttilä, J. Äystö, K. Eskola et al. *Zeitschrift für Physik A Hadrons and Nuclei*, **338**, 291 (1991). [doi:10.1007/BF01288192](https://doi.org/10.1007/BF01288192).
- [136] Y. B. Wang and J. Rissanen. *Hyperfine Interactions*, **223**, 167 (2014). [doi:10.1007/s10751-012-0615-6](https://doi.org/10.1007/s10751-012-0615-6).
- [137] P. Sarriguren. *Phys. Rev. C*, **91**, 044304 (2015). [doi:10.1103/PhysRevC.91.044304](https://doi.org/10.1103/PhysRevC.91.044304).
- [138] F. R. Xu, P. M. Walker and R. Wyss. *Phys. Rev. C*, **65**, 021303 (2002). [doi:10.1103/PhysRevC.65.021303](https://doi.org/10.1103/PhysRevC.65.021303).
- [139] W. Urban, T. Rzaca-Urban, J. L. Durell et al. *The European Physical Journal A-Hadrons and Nuclei*, **20**, 381 (2004). [doi:10.1140/epja/i2004-10023-y](https://doi.org/10.1140/epja/i2004-10023-y).
- [140] W. Urban, T. Rzaca-Urban, J. L. Durell, A. G. Smith and I. Ahmad. *The European Physical Journal A-Hadrons and Nuclei*, **24**, 161 (2005). [doi:10.1140/epja/i2004-10140-7](https://doi.org/10.1140/epja/i2004-10140-7).
- [141] J. Kurpeta, W. Urban, A. Płochocki et al. *Phys. Rev. C*, **84**, 044304 (2011). [doi:10.1103/PhysRevC.84.044304](https://doi.org/10.1103/PhysRevC.84.044304).
- [142] H. Watanabe, G. Lorusso, S. Nishimura et al. *Phys. Rev. Lett.*, **111**, 152501 (2013). [doi:10.1103/PhysRevLett.111.152501](https://doi.org/10.1103/PhysRevLett.111.152501).
- [143] A. Jungclaus, L. Cáceres, M. Górska et al. *Phys. Rev. Lett.*, **99**, 132501 (2007). [doi:10.1103/PhysRevLett.99.132501](https://doi.org/10.1103/PhysRevLett.99.132501).
- [144] J. Blachot. *Nuclear Data Sheets*, **111**, 1471 (2010). [doi:10.1016/j.nds.2010.05.001](https://doi.org/10.1016/j.nds.2010.05.001).
- [145] J. Blachot. *Nuclear Data Sheets*, **113**, 2391 (2012). [doi:10.1016/j.nds.2012.10.002](https://doi.org/10.1016/j.nds.2012.10.002).
- [146] R. P. de Groote, J. Billowes, C. L. Binnersley et al. *Nature Physics* (2020). [doi:10.1038/s41567-020-0868-y](https://doi.org/10.1038/s41567-020-0868-y).

- [147] R. F. G. Ruiz, M. L. Bissell, K. Blaum et al. *Nature Physics*, **12**, 594 (2016). [doi:10.1038/nphys3645](https://doi.org/10.1038/nphys3645).
- [148] A. R. Vernon, J. Billowes, C. L. Binnersley et al. *Spectrochim. Acta B*, **153**, 61 (2019). [doi:10.1016/j.sab.2019.02.001](https://doi.org/10.1016/j.sab.2019.02.001).
- [149] R. Engleman, U. Litzén, H. Lundberg and J.-F. Wyart. *Phys. Scr.*, **57**, 345 (1998). [doi:10.1088/0031-8949/57/3/006](https://doi.org/10.1088/0031-8949/57/3/006).
- [150] D. Gorelov. *Nuclear fission studies with the IGISOL method and JYFLTRAP*. Ph.D. thesis, University of Jyväskylä (2015).
- [151] A. Klose, K. Minamisono, C. Geppert et al. *Nuclear Instruments and Methods in Physics Research Section A: Accelerators, Spectrometers, Detectors and Associated Equipment*, **678**, 114 (2012). [doi:10.1016/j.nima.2012.03.006](https://doi.org/10.1016/j.nima.2012.03.006).
- [152] A. C. Mueller, F. Buchinger, W. Klempt et al. *Nuclear Physics A*, **403**, 234 (1983). [doi:10.1016/0375-9474\(83\)90226-9](https://doi.org/10.1016/0375-9474(83)90226-9).
- [153] A. Voss, V. Sonnenschein, P. Campbell et al. *Phys. Rev. A*, **95**, 032506 (2017). [doi:10.1103/PhysRevA.95.032506](https://doi.org/10.1103/PhysRevA.95.032506).
- [154] F. C. Charlwood, K. Baczynska, J. Billowes et al. *Physics Letters B*, **674**, 23 (2009). [doi:10.1016/j.physletb.2009.02.050](https://doi.org/10.1016/j.physletb.2009.02.050).
- [155] P. Campbell, H. L. Thayer, J. Billowes et al. *Phys. Rev. Lett.*, **89**, 082501 (2002). [doi:10.1103/PhysRevLett.89.082501](https://doi.org/10.1103/PhysRevLett.89.082501).
- [156] A. Dewald, K. Starosta, P. Petkov et al. *Phys. Rev. C*, **78**, 051302 (2008). [doi:10.1103/PhysRevC.78.051302](https://doi.org/10.1103/PhysRevC.78.051302).
- [157] E. R. Gamba, A. M. Bruce, S. Lalkovski et al. *Phys. Rev. C*, **100**, 044309 (2019). [doi:10.1103/PhysRevC.100.044309](https://doi.org/10.1103/PhysRevC.100.044309).
- [158] J. Erler, N. Birge, M. Kortelainen et al. *Nature*, **486**, 509 (2012). [doi:10.1038/nature11188](https://doi.org/10.1038/nature11188).
- [159] M. V. Stoitsov, N. Schunck, M. Kortelainen et al. *Computer Physics Communications*, **184**, 1592 (2013). [doi:10.1016/j.cpc.2013.01.013](https://doi.org/10.1016/j.cpc.2013.01.013).
- [160] P.-G. Reinhard, W. Nazarewicz and R. F. Garcia Ruiz. *Phys. Rev. C*, **101**, 021301 (2020). [doi:10.1103/PhysRevC.101.021301](https://doi.org/10.1103/PhysRevC.101.021301).
- [161] M. Reponen, I. D. Moore, I. Pohjalainen et al. *Review of Scientific Instruments*, **86**, 123501 (2015). [doi:10.1063/1.4936569](https://doi.org/10.1063/1.4936569).
- [162] D. A. Nesterenko, T. Eronen, A. Kankainen et al. *The European Physical Journal A*, **54**, 154 (2018). [doi:10.1140/epja/i2018-12589-y](https://doi.org/10.1140/epja/i2018-12589-y).

- [163] *JYFL Accelerator News*. September, 2018. URL https://www.jyu.fi/science/en/physics/current/jyfl-accelerator-news/newsletter2_2018.pdf.
- [164] *JYFL Accelerator News*. September, 2019. URL https://www.jyu.fi/science/en/physics/current/jyfl-accelerator-news/newsletter2_2019.pdf.
- [165] W. Gins, R. D. Harding, M. Baranowski et al. *Nuclear Instruments and Methods in Physics Research Section A: Accelerators, Spectrometers, Detectors and Associated Equipment*, **925**, 24 (2019). doi:10.1016/j.nima.2019.01.082.



ORIGINAL PAPERS

I

DEVELOPMENT OF A SATURATED ABSORPTION SPECTROSCOPY SETUP AT IGISOL FOR CHARACTERISATION OF FABRY-PÉROT INTERFEROMETERS

by

S. Geldhof, S. El Youbi, I. D. Moore, I. Pohjalainen, V. Sonnenschein, R.
Terabayashi, A. Voss

Hyperfine Interactions 238: 7 (2017)

Reproduced with kind permission of Springer Nature.

<https://doi.org/10.1007/s10751-016-1385-3>

Development of a saturated absorption spectroscopy setup at IGISOL for characterisation of Fabry-Pérot interferometers

S. Geldhof · S. El Youbi · I. D. Moore ·
I. Pohjalainen · V. Sonnenschein · R. Terabayashi ·
A. Voss

Received: date / Accepted: date

Abstract A saturated absorption spectroscopy setup was developed and optimised for the characterisation of a home-built and a commercial Fabry-Pérot interferometer (FPI). The free spectral range of these FPIs has been determined with reliable statistical and systematic errors. These FPIs will be used for accurate wavelength determination of broad- and narrowband pulsed Ti:Sapphire lasers used in resonance ionisation spectroscopy experiments.

Keywords Fabry-Pérot interferometer · saturation spectroscopy · rubidium

1 Introduction

Laser resonance ionisation offers outstanding opportunities to combine selectivity and sensitivity with an on-line ion source for means of element-selective ionisation of short-lived exotic nuclei or for the study of part-per-million perturbations in the atomic levels through measurements of hyperfine structure and isotope shifts [1]. This method of spectroscopy is commonly referred to as *in-source* resonance ionisation spectroscopy (RIS) and has been demonstrated both in hot cavity ion sources as well as buffer gas cells. Despite the impressive sensitivity to nuclei produced far from stability, it often remains a challenge to analyse the lower resolution in-source spectra (a reduction in spectral resolution due to environmental effects as well as the pulsed laser linewidth) and to reliably assign systematic uncertainties. In these experiments it is not possible to keep the laser frequency fixed and use a doppler tuning voltage for scanning, as in high-resolution collinear laser spectroscopy, thus the laser frequency itself must be scanned. This necessitates accurate wavelength determination. At the IGISOL facility, Jyväskylä, the wavelength of the pulsed Ti:sapphire laser radiation has been traditionally measured using a HighFinesse WS/6-UV wavemeter with an absolute accuracy of 600 MHz. Although this resolution is satisfactory for laser resonance ionisation, it was found to be unsuitable when used for spectroscopy through a measurement

S. Geldhof · S. El Youbi · I. D. Moore · I. Pohjalainen · A. Voss
Department of Physics, University of Jyväskylä, Surfontie 9, PB 35 (YFL), 40014 Jyväskylä, Finland.
E-mail: sarina.m.geldhof@ju.fi

V. Sonnenschein · R. Terabayashi
Department of Quantum Engineering, Nagoya University, Furo-cho, Chikusa-ku, Nagoya 464-8603, Japan.

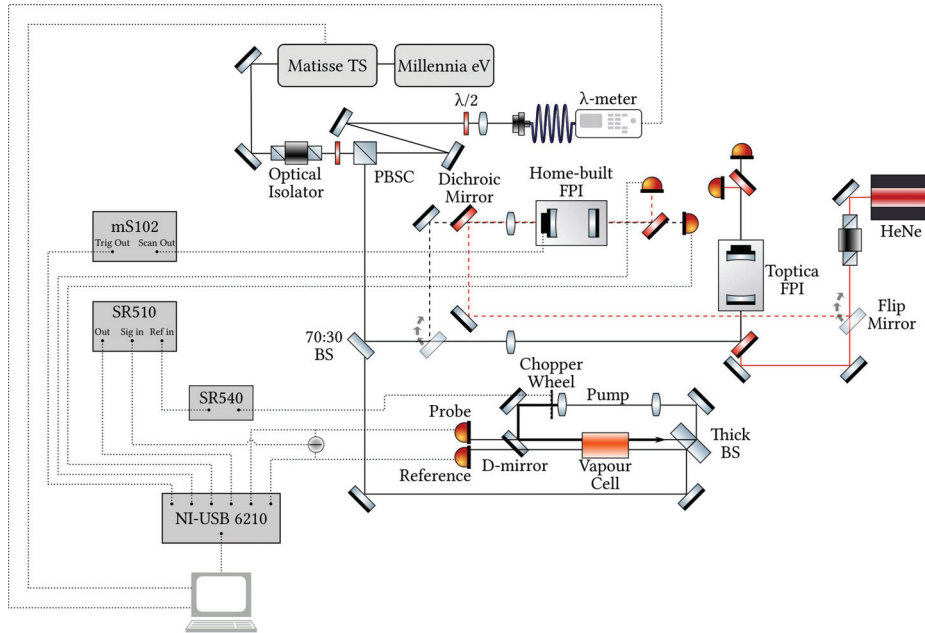


Fig. 1: Schematic of the cw laser system, the saturation absorption spectroscopy setup and two Fabry-Pérot interferometers. The ramp generator (Miniscan 102) and photodiodes can be connected to either FPI unit as required. The relevant data acquisition system is also highlighted. Colour on-line.

of the hyperfine parameters of ^{63}Cu which revealed discrepancies to existing high-resolution literature data [2].

A more appropriate method of frequency determination is with a scanning Fabry-Pérot interferometer (FPI). At IGISOL, pulsed Ti:Sapphire lasers with a broad range of bandwidths are in use. The standard resonator configuration is based on the Z-shaped standing wave design with a bandwidth of typically 5 GHz, currently in use at many RIB facilities for in-source resonance laser ionisation [3], a dual-etalon Ti:Sapphire laser for in-gas-cell spectroscopy with a bandwidth reduced to <1 GHz [2] and an injection-locked Ti:Sapphire laser with a narrow bandwidth of ~ 20 MHz [4,5], motivated for the exploitation of in-gas-jet spectroscopy. These various bandwidths require FPIs with different free spectral ranges (FSRs) in order to calculate the frequency changes in a suitable mode of resolution. To measure frequency changes during scanning the interferometers must first be calibrated, in other words the FSR needs to be determined as precisely as possible. The method described in this work is via a calibration against an atomic transition exhibiting a well-known hyperfine structure. For this purpose we have developed a Doppler-free saturated absorption spectroscopy setup which uses either a Rb or Cs vapour cell, installed in a newly constructed continuous wave (cw) Ti:Sapphire laser laboratory.

2 Experimental setup and data acquisition

A schematic of the saturated absorption spectroscopy setup is given in Fig. 1. The cw Ti:Sapphire laser beam (Sirah Matisse TS), pumped by a 6W Millennia eV DPSS laser, is split up in two beams by a polarising beam splitter cube (PBSC) and a half-waveplate. One of the beams is fibre coupled to the HighFinesse WS/6-UV wavemeter, the other is reflected to the experimental setup. A 70:30 beam splitter sends 70% of this beam to be used for spectroscopy with the remaining 30% delivered to the FPIs.

As can be seen in Fig. 1, in order to perform saturated absorption spectroscopy a part of the laser beam is split in two by reflecting it on the front and back surface of an uncoated thick (12 mm) glass beam splitter. The beam from the front reflection is termed the reference beam and the back reflection the probe beam. Both beams have a diameter of approximately 1 mm and pass through a vapour cell containing either natural rubidium (72.168% ^{85}Rb and 27.835% ^{87}Rb) or caesium (^{133}Cs). Individual photodiodes (Thorlabs, FDS100) are used to record the probe and reference beam, the signals then being fed into the data acquisition. The difference between the probe and reference signals is generated electronically and used as an input for the lock-in amplifier (Stanford Research Systems, SR510). The majority of the laser light, however, is transmitted by the thick beam splitter and becomes the pump beam, after expansion to a larger diameter of about 3 mm using a telescope. Before being overlapped in a counter-propagating direction with the probe beam by reflection from a D-shaped mirror, the pump beam is modulated using a chopper wheel. This wheel can be operated at different frequencies set by the chopper controller (Stanford Research Systems, SR540) and is needed in conjunction with the lock-in amplifier.

In addition to the saturated absorption spectroscopy setup, 30% of the Ti:Sapphire beam is sent to one of two scanning FPIs together with a frequency-stabilised HeNe laser (Melles Griot, 25-STP-912-230), stable to within a MHz per hour and 10 MHz per month according to specifications [6]. One FPI is home-built and uses a semi-hemispherical geometry, with a planar and a concave mirror (7.5 cm radius of curvature) having a broadband coating (97% reflectivity for 630-1050 nm) [7]. Due to the non-confocal nature of the FPI the laser beams must be mode-matched to the cavity in order to suppress higher order Hermite-Gaussian modes. The incoming laser beams may also have different waist sizes which will affect the mode-matching, and thus both beams pass through an aperture of approximately 1 mm in diameter before being focused into the FPI. Currently the finesse is limited to a value of ~ 75 , however values of close to 1500 were reached when using a pair of high reflecting mirrors of $R=99.8\%$, at the expense of greatly reduced transmission. The second FPI is a confocal commercial Toptica FPI-100-0750-y with an FSR of 1 GHz and a Finesse of 200-500 with the mirror set coated for 615-885 nm [8]. For both FPIs, scanning of one mirror by a piezo is provided by a ramp generator (Toptica, Miniscan 102). The Ti:Sapphire and HeNe beams are combined and split up again after the FPI with dichroic mirrors (Thorlabs, M254C45) and are detected on photodetectors with variable amplification (Thorlabs, PDA36A-EC). Fast switching between the FPIs is provided by flip mirrors.

The data acquisition hardware module from National Instruments (NI USB-6210) has 16 analogue voltage input channels with a sampling rate of 250kS/s shared between all channels in use [9]. In this work, six signals are connected: the photodiode signals from both probe and reference beam, the FPI photodiode signals of the HeNe and the Ti:Sapphire, the lock-in amplifier output and the trigger signal of the ramp generator. Acquisition and on-line visualisation is controlled in LabVIEWTM. The DAQ sampling rate puts a maximum limit on the piezo scan speed of the high finesse FPI cavities, as proper peak detection is needed.

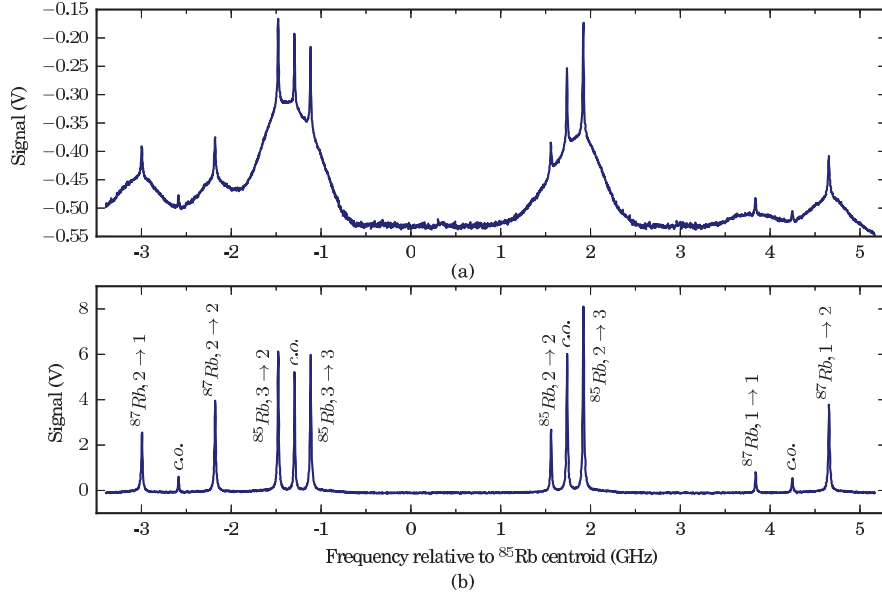


Fig. 2: (a) The direct difference between probe and reference on the Rb D1 transition. (b) The spectrum after the lock-in amplifier. The residual Doppler-broadened background is removed, the noise is reduced and the resonances are amplified. Labels indicate the transitions, with c.o. used for the cross-over resonances.

Since the raw data of all signals would quickly reach an inconvenient file size, real-time analysis is used for data reduction. A time average over one FPI scan is taken for the probe and reference signals. A linear fit of the data over this period of one FPI scan is performed to calculate the error using the fit residuals. Only the average of each signal and the standard deviation of the fit residuals are saved. By utilising a peak detection routine in LabVIEWTM, only the location and amplitude of the transmission fringes are recorded. The acquisition and analysis loops are separated in order to operate simultaneously with optimal performance. The peak detection is performed using the default peak detect function in LabVIEWTM, *Peak detector VI* [10]. It is based on an algorithm that fits a quadratic polynomial to consecutive groups of data points specified by an adjustable interval.

3 Optimisation of saturated absorption setup

According to saturated absorption theory [11], it is possible to obtain a Doppler-free spectrum with a flat background and a spectral linewidth only limited by the natural linewidth of the atomic transition by subtracting the reference signal from the probe signal, as all fluctuations should be identical for the two beams. In the normal experimental setup without a lock-in amplifier a background noise signal was always seen. This was due to imbalances in the photodiodes and their amplifiers, and absorption differences in the probe and reference beam. The reflections of the thick beam splitter are not equal in power, so slight steering and power changes while scanning the Ti:sapphire laser frequency affect both photodiode

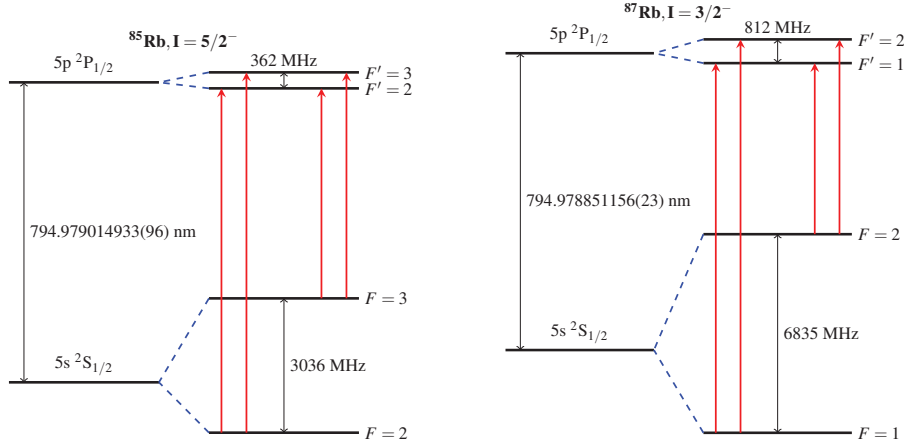


Fig. 3: D1 transition in rubidium with wavelength in vacuum and hyperfine splittings in MHz. Allowed transitions are indicated by arrows. The HFS splittings were calculated using the standard HFS equation [12] using HFS parameters from [13, 14].

signals differently. This can give rise to a non-constant background and residual Doppler broadening in the difference signal. An example can be seen in Fig. 2a for a spectrum on the Rb D1 transition, the details of which are presented in Fig. 3. So-called "cross-over" (c.o.) resonances are inherent to the saturated absorption spectroscopy technique when multiple hyperfine transitions are located within one Doppler broadened feature. They occur when pump and probe beam are resonant with different hyperfine transitions of the same multiplet. Fig. 2 shows four c.o. resonances in addition to the six hyperfine resonances.

To solve the problem of the residual background contributions, a lock-in amplifier was installed as shown in Fig. 1 using the direct difference between probe and reference beam as input. The waveform from the chopper controller, a square wave, is used as the reference signal for the lock-in amplifier. This eliminates the background as only signals correlated with the pump beam are recorded, and amplifies the resonances. An example of the spectral enhancement can be seen in Fig. 2b. This experimental setup was tested to obtain the optimal conditions. As the input and reference signal are mixed in the lock-in amplifier, it can be shown with simple mathematics that the output is of the form $V_{out} = \frac{1}{2}V_{signal}V_{ref}\cos(\Delta\phi)$ where V_i are the amplitudes and $\Delta\phi$ the phase difference between the signal and reference. Therefore changing the phase angle between the input and reference signal on the lock-in amplifier should yield a cosine dependence on the peak intensities as is experimentally observed in Fig. 4. Notice that the results shown in Fig. 4 are for spectroscopy on Cs.

As considerable condensation was present at room temperature in the Rb vapour cell, a heating controller (Thorlabs TC200) was installed around the cell. The effect of heating was investigated by comparing the depth of the Doppler-broadened absorption (using the single reference beam) and the saturated absorption peak intensity for different temperatures, as shown in Fig. 5. Cs on the other hand showed a very strong absorption, even at room temperatures, therefore the heater is not required in this case.

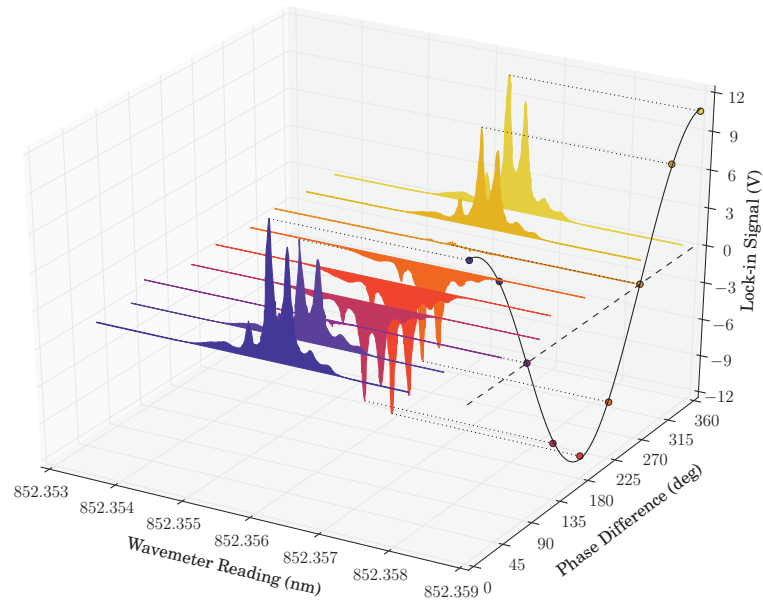


Fig. 4: Partial hyperfine spectra taken on the Cs D2 transition by changing the phase angle between input and reference signal in the lock-in amplifier. The peak intensities show a cosine dependence as expected from theory. Colour on-line.

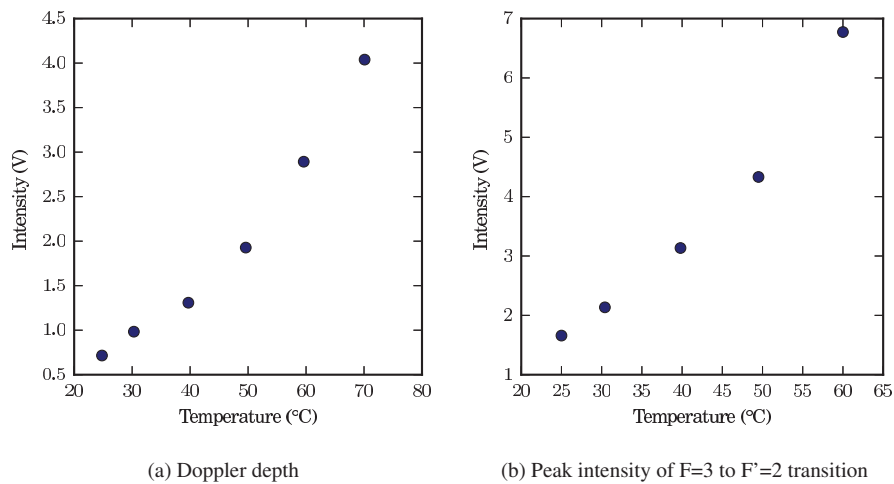


Fig. 5: Effect of heating the Rb vapour cell on the (a) Doppler-broadened absorption depth and (b) saturated absorption peak intensity of the F=3 to F'=2 transition in the D1 transition of ^{85}Rb . Error bars are within data points.

4 Fabry-Pérot interferometer characterisation

4.1 Procedure

In order to characterise the FSR of the FPIs, the saturated absorption spectrum of the D1 transition in Rb was recorded, simultaneously with the transmission fringes of both the stabilised HeNe laser and the scanning cw Ti:sapphire laser.

The initial step in the characterisation procedure is to convert the recorded time scale to a scale in *number of FSR*. The data is first split up into separate FPI scans using the ramp trigger signal as an indicator of the start and stop of each scan. Both the HeNe and Ti:Sapphire transmission fringe positions in a scan are then identified. Ideally, the distance between consecutive fringes should be constant, however this is not the case due to the non-linearity of the piezo scanning of the FPI mirror. Therefore, the fringe positions are linearised. The positions of the HeNe fringes, with the first fringe set to zero for reference, are plotted versus the number of fringes counted, which is equal to the number of scanned FSRs. The data points are then fitted with polynomials of different orders. An example of one such fit can be seen in Fig. 6. While the deviation between a linear fit and the data points is of the order of 5% of one FSR, the third degree polynomial reproduces the data accurate to 0.4%. Higher order polynomials did not significantly improve the fit. The positions of the Ti:Sapphire fringes are then converted to the number of FSRs scanned, using the fit parameters obtained from the HeNe transmission fringes and scaling by the ratio of the wavelengths, $\lambda_{\text{HeNe}}/\lambda_{\text{Ti:Sa}} = 632.099 \text{ nm}/794.979 \text{ nm}$.

Secondly, one Ti:Sapphire fringe and the corresponding HeNe fringe are chosen, to track and use for the determination of the *number of FSR* scale. While temperature changes and vibrations will cause drifting of the transmission fringes, both the HeNe and Ti:Sapphire are affected in the same manner. The position difference between the Ti:Sapphire and HeNe fringes is thus unaffected. As the tuning range of the Ti:Sapphire laser often spans multiple FSRs to cover the whole hyperfine structure, the tracked Ti:Sapphire fringe would at some point leave the available scanning range provided by the piezo. To overcome this problem, the transmission order of the tracked Ti:Sapphire fringe is changed by one in the analysis procedure each time the currently tracked fringe moves too far from the HeNe fringe, i.e. by more than half an FSR (Fig. 7). The scanned number of FSRs is then the value obtained from the linearisation fit procedure for the tracked Ti:Sapphire fringe plus the number of jumps, N_j , up to that point in the Ti:Sapphire scan,

$$FSR = FSR_{fit} + N_j. \quad (1)$$

To improve the statistical uncertainty, multiple Ti:Sapphire fringes may be tracked in the same way to calculate an average for FSR_{fit} . The number of Ti:Sapphire fringes one can choose to track depends on the number of recorded Ti:Sapphire fringes per scan, the non-linearity and the temperature stability. Usually the piezo movement is highly non-linear at the start and end of a scan, so it is best not to use the Ti:Sapphire fringes close to a change in scan direction. Temperature fluctuations will move the HeNe fringes, so some transmission orders might (dis)appear from the FPI scanning range. As the same HeNe transmission orders are tracked over the whole spectrum, only orders that are present throughout the entire hyperfine structure scan can be used. Based on these considerations, an optimal number of Ti:Sapphire fringes can be chosen for each spectrum.

The difference between the number of FSRs obtained for each Ti:Sapphire fringe from the fit, after rescaling by the wavelength ratio, should be equal to one, as one FSR is de-

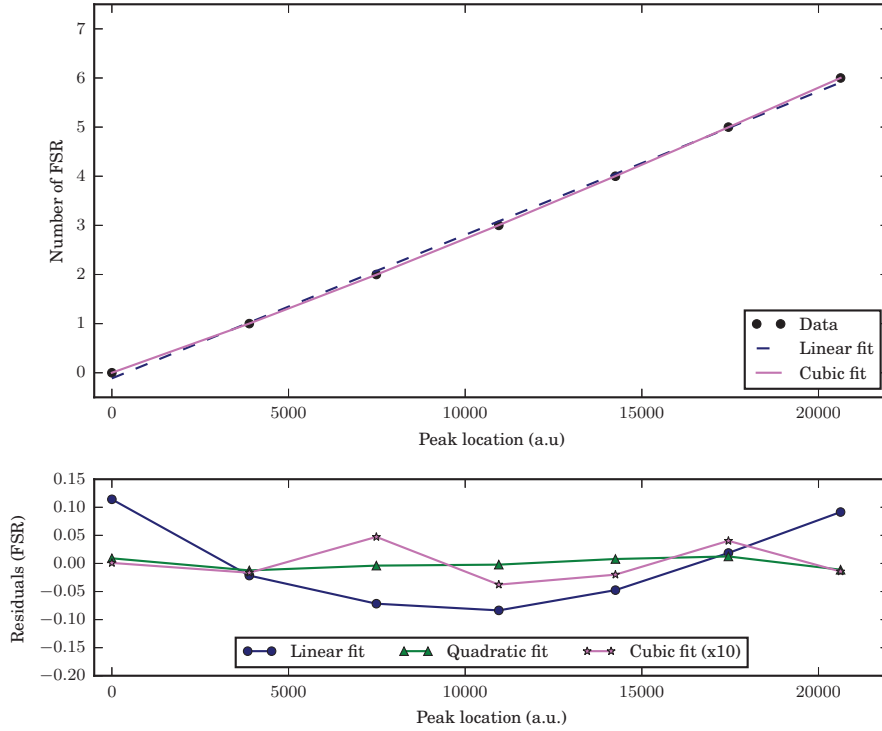


Fig. 6: An example of the linearisation of the relative HeNe fringe positions against FSR number. In the upper plot the quadratic fit is not shown for clarity. The lower plot shows the residuals for the different polynomials with the residuals of the cubic fit multiplied by ten. Colour on-line.

defined as the spacing between two fringes. The deviation from one gives the remaining non-linearity that is not compensated. For each FPI scan the average of the differences from one is calculated, and then finally, the average of all values for one spectrum is determined. This value is added as a systematic error to the measured value of the FSR.

Combining the number of FSRs scanned with the recorded photodiode signals, a spectrum can be plotted with one data point for each FPI scan. The value of the FSR, in frequency units, is then obtained from a hyperfine structure fit with the all hyperfine parameters fixed to literature values but multiplied by a free-running common scaling factor. The inverse of this scaling factor is an accurate measure of the FSR.

4.2 Results

In total 14 spectra were recorded on the D1 transition in Rb, two for the home-built FPI and eight for the Toptica FPI without lock-in amplifier, and two scans for each FPI with the lock-in amplifier. Each spectrum was converted to an x -axis in *number of FSR* using the procedure outlined in section 4.1, each time using the optimal number of Ti:Sapphire fringes.

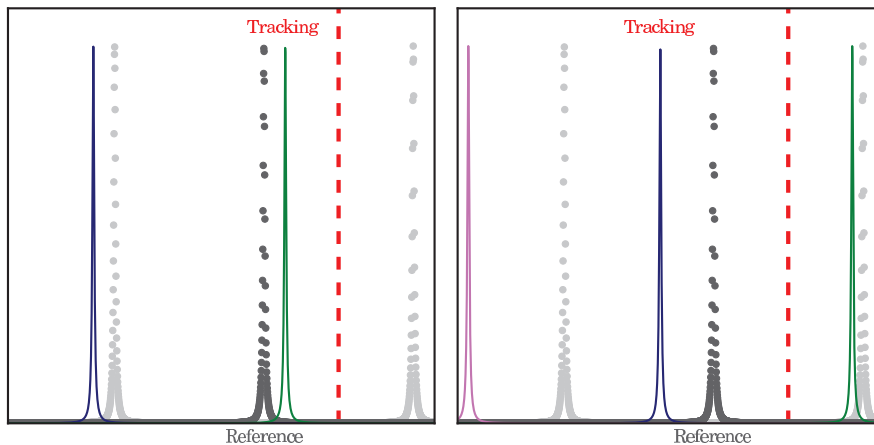


Fig. 7: Illustration of the fringe tracking procedure. Dotted lines are HeNe fringes, solid lines are Ti:Sapphire fringes. The darker HeNe fringe is the reference (labeled below). The left figure represents the first FPI scan. In the figure to the right, recorded some time later, the previously tracked fringe has moved beyond the limit of half an FSR from the reference HeNe fringe, indicated by the dashed red line, and thus a jump back has occurred. Colour on-line.

Table 1: FSR values for the home-built and commercial Toptica FPI. The values per technique are weighted averages, and the final values are the weighted averages running over all individual values. Only statistical uncertainties are quoted.

	Without lock-in (GHz)	With lock-in (GHz)	Previous measurement (GHz) [5]	Final value (GHz)
Toptica FPI	0.99887(4)	0.998569(15)	0.99850(15)	0.998604(14)
Home-built FPI	3.4765(2)	3.46525(5)		3.46571(5)

Hyperfine structure fits were performed to the Rb spectra with Lorentzian lineshapes, a common full width at half maximum (FWHM) and the common scaling factor for the hyperfine parameters and isotope shift fixed to the literature values [13, 14]. All peak intensities were left free, as constraining them by the Racah coefficients had a negative effect due to the peak positions not being in the exact location given by the hyperfine parameters. The positions of the crossover peaks were determined using the hyperfine parameters, and thus are also scaled by the common factor.

The weighted averaged FSR values for each FPI, with and without the use of the lock-in amplifier, can be found in Table 1, including a previous value determined for the commercial Toptica FPI [5]. The values per technique are weighted averages, however the final weighted average per FPI runs over all individual values. The final adopted values for the FSRs of both FPIs are the weighted averages of the individual values. The systematic uncertainties, calculated from the remaining non-linearity as explained in section 4.1, are 4 MHz for the Toptica FPI and 5 MHz for the home-built FPI, respectively. Temperature drifts are the main cause of the systematic error, as the linearisation becomes less reliable when the HeNe fringes move considerably. The continuous wave laboratory was recently upgraded, with

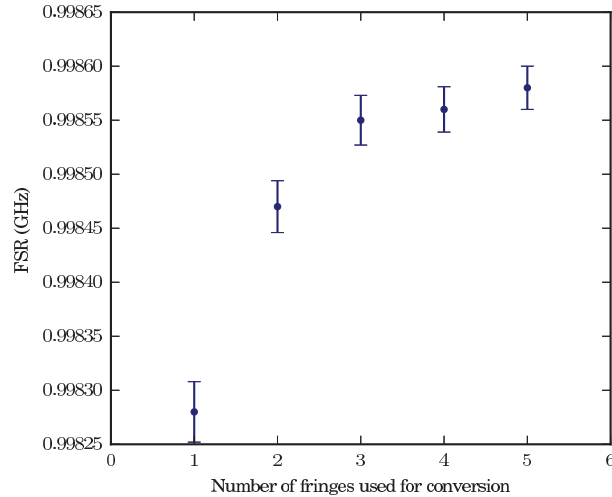


Fig. 8: Example of improvement of statistical errors (a small reduction in the size of the error bars) and convergence of the FSR value with increasing number of Ti:sapphire transmission fringes used for conversion for the Toptica FPI. Systematic errors are not included.

the optical table better shielded from the air flow from the air-conditioning unit. Very recent tests show that the systematic error for the Toptica FPI has been reduced to 3 MHz. This directly correlates to less drifting of the HeNe fringes in the new environment, as was seen when tracking the fringes over time.

To prove that using multiple Ti:Sapphire fringes for the conversion to scanned number of FSR improves the statistical uncertainty, the conversion for four spectra was done using one to five fringes out of a total of about six or seven fringes. Five fringes was the maximum possible due to temperature instabilities. For each number of used fringes the fit to determine the FSR was performed. In all spectra the reduced chi-squared improved with the number of fringes used. The statistical uncertainty on the FSR value also decreased and the value itself appears to saturate with increasing number of fringes, shown for one spectrum in Fig. 8.

As a consistency check, the four spectra taken with the lock-in amplifier were converted to an actual frequency scale. This is done by multiplying the scanned number of FSR from Eq. 1 by the obtained FSR in frequency units from Table 1. The fit to the hyperfine structure was then redone, however now using free-running hyperfine parameters and isotope shift, again with Lorentzian lineshapes, a common FWHM and free intensities. Typical differences of the hyperfine parameters with respect to literature values are of the order of 0.5 MHz for the Toptica and 0.8 MHz for the home-built FPI, as can be seen in Table 2, which is considerably smaller than the systematic errors of either 4 or 5 MHz. This gives confidence in the assignment of the systematic errors.

5 Conclusion

A saturated absorption spectroscopy setup for Rb and Cs has been implemented at the IGISOL facility and optimised using phase-sensitive detection via a lock-in amplifier. Us-

Table 2: Results of the fit with free-running hyperfine parameters and isotope shift as a consistency check. Only statistical errors are shown. None of the values deviates more than the systematic error which is dominated by temperature instabilities.

	Literature (MHz) [13, 14]	Toptica FPI (MHz)	Home-built FPI (MHz)
$A_{85,^2P_{1/2}}$	120.527(56)	121.34(3)	120.71(3)
$A_{85,^2S_{1/2}}$	1011.9108130(20)	1011.72(3)	1011.98(3)
$A_{87,^2P_{1/2}}$	407.25(63)	407.90(7)	408.54(6)
$A_{87,^2S_{1/2}}$	3417.341305452145(45)	3417.19(6)	3416.76(6)
ν_{87-85}	78.095(12)	78.29(7)	78.40(7)

ing the saturated absorption spectrum of the D1 transition in Rb as a calibration, a procedure for frequency conversion using FPIs has been developed and described in detail. The free spectral range of a commercial Toptica and a home-built FPI were determined to be 0.998836(13)[4000] GHz and 3.46571(5)[500] GHz, respectively. The technique has resulted in a good understanding of statistical and systematic errors.

The rather large size of the systematic uncertainties (of the order of a few MHz) is most likely due to temperature instabilities within the laser laboratory. Work on the general lab environment has been undertaken to reduce the uncertainties further and investigations to quantify the instabilities are currently of high priority. In order to mitigate any temperature drifts in the future, one route to be pursued will be to temperature stabilise the FPIs well above room temperature in order to be independent from the general laboratory environment.

Improvements are also underway for the data acquisition. It has been observed that small fluctuations in the FPI photodiode signals may cause errors such as duplicate detection in the peak detector routine. As the transmission fringes can be expressed as series of Lorentzian functions [15], a new method based on Lorentzian fitting is expected to yield a more reliable and accurate result. It is further anticipated to interface the DAQ system with the scanning of the laser through the Matisse Commander such that individual frequency steps can be taken.

In the future, the cw Ti:sapphire laser will be used for high-resolution collinear laser spectroscopy experiments and thus will require long-term frequency stabilisation. Typical stabilisation methods include the use of a suitable commercial wavelength meter [16] or by transferring the stability of a master laser via an FPI of low FSR [17]. Often, a frequency stabilised HeNe laser acts as the master laser achieving a long-term frequency stability of ~ 400 kHz relative to the HeNe [18]. It is foreseen to investigate the frequency stability of the HeNe laser used in the experiments presented here by stabilising the Matisse TS against a saturated absorption peak and tracking the transmission fringes of both lasers via a 150 MHz FPI. In parallel, tendering for a new commercial wavemeter has begun. The best method of frequency stabilising the cw Ti:Sapphire laser will then be evaluated.

Acknowledgements This work has been supported by the Academy of Finland programme under the Finnish Centre of Excellence Programme 2012-2017 (Project No. 251353, Nuclear and Accelerator-Based Physics Research at JYFL).

References

1. Fedosseev, V.N., Kudryavtsev, Y., Mishin, V.I.: Resonance laser ionization of atoms for nuclear physics. *Physica Scripta* **85**(5), 058,104 (2012)
2. Sonnenschein, V., Moore, I., Khan, H., Pohjalainen, I., Reponen, M.: Characterization of a dual-etalon Ti:Sapphire laser via resonance ionization spectroscopy of stable copper isotopes. *Hyp. Int.* **227**(1-3), 113–123 (2014)
3. Geppert, C.: Laser systems for on-line laser ion sources. *Nucl. Instrum. Meth. B* **266**(19–20), 4354 – 4361 (2008). Proceedings of the XVth International Conference on Electromagnetic Isotope Separators and Techniques Related to their Applications
4. Kessler, T., Tomita, H., Mattolat, C., Raeder, S., Wendt, K.: An injection-seeded high-repetition rate Ti:Sapphire laser for high-resolution spectroscopy and trace analysis of rare isotopes. *Laser Phys.* **18**(7), 1–8 (2008)
5. Sonnenschein, V.: Laser developments and high resolution resonance ionization spectroscopy of actinide elements. Ph.D. thesis, University of Jyväskylä (2014)
6. Melles Griot: Specifications stabilized helium neon laser system 05-STP-912
7. Khan, H.: Fabry-Perot interferometer; construction, calibration and development. Master's thesis, University of Jyväskylä (2015)
8. TOPTICA Photonics AG: FPI 100 - Fabry-Perot Interferometer. http://www.toptica.com/products/photonicals/scanning_fabry_perot_interferometer_and_detector.unit
9. National Instruments: NI USB-621x User Manual (2009)
10. National Instruments: LabVIEW 2012 Help - Peak Detector VI (2012). https://zone.ni.com/reference/en-XX/help/371361J-01/lvanls/peak_detector/
11. Demtröder, W.: *Laser Spectroscopy 2: Experimental techniques*. Springer (2008)
12. Campbell, P., Moore, I., Pearson, M.: Laser spectroscopy for nuclear structure physics. *Prog. Part. Nucl. Phys.* **86**, 127–180 (2016)
13. Steck, D.A.: Rubidium 85 D line data. <http://steck.us/alkalidata>. (revision 2.1.6, 20 September 2013)
14. Steck, D.A.: Rubidium 87 D line data. <http://steck.us/alkalidata>. (revision 2.1.5, 13 January 2015)
15. Henderson, A.R.: *Fabry-Perot interferometers*. G. Hernandez Cambridge University Press. *Opt. Laser Technol.* **18**, 274 (1986)
16. Minamisono, K., Mantica, P., Klose, A., Vinnikova, S., Schneider, A., Johnson, B., Barquest, B.: Commissioning of the collinear laser spectroscopy system in the BECOLA facility at NSCL. *Nucl. Instrum. Meth. A* **709**, 85–94 (2013)
17. Zhao, W., Simsarian, J., Orozco, L., Sprouse, G.: A computer-based digital feedback control of frequency drift of multiple lasers. *Rev. Sci. Instrum.* **69**(11), 3737–3740 (1998)
18. Voss, A., Procter, T., Shelbaya, O., Amaudruz, P., Buchinger, F., Crawford, J., Daviel, S., Mané, E., Pearson, M., Al Tamimi, W.: The Collinear Fast Beam laser Spectroscopy (Cfbs) experiment at Triumf. *Nucl. Instrum. Meth. A* **811**, 57–69 (2016)



II

ON THE PERFORMANCE OF WAVELENGTH METERS: PART 1 – CONSEQUENCES FOR MEDIUM-TO-HIGH- RESOLUTION LASER SPECTROSCOPY

by

M. Verlinde, K. Dockx, S. Geldhof, K. König, D. Studer, T. E. Cocolios, R. P. de Groot, R. Ferrer, Yu. Kudryavtsev, T. Kieck, I. Moore, W. Nortershauser, S. Rader, P. Van den Bergh, P. Van Duppen, K. Wendt

Applied Physics B 126, 85 (2020)

Reproduced with kind permission of Springer Nature.

<https://doi.org/10.1007/s00340-020-07425-4>

On the performance of wavelength meters — Part 1: Consequences for medium- to high-resolution laser spectroscopy

M. Verlinde,^{1,*} K. Dockx,¹ S. Geldhof,² K. König,³ D. Studer,⁴ T.E. Cocolios,¹
R. de Groote,² R. Ferrer,¹ Yu. Kudryavtsev,¹ T. Kieck,⁴ I. Moore,² W.
Nörtershäuser,³ S. Raeder,^{5,6} P. Van den Bergh,¹ P. Van Duppen,¹ and K. Wendt⁴

¹*KU Leuven, Instituut voor Kern- en Stralingsfysica, Celestijnenlaan 200D, 3001 Leuven, Belgium*

²*University of Jyväskylä, Department of Physics, FI-40014 Jyväskylä, Finland*

³*Technische Universität Darmstadt, Institut für Kernphysik, 64289 Darmstadt, Germany*

⁴*Johannes Gutenberg-Universität, Institut für Physik, D-55099 Mainz, Germany*

⁵*Helmholtz-Institut Mainz, D-55128 Mainz, Germany*

⁶*GSI Helmholtzzentrum für Schwerionenforschung GmbH, D-64291 Darmstadt, Germany*

Present-day laser-spectroscopy experiments increasingly rely on modern commercial devices to monitor, stabilize and scan the wavelength of their probe laser. Recently, new techniques are capable of achieving unprecedented levels of precision on atomic and nuclear observables, pushing these devices to their performance limits. Considering the fact that these observables themselves are deduced from the frequency difference between specific atomic resonances, in the order of MHz-GHz, the uncertainty on the output of the device measuring the wavelength is often directly related to the final systematic uncertainty on the experimental results. Owing to its importance, the performance of several commercial wavelength meters was compared against different reference sources, including a Scanning Fabry-Pérot Interferometer (SFPI) and a frequency comb. Reproducible, wavelength- and device-dependent disagreements are observed, potentially skewing the experimental output at high precision. In this paper, a practical and relatively inexpensive wavelength meter characterization procedure is presented and validated. This method is capable of improving the precision on wavelength differences considerably depending on the device, while together with a second investigation that is published separately, [1], it offers a full description of the expected wavelength meter performance for users.

I. INTRODUCTION

To run modern laser-spectroscopy experiments, the probe laser requires means to monitor, stabilize and/or scan the wavelength during operation. These tasks are often realized using state-of-the-art commercial wavelength meters, which are capable of performing a wavelength determination for a variety of optical radiation sources ranging from deep UV to infrared in relatively short time scales (> 1 kHz), ideal for fast correction feedback loops. The performance of these wavelength meters has already been the topic of several studies, mainly focused on their performance stability (see e.g. [2–6]).

A specific field of use of these devices, is the study of exotic radionuclides at Radioactive Ion Beams (RIB) facilities via hyperfine laser spectroscopy. This technique provides information on the electromagnetic structure of the nucleus by offering a nuclear-model independent window to the nuclear spin, nuclear moments and differences in mean-square charge radii, for a range of isotopes [7, 8]. The hyperfine structure, carrying the nuclear information imprinted in the form of frequency differences between specific closely-spaced resonances in the atomic spectrum (MHz-GHz energy scale), can be uncovered with varying degrees of precision (defined here via the Full-Width-at-Half-Maximum (FWHM), Δf_{FWHM} , of the obtained resonance). As the production rate of nuclei decreases as

one pushes to more exotic species, Resonant Ionization Spectroscopy (RIS), whereby the number of ions produced as a function of laser wavelength is monitored, is the technique of choice due to the high efficiency of counting ions or detecting the radioactive decay signal. A number of RIS techniques exist, adapted to the environment in which the atomic species of interest are probed, which eventually defines the achievable precision [9]. These techniques are, for example: RIS in a hot-cavity source or in a gas cell ($3 \text{ GHz} < \Delta f_{\text{FWHM}} < 10 \text{ GHz}$ [10, 11]), RIS in a perpendicular geometry, which can be realized in a gas jet or within the PI-LIST ion source ($0.1 \text{ GHz} < \Delta f_{\text{FWHM}} < 1 \text{ GHz}$ [11, 12]) and with collinear techniques on fast ion/atom beams ($\Delta f_{\text{FWHM}} \approx$ natural linewidth [13]). In order to reduce the linewidth of the hyperfine resonances, and, hence, to provide higher precision data on the nuclear observables, the latter two techniques are pushing the limits on accurate frequency determination by using commercial wavelength meters for monitoring, stabilizing and potentially scanning the probe laser [6].

As the final hyperfine observables of interest are directly related to the ill-defined uncertainty of the readout of this wavelength meter, it is important to understand its performance in determining frequency differences $\nu_{\alpha\beta} = \nu_{\beta} - \nu_{\alpha}$ of the order $\sim \text{MHz/GHz}$ over the complete operational spectral range. Additionally, as the isotopes of interest are becoming increasingly exotic and, thus, only produced in minute quantities, the performance stability over longer periods of time, re-

* Matthias.Verlinde@kuleuven.be

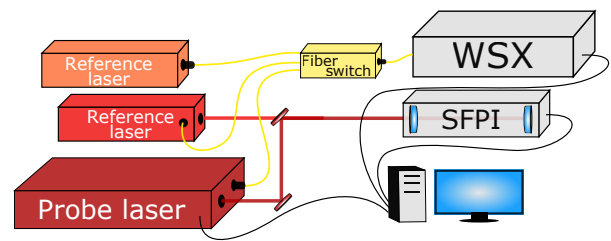
quired to obtain sufficient statistics, is crucial. Moreover, RIS most often relies on the measurement of one isotope at a time, so that the accurate determination of isotope shifts strongly depends on the comparability of the data and, thus, the reproducibility of the frequency determination. In this paper, we report on a reliability study performed in different laboratories using different wavelength ranges, different wavelength meters and different measuring protocols with the goal to provide an easy, cost-friendly, widely-applicable and potentially performance-increasing, wavelength meter characterization procedure. The wavelength meters of interest in this paper and [1] belong to the WS series from HighFinesse GmbH. These devices consist of beam optics coupling the laser light, entering the device via an optical fiber, into Fizeau interferometers. The induced interference pattern is imaged on a CCD photodiode array. The obtained spectrum is fitted and compared to the calibration pattern resulting in a wavelength determination. Here, we will concentrate on the accuracy of relative frequency measurements, while in a second study, the focus will lie on the accuracy of absolute frequency determinations [1].

To determine the precision on $\nu_{\alpha\beta}$, $\Delta\nu_{\alpha\beta}$, for different wavelength meters in different wavelength ranges, the readout of these devices was compared to another reference. To summarize the tests, the paper is structured as follows. In Sec. II, the capabilities of several wavelength meters (WS series HighFinesse GmbH, when no specific type is specified the notation WSX is used) to accurately measure frequency differences, $\nu_{\alpha\beta} = \nu_{\beta} - \nu_{\alpha}$, in a range of ~ 10 GHz is investigated with the aid of a Scanning Fabry-Pérot Interferometer (SFPI), a frequency comb and an ionic resonance. Sec. III contains a description of the temporal stability of these devices and different solutions on how to improve it. Several measurement methods are combined to give a comprehensive overview for a number of devices over a large spectral range. In Sec. IV, a validation of the results from Sec. II is done by performing laser spectroscopy on $^{63,65}\text{Cu}$ isotopes in an Atomic-Beam Unit (ABU) and in a gas-jet environment, confirming the necessity of a proper wavelength meter characterization.

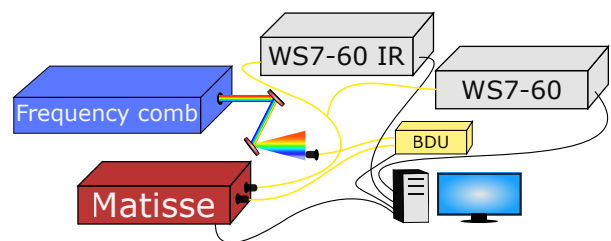
II. DETERMINATION OF $\Delta\nu_{\alpha\beta}$ (WSX)

A. WSX-SFPI comparison

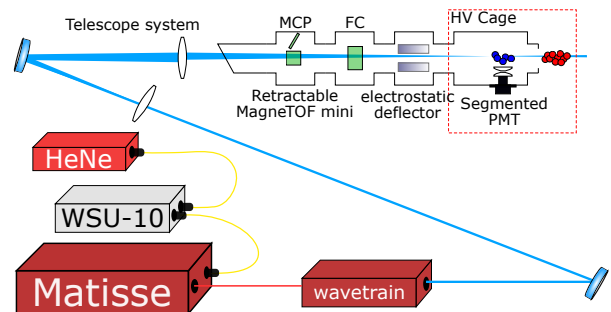
The first series of tests were performed at the In-Gas Laser and Ionization Spectroscopy (IGLIS) laboratory at KU Leuven, Belgium. This facility has been built to carry out a full characterization, validation and optimization of the in-gas-jet spectroscopy for its later implementation in a number of online accelerator facilities (S3 LEB, MARA LEB, GSI), to study, amongst others, the heavy and super heavy elements [11]. In the in-gas-jet method, the atoms of interest are embedded in a low-



(a) Simplified schematic layout of a general setup used to compare the output of an SFPI with that of a specific wavelength meter. The probe laser is measured by a specific WSX wavelength meter together with a reference laser. The wavelength scan of the probe laser is controlled externally by a feedback loop, based on the readout of the WSX. One reference laser is also overlapped with the probe laser and directed to the SFPI. For details, see text.



(b) Simplified schematic layout of the continuous wave (cw) laser setup at TU Darmstadt. The Matisse 2 TS laser frequency, locked to both reference cavity and FC1500 frequency comb, is monitored during a wavelength scan by the WS7-60 wavelength meters and by the comb itself via a Beat Detection Unit (BDU). For details, see text.



(c) Schematic view of the light collection region and laser systems of the collinear beamline at IGISOL for the measurements on ^{89}Y . The ion beam enters the beamline from the right side. The laser interaction region is monitored by a segmented Photo-Multiplier Tube (PMT) for resonance fluorescence detection.

Figure 1: Experimental techniques used in this work.

density and low-temperature gas jet environment, minimizing the spectral pressure and temperature broadening mechanisms, while still offering high selectivity, short extraction time (< 0.5 s), high efficiency and an indepen-

dence to the chemical nature of the species of interest [14]. To probe the hyperfine structure of the atoms embedded in the gas jet, high-repetition rate, high-power dye lasers are available, supported by a pulsed dye amplifier system seeded with a cw single-mode diode laser for high-resolution laser operation [15].

A second set of characterization tests were performed in the RISIKO laboratory at Johannes Gutenberg-University (JGU) Mainz, Germany. This facility is in use for studies on beams of stable or long-lived radioactive ions, in combination with related development on hot cavity laser ion sources, dedicated laser systems and spectroscopic techniques. The laser ion source here is based on high-repetition rate pulsed Ti:sapphire lasers specifically developed for this application [16]. While these lasers provide high output power required for efficient ionization, a complementary cw laser system provides the stability and narrow linewidth necessary for ultra-trace analysis applications [17, 18] and high-resolution spectroscopy [19–21]. The benefits of both systems can be combined by using a cw external cavity diode laser (ECDL) as master laser for seeding of a pulsed injection-locked Ti:sapphire laser (slave). This combination provides both, high-power pulsed laser radiation and a narrow spectral linewidth of ≈ 20 MHz with appropriate stability [22, 23], well suited for sensitive RIS studies.

Measurement protocol

The tests at the IGLIS laboratory were done by studying, simultaneously, the readout of a wavelength meter (WS7-60, acquired in 2012), which has a quoted accuracy of 60 MHz (according to the 3σ criterion) in the range 420–1100 nm, and a Scanning Fabry-Pérot Interferometer (SFPI, Toptica FPI-100-0500-1) with a Free Spectral Range (FSR) of 4 GHz. A schematic overview of the setup is given in Fig. 1a. The IGLIS control software performs a stepwise frequency scan of a diode laser (TA:pro, TOPTICA Photonics AG) by applying a DC voltage to the DC 110 diode laser driver, a component of the Diode Laser Driver Electronics (Sys DC 110, TOPTICA Photonics AG), via a pulse generator (PicoScope 5000a, Pico Technology). This voltage is amplified in the DC110 diode laser driver and applied to a piezo actuator in the diode laser for accurate control of the laser wavelength. The TA:pro laser, lasing around 654.9 nm, is stabilized relative to the WS7-60’s readout of either a 770.108796 nm diode reference laser (DL pro 780, TOPTICA Photonics AG), frequency locked to a potassium cell (CoSy, TEM Messtechnik GmbH), or a 632.991026 nm frequency-stabilized HeNe laser (Model 32734, Research Electro-Optics, Inc.) during a laser scan, see [15]. For the wavelength determination via the SFPI, both TA:pro and HeNe laser beams are overlapped in the SFPI. In this way, both wavelength measuring devices contain a reference source for calibration and stabilization purposes. A finesse, $\mathcal{F} \approx 300$, is obtained in

the SFPI for both TA:pro and HeNe laser light. To provide optimal working conditions for the SFPI, a scanning range of its piezo actuator is chosen such that a previously optimized number of fringes (≈ 10) of both lasers is visible in one single voltage ramp. At each wavelength step of the TA:pro, one or more traces of the SFPI’s diode sensor are recorded. Off-line, all data are analyzed with a Python-based algorithm. This program uses peak finder and peak tracker algorithms to identify HeNe and TA:pro fringes, fitting each with Gaussian profiles. The fringe positions of the HeNe laser are used as a ruler to accurately transform the time positions of each fringe into a frequency value via the known FSR. After this procedure the average position of the TA:pro fringes of each trace in the frequency domain is saved together with their standard deviation. In case higher precision is required, multiple traces can be extracted at each wavelength, providing a final value as the weighted average with corresponding uncertainty, taking into account the reduced χ^2 .

At the RISIKO laboratory, a similar comparison was performed between a wavelength meter (WSU-30, acquired in 2003) and a home made SFPI. The WSU-30(UV) wavelength meter has an accuracy of 30 MHz in the range 248–1180 nm. The scanning ECDL consists of a custom-built mount with a piezo-actuated grating for external feedback, and a Peltier element for temperature stabilization, supplied by commercial laser driver electronics (LDC202, Thorlabs Inc.). In total two different laser diodes were used in this setup (RWE-920, RWE-980, Eagleyard Photonics GmbH). Fast stabilization and scanning operation is performed with a quadrature interferometer, (iScan, TEM Messtechnik GmbH). The longterm and accurate stabilization of the ECDL set frequency is obtained from an SFPI via a fringe offset locking (FOL) technique [24]. More information on the laser setup can be found in [25]. Here, the light from the probe ECDL and from a stabilized HeNe laser (SL-03, SIOS Messtechnik GmbH) is overlapped in a custom-built confocal SFPI, with a piezo-actuated mirror. The SFPI has a free spectral range of $\text{FSR} = 298.721$ MHz and a Finesse of $\mathcal{F} \approx 400$. Depending on the wavelength, the piezo ramp covers 2–3 fringes. The transmission of the probe ECDL and the HeNe fringes are separated by a dichroic mirror and detected with separate photodiodes. The time difference of the first ECDL fringe after the start of the voltage ramp is measured with respect to the fringe from the reference HeNe laser via a counter card and the frequency change is evaluated using an Arduino MCU, via the precisely known FSR and HeNe wavelengths. To ensure proper single-mode operation of the ECDL, the time between the first and the second fringe is in addition evaluated. Values of the mean relative frequency and frequency jitter within a time of ≈ 50 ms (matched to the data acquisition cycle of the wavelength meter) are sent to a LabVIEW interface, used for controlling, monitoring and recording. An absolute frequency measurement is provided by the WSU-30,

where both the probe ECDL and the stable HeNe output are measured through a multichannel switch (High-Finesse GmbH). The absolute reference and calibration source for the wavelength meter is an additional ECDL (DL pro 780, Toptica Photonics AG), coupled to a compact rubidium saturated absorption spectroscopy setup (SAS) (CoSy 4.0, TEM Messtechnik GmbH). By using a dither-lock stabilization (LaseLock 3.0, TEM Messtechnik GmbH), it is locked to the $F = 2 \rightarrow F = 3$ transition in the D2 line of ^{87}Rb at 780.24602 nm. A schematic overview of this setup is shown in fig. 1a.

To compare the relative performance of both SFPI and wavelength meter during a frequency scan, the magnitude of each laser step with respect to the starting point of the scan is monitored for both devices. Finally, the difference in the step size as measured by the SFPI and wavelength meter, respectively, is subtracted to obtain a relative result. Mathematically, the final output $\Delta_{\text{SFPI-WSX}}(\nu)$ for a random wavelength meter WSX, reads as follows:

$$\begin{aligned} \Delta_{\text{SFPI-WSX}}(\nu) &= \Delta_{\text{SFPI}}(\nu) - \Delta_{\text{WSX}}(\nu) \\ &= (\nu_{\text{SFPI}} - \nu_{0,\text{SFPI}}) - (\nu_{\text{WSX}} - \nu_{0,\text{WSX}}). \end{aligned} \quad (1)$$

In Eq. (1), ν_{WSX} represents the frequency readout at a certain moment during a laser scan while $\nu_{0,\text{WSX}}$ represents a reference point within the scan.

Results

The procedure described for the IGLIS laboratory, using the setup in Fig. 1a, was applied to a number of scan ranges. The results for $\Delta_{\text{SFPI-WS7}}(\nu)$, defined in Eq. (1), in the 654.9570-654.9969 nm range (spanning roughly 28 GHz in total) are shown in Fig. 2. These results show that the WS7-60 and SFPI disagree reproducibly on the step size taken by the TA:pro laser with a maximum of 8 MHz, with an additional degree of periodicity. To map this periodicity, a triangular wave form was fitted to the data of Fig. 2 without any prior knowledge on the underlying mechanism:

$$\begin{aligned} \Delta_{\text{triangle}}(\nu) &= \frac{4A}{T} \left((\nu + S) - \frac{T}{2} \left[\frac{2(\nu + S)}{T} + \frac{1}{2} \right] \right) \\ &\cdot (-1)^{\lfloor \frac{2(\nu + S)}{T} + \frac{1}{2} \rfloor}. \end{aligned} \quad (2)$$

This function of the frequency ν has three parameters; the amplitude, A , period, T and shift, S , of the triangular wave. The fitting procedure reveals a peak-to-peak amplitude $A_{655}^{\text{WS7}} = 8.2(2)$ MHz and a period $T_{655}^{\text{WS7}} = 3.871(10)$ GHz for Eq. (2). The period matches closely to the FSR of the most precise interferometer of the WS7-60 wavelength meter (≈ 4 GHz). To understand the behavior of the WS7-60 in more detail, the wavelength range 654.973-654.985 nm was scanned with higher resolution (≈ 10 traces per wavelength

step were combined). The results of this measurement are shown in yellow in Fig. 2 with a magnified region shown in Sec. IV, Fig. 10. The finer details observed in Fig. 10 shows that the underlying mechanism, causing the disagreement between the WS7-60 and SFPI, is of a more complex nature than a simple triangular waveform. However, the general features of the disagreement between both devices are clear. The data of Fig. 2 present multiple measurements confirming the reproducibility of the results. Additionally, the structure obtained for Fig. 2 is independent of the calibration laser. The specific calibration tool only causes an absolute offset, not visible in these measurements.

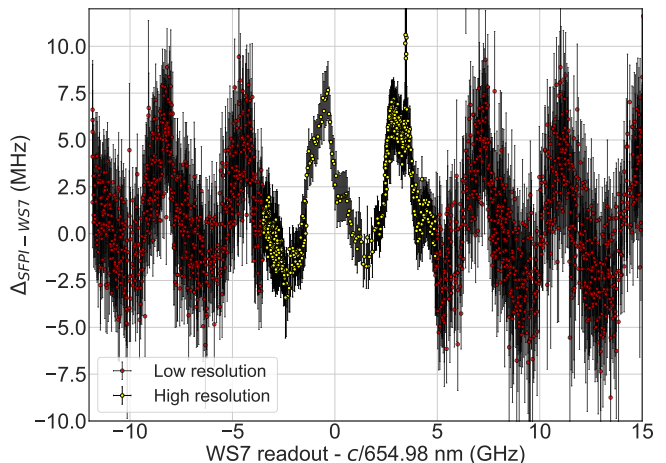


Figure 2: The results for $\Delta_{\text{SFPI-WS7}}(\nu)$, defined in Eq. (1), recorded at the IGLIS laboratory. The results presented here combine multiple scans taken at different times to prove the reproducibility of the data. For details, see text. c presents the speed of light in m/s.

The comparison between the WSU-30 wavelength meter and the home made SFPI at the RISIKO laboratory is presented in Fig. 3 (middle and bottom panel). The data in Fig. 3 shows also a periodic deviation of the WSU-30 readout with respect to the SFPI, calculated according to Eq. (1), with $\nu_{0,\text{WSU30}} = c/905.795$ nm and $\nu_{0,\text{WSU30}} = c/938.853$ nm for middle and lower graph, respectively ($\nu_{0,\text{SFPI}} = 0$). In both measurements a calibration of the wavelength meter was performed after each data point, to exclude any time-dependent drifts of the wavelength meter performance, as discussed in the next section. The rather large scatter in the scan at 905 nm arises from stability issues of the probe ECDL, which may be caused by internal feedback in the laser diode, owing to an inferior anti-reflection coating of the front window. The different colors represent measurements performed on different days over the same frequency range and underline the reproducibility of the periodic pattern. Minor shifts may be caused by drifts of the HeNe laser (i.e. the SFPI reference), but still lie within the specified stability. Fitting all datapoints of one frequency range with the tri-

angular pattern from Eq. (2) yields a period of $T_{905}^{\text{WSU30}} = 1.923(14)$ GHz and $T_{938}^{\text{WSU30}} = 1.912(12)$ GHz, close to the FSR of the final WSU-30 interferometer of ≈ 2 GHz. The peak-to-peak deviation is $A_{905}^{\text{WSU30}} = 5.1(3)$ MHz and $A_{938}^{\text{WSU30}} = 5.3(2)$ MHz, respectively. To confirm both the IGLIS and RISIKO data acquisition and in general the SFPI measurement procedure, the WSU-30 wavelength meter was remeasured at the IGLIS laboratory in the wavelength range around 654.980 nm. The results are shown in Fig. 3 (top panel) and they confirm both the ≈ 2 GHz period for this WSU-30 and the smaller amplitude compared to the WS7-60 ($A_{655}^{\text{WSU30}} \approx 5$ MHz). While the 'global' periodicity of the signal is easily distinguished, extra structures are clearly visible. The obtained results for $\Delta_{\text{SFPI-WSU30}}$, also, clearly show both a wavelength range and device-specific dependency of the wavelength meter response, as was confirmed in the next measurements.

B. WSX-frequency comb comparison

A third series of wavelength meter tests was performed at the Collinear Apparatus for Laser spectroscopy and Applied physics (COALA) at TU Darmstadt, Germany. This laboratory was originally designed for accurate high-voltage evaluations based on Collinear Laser Spectroscopy (CLS) operation. Nowadays, precise measurements of absolute transition frequencies and isotope shifts in ions are also performed to benchmark atomic theory and to support on-line investigations of short-lived isotopes. For this purpose, a cw laser system based on Ti:sapphire lasers combined with Wavetrain frequency doublers is available alongside a GPS-referenced frequency comb to determine and stabilize its frequency [1, 26, 27].

Measurement protocol

At the COALA laboratory the output of both the IGLIS WS7-60 wavelength meter and the in-house WS7-60-IR (630-1750 nm, acquired in 2007) device was compared to the frequency comb (FC1500-250-WG, Menlo Systems) and the accuracy of the wavelength meter's absolute readout could be tested. The setup is shown in Fig. 1b. A Ti:sapphire laser (Matisse 2 TS, Sirah) is stabilized to its reference cavity to avoid short-term frequency fluctuations. Additionally, a slower stabilization feedback loop for long-term stabilization is realized using the frequency comb. To achieve this, the beat frequency between the nearest comb mode and the Ti:sapphire beam is measured in a fiber-coupled beat detection unit (BDU) and digitally communicated to the Matisse commander software, which adapts the length of the reference cavity to keep the beat frequency constant. In this way, an accurate and stable absolute reference is available with a precision of better than 100 kHz, limited by the linewidth

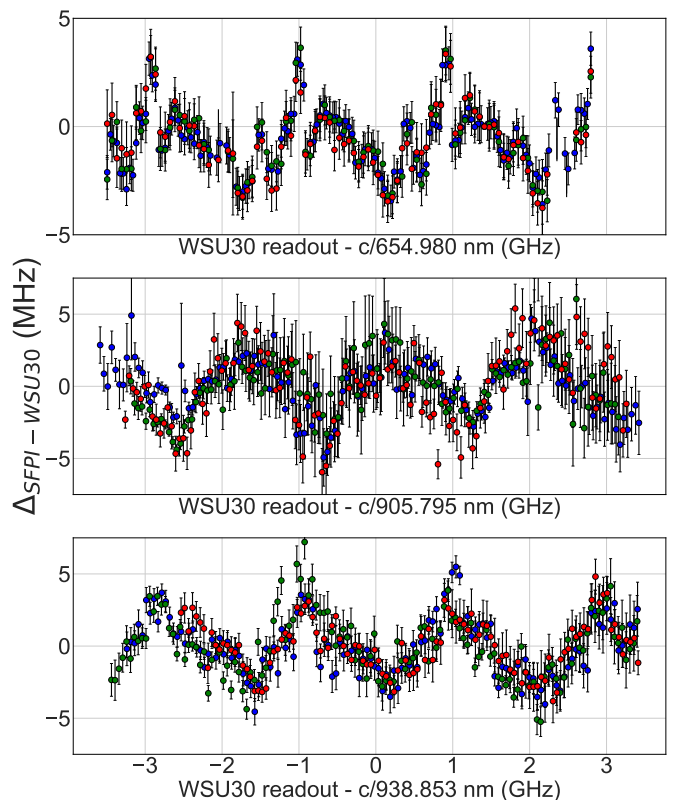


Figure 3: Results for $\Delta_{\text{SFPI-WSU30}}$, measured for three different laser wavelength ranges. The upper panel at 654.980 nm was obtained at the IGLIS laboratory. Each data point of the upper panel is taken as the weighted average with corresponding uncertainty of the results from 10 SFPI traces, obtained via Eq. (1), at a distinct frequency. Around 10 consistent measurements were taken, from which three are shown in the upper panel.

The other panels, scanned at 905.795 nm and 938.853 nm, respectively, were measured at the RISIKO laboratory in Mainz. The results are obtained with a similar analysis to the one in the IGLIS laboratory, and the final data points represent the average and standard deviation of all SFPI results taken within one wavelength bin. 11 and 8 consistent measurements were taken for the 905 nm and 938 nm cases, respectively, from which again three full range results are shown in both panels. All three measurements for $\Delta_{\text{SFPI-WSU30}}$ show the same period in their structure.

of the Matisse. For the measurements performed here, the laser is scanned across a similar frequency range as in the IGLIS/RISIKO measurements, locked to the frequency comb at every wavelength step. The customized data acquisition system records the readout from both the frequency comb and the two WS7-60 wavelength meters. With this setup, both relative and absolute performance of the WS7-60 can be mapped across a large wavelength range.

As the combination of the frequency comb and the Ma-

tisse laser at the COALA laboratory offers a reference with a well-known frequency, one can go a step further than Eq. (1) and compare directly the frequency output of both devices:

$$\Delta_{\text{Comb-WSX}}(\nu) = \nu_{\text{Comb}} - \nu_{\text{WSX}}. \quad (3)$$

In this case, the wavelength meters are not only tested in their ability to determine $\nu_{\alpha\beta}$ but also in measuring ν_{α} itself.

Results

The results for the comparison between the WS7-60 and WS7-60-IR wavelength meters and the FC-1500 frequency comb, performed at the COALA laboratory, are shown in Fig. 4. They are obtained from a scan of the Matisse laser across ≈ 16 GHz around 805.56 nm and 795.56 nm, and across ≈ 8 GHz around 856.45 nm, respectively. The wavelength meters are calibrated at 812.77 nm using the frequency-comb stabilized Matisse, for the measurements at 805 nm and 856 nm and at 632.99 nm with a frequency-stabilized HeNe laser (SIOS SL 03, Meßtechnik GmbH) for the measurement at 795.56 nm. To identify device-dependent effects, a WS7-60-IR was included in the measurements. From Fig. 4, it follows that similar periodic patterns arise at different wavelength ranges, with similar peak-to-peak discrepancies for both wavelength meters. The structure is found to be highly reproducible over months in previous measurements performed at COALA [1]. Inspecting both Figs. 2 and 4 indicates a wavelength dependence of the discrepancy between the reference and the WS7-60. Additionally, both devices do not react in the same way, indicating an additional device-dependent effect on the results of $\Delta_{\text{Comb-WS7}}(\nu)$. Finally, it should be mentioned that the structure in the results of Fig. 4 also does not depend on the specific calibration point of the laser. Only the absolute offset to the real wavelength determined with the frequency comb might change, which is strongly wavelength-dependent itself. This as well as a full description of the frequency-comb based specification of various high-precision wavelength meters is presented in [1].

C. WSX-ionic resonance comparison

A final series of measurements was done at the IGISOL facility of the Accelerator Laboratory in the University of Jyväskylä, Finland. This facility uses the ion guide technique for the production and study of low-energy beams of exotic radioactive nuclei [28]. Fundamental nuclear ground and isomeric state properties and mass are probed using a variety of ion (and atom) manipulation devices including ion traps, radiofrequency (rf) cooler-bunchers as well as methods of optical spectroscopy.

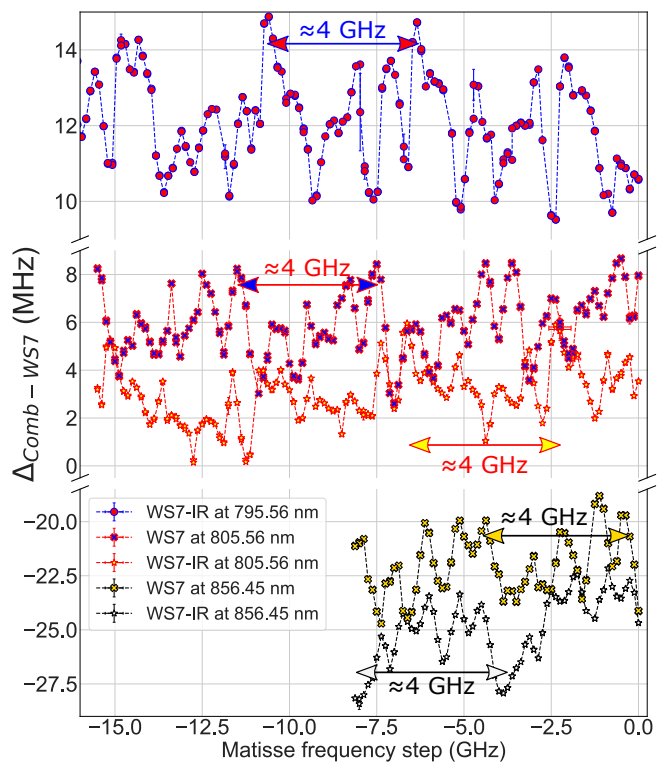


Figure 4: Benchmarking the performance of two different WS7-60 devices, in the vicinity of 805.56 nm, 856.45 nm, and 795.56 nm against a frequency-comb measurement of the laser frequency resulting in $\Delta_{\text{Comb-WS7}}(\nu)$.

Over the years an expanding program of optical spectroscopy at the facility has resulted in a variety of improvements to methods including collinear laser spectroscopy as well as resonance ionization spectroscopy. The former technique is applied for high-resolution spectroscopy on fast ionic and atomic beams, routinely providing measurements of optical frequency splittings to 1-10 MHz precision. For these applications, a high-resolution laser spectroscopy setup based on a Matisse 2 TS laser and a Wavetrain frequency doubler, is available. Additional infrastructure includes an injection-locked Ti:sapphire laser, seeded by the Matisse cw light, and several wavelength reference options.

Measurement protocol

At the IGISOL facility beam line for collinear laser spectroscopy, a wavelength meter (WSU-10, acquired in 2017), with a specified 10 MHz accuracy, was investigated. A schematic of the laser system and light collection region of the collinear beam line can be seen in Fig. 1c. More details on the beamline and data acquisition system can be found in [29]. Stable ^{89}Y , pro-

duced by a spark discharge source, was measured on the 363.4157 nm transition from the ionic ground state using the Matisse TS laser, pumped by a cw frequency doubled YAG-laser (Millenia eV, Spectra Physics) and stabilized to a fixed setpoint in the wavelength meter. Resonant interaction between the anti-collinear laser beam and ions is measured by monitoring the optical deexcitation of the excited state with a segmented Photo Multiplier Tube (PMT). The hyperfine structure can be mapped by tuning the acceleration voltage of the ion beam. To probe systematic discrepancies between the WSU-10 and the centroid of the 363.4157 nm transition used as a reference, the stabilization setpoint was changed in steps of 600 MHz, and for each setpoint a spectrum with sufficient statistics (> 1000 counts on the resonance peak) was collected.

For the IGISOL wavelength meter tests, the centroid of ^{89}Y presents an absolute reference while it is assumed that the voltage scan is identical for every measurement. This results in:

$$\Delta_{\text{Centroid}}(\nu) = (V_{\text{Centroid},\nu} - V_{\text{Centroid},\nu_0}) \frac{\partial \nu}{\partial V}. \quad (4)$$

Here $V_{\text{Centroid},\nu}$ is the voltage at which the centroid of the transition is obtained for a random measurement at fixed setpoint ν and $V_{\text{Centroid},\nu_0}$ is the same for a reference measurement. $\partial \nu / \partial V$ converts the acceleration voltage difference to a frequency difference via the Doppler shift. In this way, similar results are obtained as for Eq. (1) and Eq. (3).

Results

The resulting ^{89}Y hyperfine spectrum consists of an unresolved doublet, which was fitted by fixing the hyperfine parameter of the upper state to the literature value of 32.6(1) MHz [30]. The fitted centroid frequencies of the 363.4157 nm transition, obtained from the collinear beam line at IGISOL, are depicted in Fig. 5. A triangular wave pattern applied to the data, following Eq. (2), resulted in a peak-to-peak amplitude of $A_{727}^{\text{WSU}10} = 1.3(3)$ MHz, which is almost an order of magnitude smaller than for the WS7-60. The period $T_{727}^{\text{WSU}10} = 1.99(12)$ GHz, is consistent with the ≈ 2 GHz FSR of the most precise interferometer in the wavelength meter.

D. Summary

In summary, the results indicate that each wavelength meter has its characteristic $\Delta \nu_{\alpha\beta}$ that is unique for every instrument separately. It can be extracted from $\Delta_{\text{SFPI-WSX}}(\nu)$, $\Delta_{\text{Comb-WSX}}(\nu)$ and $\Delta_{\text{Centroid}}(\nu)$, depends on the wavelength range of interest and is characterized by a periodic structure which follows the FSR

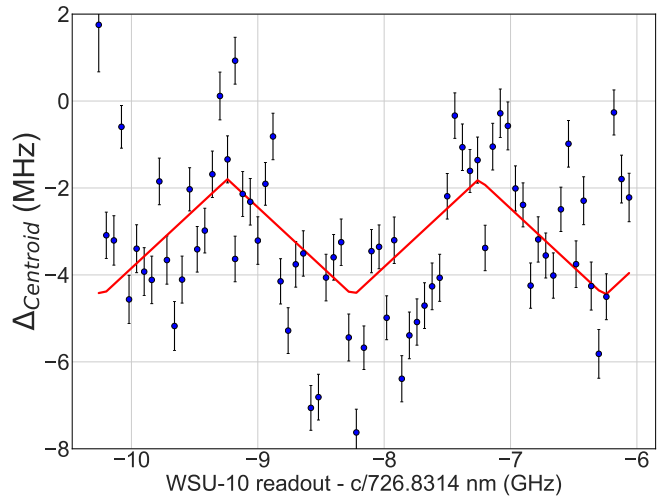


Figure 5: The fitted centroid of the ^{89}Y hyperfine structure at changing laser stabilization setpoints using the WSU-10 wavelength meter (blue). The resulting data has been fitted using a triangular wave function according to Eq. (2) (red solid line).

of the most precise interferometer in the device. To obtain a value for $\Delta \nu_{\alpha\beta}$, one should perform a characterization procedure as presented here and further elaborated on in Sec. IV, or otherwise remain with the conservative absolute accuracy mentioned by the manufacturer. To assess the potential systematic uncertainty to be expected, our data is summarized in Table I, which contains the A_{λ}^{WSX} alongside the outer boundaries of the $\Delta_{\text{SFPI-WSX}}(\nu)$, $\Delta_{\text{Comb-WSX}}(\nu)$ and $\Delta_{\text{Centroid}}(\nu)$ distributions covering 95% or 99.7% of all measurements.

III. TEMPORAL STABILITY OF $\nu_{\alpha}(\text{WSX})$

Following a comparison of the performance of different wavelength meters in determining $\nu_{\alpha\beta}$ in a range of ~ 10 GHz with that of an SFPI and a frequency comb, its stability over time is mapped. A well-known feature of these wavelength meters is their tendency to drift over longer periods of time, strongly correlated to external temperature and/or pressure instabilities. The magnitude of these drifts is most often in the range of a few MHz/hour dependent on the magnitude of the time derivative of the external conditions. During longer measurement times, these drifts will have a profound impact on the results obtained. Two options exist to compensate for the time-dependent readout of the wavelength. First of all, one can correct for the drift of the scanning laser by monitoring the wavelength of an externally locked reference laser at the same time, which will be discussed in Sec. III A. Secondly, a periodical calibration of the wavelength meter can be included in the control software of the laser, see Sec. III B.

To exemplify the importance of a well-controlled external

Wavelength meter	Wavelength probe (nm) [$\pm 5 - 20$ GHz]	A_λ^{WSX} MHz	Q_{95} (MHz)	$Q_{99.7}$ (MHz)
WS7-60	655.0	8.2(2)	11.7	18.0
WS7-60	856.5	≈ 3.5	5.0	5.9
WS7-60	805.6	≈ 5	5.1	6.1
WS7-60-IR	856.5	≈ 4	5.7	6.2
WS7-60-IR	805.6	≈ 3.5	4.7	5.8
WS7-60-IR	795.6	≈ 5	4.5	5.4
WSU-30	655.0	≈ 5	6.4	7.3
WSU-30	905.8	5.1(3)	8.8	13.7
WSU-30	938.9	5.3(2)	7.2	11.6
WSU-10	726.8	1.3(3)	7.2	9.2

Table I: The peak-to-peak amplitude A_λ^{WSX} and outer boundaries of the $\Delta_{\text{SFPI-WSX}}(\nu)$, $\Delta_{\text{Comb-WSX}}(\nu)$ and $\Delta_{\text{Centroid}}(\nu)$ distributions, covering 95% or 99.7% of all measurements performed, Q_{95} and $Q_{99.7}$. When no explicit correction to the wavelength meter output is applied, see Sec. IV, Q_{95} and $Q_{99.7}$ should be taken into account to determine the systematic uncertainty on a determination of $\Delta\nu_{\alpha\beta}$ in a specific wavelength range. The Q values are not only influenced by the wavelength meter but also by the uncertainty of the analysis procedure. The values of A_λ^{WSX} are approximated in case the discrepancy of the wavelength meter shows significant deviation from Eq. (2).

environment on the wavelength meter’s long-term performance, the Matisse 2 TS laser at IGISOL was stabilized to a Rb hyperfine peak using a side-of-fringe stabilization method implemented in LabVIEW while being monitored by the WSU-10. Any wavelength meter drifts are then transferred to the device’s readout. The largest variation seen is approximately 4 MHz over 24 hours. This stability is in part due to the stable laboratory environment, with laboratory temperature control and minimal disturbance. To account for larger drifts in less stable conditions, they can be corrected for by (auto-)calibrating the device to a frequency-stabilized HeNe laser at certain times suitable to the ongoing measurements, see Sec. III B. Because the high resolution work at the collinear beam line of IGISOL is performed with a fixed laser frequency setpoint, the Matisse transfer cavity can be used to bypass the wavelength meter in general. In this case, a digital plugin of the Matisse control software uses the intensity of the HeNe (HRS015B, Thorlabs Inc.) measured behind the reference cell with a photodiode (PDA36A-EC, Thorlabs Inc.) to stabilize the reference cell length with the side-of-fringe locking method. In this manner, the absolute frequency stability is now directly related to the frequency stability of the HeNe laser, eliminating the need for the wavelength meter. Collinear laser spectroscopy on stable even-even ytterbium isotopes was performed using either the wavelength meter or the transfer cavity for frequency stabilization to verify proper functioning of the transfer cavity. The scatter on the fitted centroids for each isotope, measured in the course of a few hours, was reduced when stabilized to the transfer cavity compared to the wavelength meter, confirming the wavelength meter as a possible source of systematic uncertainty, see Fig. 6.

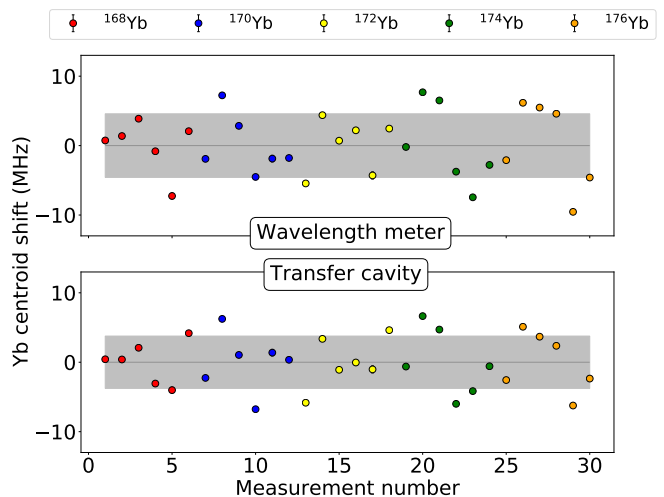


Figure 6: Scatter of the ^{168}Yb , ^{170}Yb , ^{172}Yb , ^{174}Yb and ^{176}Yb centroids, obtained through collinear laser spectroscopy for different measurements stabilizing the probe laser to either the WSU-10 wavelength meter or the Matisse 2 TS transfer cavity. All centroids of a specific isotope, which were measured with a total of 6 different laser setpoints, are compared to their average. The 1σ confidence level was reduced from 4.6 MHz to 3.8 MHz when stabilization to the transfer cavity was done.

A. Drift correction

The most general correction to drifts in the wavelength meter output, in the presence of a reference laser, can be written as follows:

$$\nu'_{\text{corr,WSX}} = \nu_{\text{set}} + \beta(\nu_{\text{set}}, \nu_{\text{ref}}, t)(\nu_{\text{ref}} - \nu_{\text{ref,WSX}}). \quad (5)$$

ν_{set} is the originally defined setpoint at which the laser should be stabilized, ν_{ref} represents the absolute frequency of the reference laser and $\nu_{\text{ref,WSX}}$ is the reference's wavelength meter readout. The parameter $\beta(\nu_{\text{set}}, \nu_{\text{ref}}, t)$ takes into account any kind of frequency and/or time-dependent differences between the drift of the reference laser and the probe laser. As outlined in [15], the IGLIS control software stabilizes the scanning TA:pro's frequency at a wavelength $\nu'_{\text{set,WS7}}$ in the WS7-60, with $\beta(\nu_{\text{set}}, \nu_{\text{ref}}, t) = 1$. Doing so, wavelength meter dependent drifts in time, which can be as large as 5 MHz/h for the WS7-60 of interest, are corrected. To identify higher order (wavelength and/or time-dependent) corrections to $\nu'_{\text{set,WS7}}$ in the form of

$$\beta(\nu_{\text{set}}, \nu_{\text{ref}}, t) = \frac{\nu'_{\text{set,WS7}} - \nu_{\text{set}}}{\nu_{\text{ref}} - \nu_{\text{ref,WS7}}}$$
, three independent measurements were done both at the IGLIS laboratory, a temperature-controlled (± 0.5 °C) ISO8 clean room, and the COALA laboratory (see Figs. 7a to 7c). In all three cases, a HeNe laser was used both to calibrate the wavelength meter and as reference for the correction applied as it is the most common reference source. In addition to the HeNe, another externally stabilized laser, a proxy for the laser to be monitored during the experiment, was read out by the WS7-60 to search for any frequency dependence in $\beta(\nu_{\text{set}}, \nu_{\text{ref}}, t)$. First, the IGLIS TA:pro, stabilized to the wavelength meter readout at 654.97538 nm was included. Secondly, a potassium-locked diode was used at 770.10878 nm, also at the IGLIS laboratory. Finally, a Matisse 2 TS Ti:sapphire laser, locked to the FC1500 frequency comb at the COALA laboratory, was monitored at a wavelength of 787.82884 nm. The drift of the TA:pro was measured by supplying the laser, stabilized to ν_{set} in the WS7-60, also to the SFPI. The data analysis of these results remains the same as described in Sec. II B. For all three measurements, the full drift of the WS7-60's response in ≈ 6 h is mapped together with the results of available corrections. These corrections include $\beta(\nu_{\text{set}}, \nu_{\text{ref}}, t) = 0$, $\beta(\nu_{\text{set}}, \nu_{\text{ref}}, t) = 1$ and $\beta(\nu_{\text{set}}, \nu_{\text{ref}}, t) = \beta(\nu_{\text{set}}, \nu_{\text{ref}})$. The factor $\beta(\nu_{\text{set}}, \nu_{\text{ref}})$ is a reproducible, wavelength-dependent constant, which is obtained after longer periods of drift as can be seen in Figs. 7a to 7c. This number is reproducible for different measurements, independent of the drift rate, showing only a dependence on the device, ν_{set} and ν_{ref} . From the data, one can see that the WS7-60 does not provide a stable read out of the wavelength over time (this would be the case $\beta(\nu_{\text{set}}, \nu_{\text{ref}}, t) = 0$). For the TA:pro at 654.98 nm, $\beta(\nu_{\text{set}}, \nu_{\text{ref}}, t) = 1$ is sufficiently accurate to keep the laser stable to within 1 MHz. This 1 MHz limit was chosen arbitrarily as it is similar to other uncertainties contributing to the laser stability, as will be discussed in Sec. IV. For both infrared lasers, the inclusion of the $\beta(\nu_{\text{set}}, \nu_{\text{ref}})$ factor is required to ensure a similar stability over this time domain. Through these measurements, it can be concluded that a correction to the WS7-60 output with $\beta(\nu_{\text{set}}, \nu_{\text{ref}}, t) = 1$, is sufficient up to scan times of ≈ 30 min. For longer scans, either the $\beta(\nu_{\text{set}}, \nu_{\text{ref}})$ factor

has to be determined and applied, or a recalibration is required with a repetition rate higher than once every ≈ 30 min, as will be discussed next.

B. Periodical calibration

The stability of the WSU-30 wavelength meter readout at the RISIKO laboratory was tested over a period of ≈ 1 day by monitoring the measured frequencies of the Rb-locked ECDL and the HeNe after one initial calibration to the Rb D2 line. In a second measurement, one day later, the wavelength meter was auto-calibrated to the Rb-locked ECDL with a cycle of 10 minutes. The results are presented in Fig. 8. It can be clearly seen that without auto-calibration (AC), the wavelength meter readout drifts over a few tens of MHz, strongly correlated to the temperature. Moreover, at large deviations from the nominal frequency, the HeNe readout seems to drift further than the Rb-locked ECDL, indicating also here $\beta(\nu_{\text{set}}, \nu_{\text{ref}}, t) \neq 1$.

Auto-calibration resolves the long-term stability issues of the wavelength meter readout almost completely. The deviation $\nu - \nu_{\text{cal}}$ to the calibration frequency is < 2 MHz over the measurement duration and can be further reduced by a shorter calibration interval. As a consequence an AC routine was added to the data acquisition cycle, so that the wavelength meter can be calibrated (taking less than 1 s) before moving to the next frequency setpoint. Alternatively, a stable temperature environment for the wavelength meter should provide superior frequency stability than in our test without AC. In this case one should also consider the air pressure in the room, which could not be measured with our device. Newer devices usually have an integrated pressure sensor.

IV. VALIDATION

The reliability of the laser system in general and the WS7-60 wavelength meter in particular was tested by performing hyperfine spectroscopy on the $4s\ ^2S_{1/2}$ ground state (g.s.) to the $4p\ ^2P_{1/2}$ excited state (e.s.) transition in $^{63,65}\text{Cu}$, in an Atomic-Beam Unit (ABU) and in a gas jet, and comparing the results with literature. The resulting data as well as the excitation and ionization scheme are presented in Fig. 10. To achieve the excitation at 327.49 nm, light from the scanning TA:pro laser is amplified in a Pulsed Dye Amplifier (PDA, Sirah Lasertechnik GmbH) and frequency doubled in a BBO nonlinear crystal. The ionization step of 287.98 nm is provided by a broadband tunable dye laser (CREDO, Sirah Lasertechnik GmbH) with also an integrated frequency conversion unit. Both PDA and broadband dye lasers are pumped by Nd:YAG lasers (INNOSLAB, Edgewave GmbH) at 1 kHz with a pulse length of ≈ 7 ns. The ABU provides a copper atom plume by resistively heating a graphite tube filled with copper. After ionization, these atoms experi-

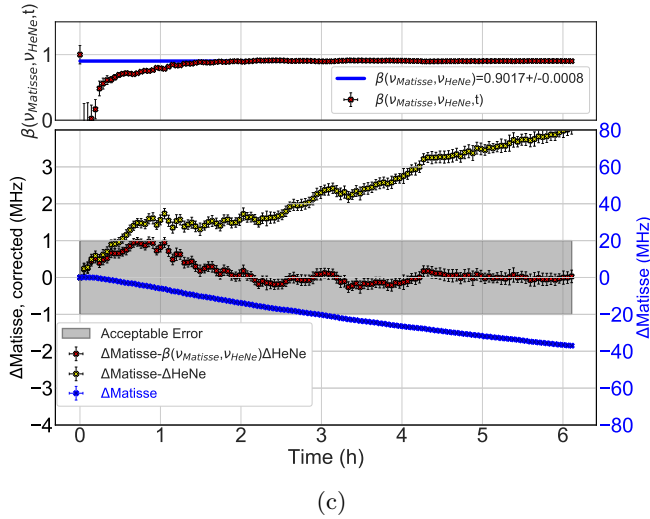
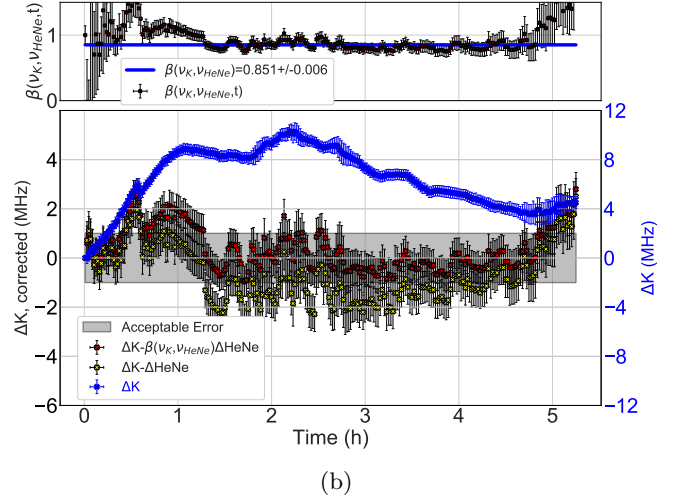
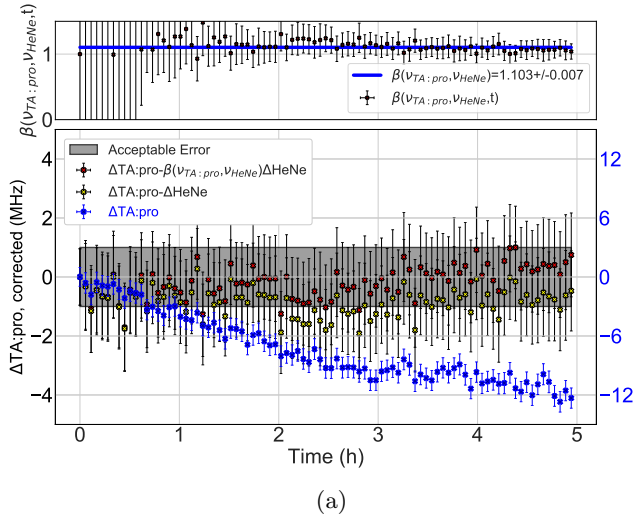


Figure 7: The time dependence of the WS7-60's response to an externally locked laser at 654.97538 nm (Fig. 7a), 770.10878 nm (Fig. 7b) and 787.82884 nm (Fig. 7c), respectively. The drift is defined as $\Delta X = \nu_{\text{WS7}}(t) - \nu_{\text{WS7}}(t_0)$, with t_0 being the time of calibration and X the specific laser used. The uncorrected readout (right axis, blue) is plotted alongside possible corrections (left axis, yellow for $\beta(\nu_{\text{set}}, \nu_{\text{ref}}, t) = 1$ and red for $\beta(\nu_{\text{set}}, \nu_{\text{ref}}, t) = \beta(\nu_{\text{set}}, \nu_{\text{ref}})$), see text for details. The measured correction factor $\beta(\nu_{\text{set}}, \nu_{\text{ref}}, t)$, with its stable value, $\beta(\nu_{\text{set}}, \nu_{\text{ref}})$, fitted to the data, is added to the top panel of each figure. The different drift amplitudes originate from differences in the external conditions during the measurement.

ence a two-stage acceleration region before a field free drift towards a Multi Channel Plate (MCP) detector. At the MCP, the time-of-flight of copper ions is recorded to provide a mass resolving power of $R \approx 150$ for ^{63}Cu . For the gas jet, copper atoms are produced by resistively heating a copper filament inside a buffer gas cell filled with argon. After laser ionization in the jet formed by a de Laval nozzle, placed at the gas-cell exit, these ions are transported through a set of Radio-Frequency Quadrupoles (RFQ's) and ion optical elements to a dipole magnet mass separator ($R \approx 300$) on high voltage. The mass-separated ions are finally detected by an MCP. More details on the setup system is available in [15, 31]. A schematic overview of the laser setup for an ABU measurement is shown in Fig. 9. The scheme for in-gas-jet measurements is similar with the exception that the laser beams are sent to the adjacent separator lab for overlap in the gas jet. An example of the resulting hyperfine structure, obtained from an ABU measurement, is visualized in the bottom part of Fig. 10. The measuring protocol, automatized in the IGLIS Control Software and outlined in [15] provides, together

with additional systematic checks, all data required to specify the expected uncertainties on both the ion rate and wavelength determination. The uncertainty on the ion arrival rate, I , is deduced from the standard deviation of a number of measurements, $I \pm \Delta I = \langle I \rangle \pm \sqrt{\langle I^2 \rangle - \langle I \rangle^2}$, at a specific wavelength,. The uncertainty on the wavelength ν comprises of several components $\Delta \nu_{\text{stat}}, \Delta \nu_{\text{stab}}, \Delta \nu_{\text{drift}}, \Delta \nu_{\text{corr}}$, combining to $\nu_{\alpha} \pm \Delta \nu_{\alpha} = \langle \nu \rangle \pm \sqrt{(\Delta \nu_{\text{stat}})^2 + (\Delta \nu_{\text{stab}})^2 + (\Delta \nu_{\text{drift}})^2 + (\Delta \nu_{\text{corr}})^2}$. Here, $\Delta \nu_{\text{stat}}$ represents the standard deviation of all wavelength values read out by the WS7-60 in a specific wavelength step, typically $\Delta \nu_{\text{stat}} \approx 1$ MHz, see [15]. $\Delta \nu_{\text{stab}}$ covers the stability of the frequency reference, ≈ 1 MHz in one hour for the HeNe and < 1 MHz for the potassium-locked diode laser. Third, $\Delta \nu_{\text{drift}}$ describes the uncertainty on the WS7-60's drift correction. For the IGLIS control software, $\beta(\nu_{\text{set}}, \nu_{\text{ref}}, t) = 1$. In this case, $\Delta \nu_{\text{drift}}$ remains < 1 MHz for a scan at 654.98 nm, see Fig. 7a. Finally, $\Delta \nu_{\text{corr}}$ can be added to account for any applied corrections to the WS7-60 output. Within these specifications, a multitude of scans are performed in high resolution mode in the ABU. For each scan, a

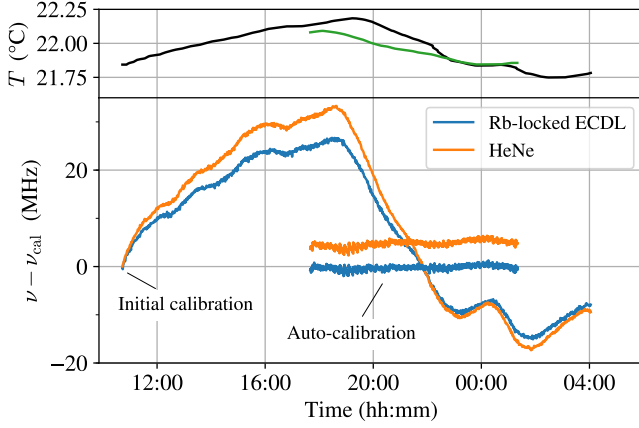


Figure 8: Long-term frequency drifts in the readout of the WSU-30 for the HeNe laser (orange) and the Rb-locked ECDL (blue). Lower panel: deviation of the frequency readout ν to the frequency readout at the time of calibration ν_{cal} . The measurement was performed two times: firstly with one initial calibration and secondly with auto-calibration (AC) in a 10 min interval to the Rb-locked ECDL. For better readability the HeNe frequency has an offset of +5 MHz in the measurement with AC. Upper panel: temperature readout of the WSU-30 for the measurement without AC (black) and with AC (green).

delay of around 6 ns between excitation and ionization laser pulses was implemented to find the optimal compromise between linewidth reduction and scan time [32]. The obtained FWHM of the resonances was between 110-130 MHz, including the natural linewidth, the Fourier-limited amplified TA:pro laser linewidth (≈ 70 MHz) and some residual power broadening from the ionization laser. In addition, for the in-gas-jet data, a resolution of ≈ 400 MHz was achieved, consisting of the components already mentioned added to a $T \approx 22$ K Doppler ensemble in a Mach 7.5 jet. The final results for the hyperfine parameters of $^{63,65}\text{Cu}$ are summarized in Table II. These values are obtained after evaluation with the Statistical Analysis Toolbox for Laser Spectroscopy (SATLAS) module in python [33]. This software is designed specifically to analyze the data of laser spectroscopy experiments and allows for both χ^2 and maximum likelihood fitting procedures. A model for the hyperfine structure of the element of interest is fitted directly to the experimental spectrum, providing both hyperfine parameters and resonance characteristics. From Table II, a consistent and reproducible disagreement $> 10\sigma$, with literature on the value $a(^{63}\text{Cu,g.s.})$ is found. The WS7-60 to SFPI comparison in Fig. 10 shows, however, an overestimation of the relative distances, defining for example the ^{63}Cu ground-state splitting, as indicated by the relative difference in position on the $\Delta_{\text{SFPI-WS7}}(\nu)$ function of the particular resonances in the figure. Therefore, to improve the WS7-60's precision, the wavelength array in

the hyperfine spectra is corrected by a fit of the waveform in Fig. 10. Because the fine structure of $\Delta_{\text{SFPI-WS7}}(\nu)$ as a function of wavelength is much more complex than a triangular waveform, a spline generated by the *splrep* function of the *scipy* python library, weighted by the errors on each measurement point, was used to describe its behavior by finding the B-spline representation of the curve. The distribution of residuals from this spline were used to define $\Delta\nu_{\text{corr}} \approx 1$ MHz. The resulting hyperfine parameters, obtained after correcting the wavelength array of each scan by the spline function, are shown in Table II. This correction procedure alters the readout of the WS7-60 such that it would match that of the SFPI reference. Agreement with literature is obtained for $^{63,65}\text{Cu}$ within $1\sigma = 0.5(^{63}\text{Cu}), 0.8(^{65}\text{Cu})$ MHz for the ABU, and $1.25\sigma = 2$ MHz for the gas jet, respectively, taking into account only statistical errors. This correspondence means that with the correction applied to the WS7-60 output, an uncertainty $\Delta\nu_{\alpha\beta,\text{total}}^{654,98} = 3$ MHz is achieved in this specific wavelength region. Combining the results for both hyperfine a parameters of $^{63,65}\text{Cu}$, reveals $a(^{63}\text{Cu,g.s.})/a(^{63}\text{Cu,e.s.}) = 1.600(11)$ and $a(^{65}\text{Cu,g.s.})/a(^{65}\text{Cu,e.s.}) = 11.620(17)$, respectively, excluding any hyperfine anomaly within this precision. An isotope shift $\delta\nu^{63-65}$ of 573.7(18) MHz can also be extracted from the data, also in agreement with literature [34, 35].

In case no spline correction were applied, an additional non-stochastic systematic error would have to be introduced to the resulting observables, $a_{\text{Cu,g.s.}}$, $a_{\text{Cu,e.s.}}$ and $\delta\nu^{63-65}$, such that $\Delta\nu_{\alpha\beta,\text{total}}^{654,98}$ is bound by a specific condition from Table I. When no information is available on the wavelength meter response in the required range, the conservative absolute uncertainty of the device (60 MHz for WS7-60) should be taken into account.

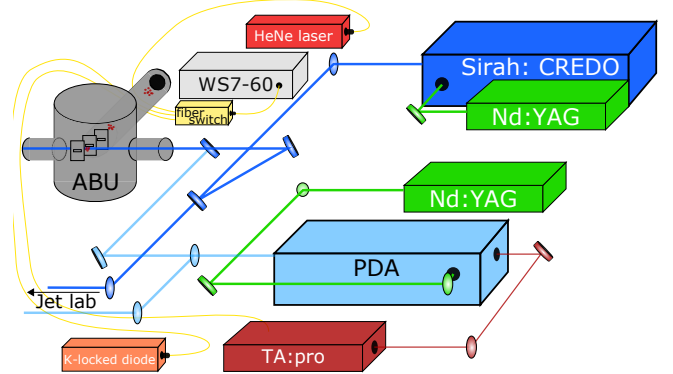


Figure 9: Schematic overview of the setup used to determine the hyperfine parameters of the $4s\ ^2S_{1/2}$ to $4p\ ^2P_{1/2}$ transition. For the in-gas-jet measurements, the UV laser beams were guided to the adjacent offline beam separator lab, see [15, 31].

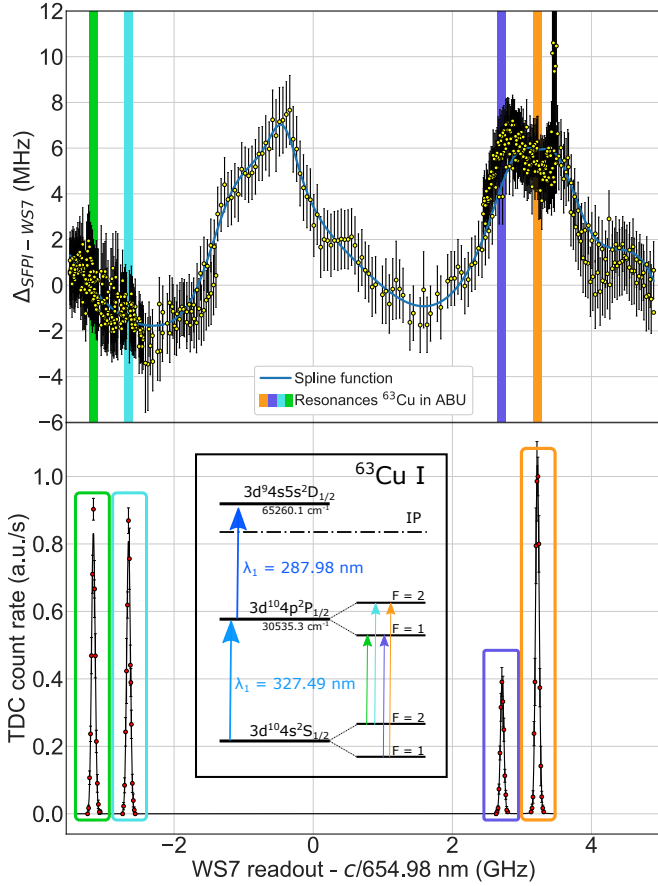


Figure 10: Visualization of the correction to the WS7-60 output. The upper panel shows a zoom of $\Delta_{\text{SFPI-WSX}}(\nu)$ in the wavelength range of the $4s\ ^2S_{1/2}$ to $4p\ ^2P_{1/2}$ hyperfine structure in copper. The spline function corrects each individual wavelength number given by the WS7-60 during the frequency scan such that $\Delta_{\text{SFPI-WSX}}(\nu) = 0$ and no apparent disagreement with the SFPI reference exists. The bottom panel shows a typical copper hyperfine spectrum with the fitted lineshape. All frequency values have been reported with respect to the fundamental wavelength, which is read by the wavelength meter. The results of the $\Delta_{\text{SFPI-WSX}}(\nu) = 0$ correction on the hyperfine parameters are shown in table Table II.

V. CONCLUSION

In this paper, two performance aspects of several commercial wavelength meters (HighFinesse GmbH), which are commonly used to monitor, stabilize and scan a laser's wavelength in medium/high-resolution laser hyperfine spectroscopy experiments, are investigated in a number of laboratories. First, the measurement uncertainty of wavelength differences in the order of 10 GHz, $\Delta\lambda_{\alpha\beta}$, which is directly related to the final physical observables of interest, is determined by a comparison to

Literature	$a(^{63}\text{Cu,g.s.})$ (MHz)	$a(^{63}\text{Cu,e.s.})$ (MHz)	
		5866.90871(2)	505.2 (8)
Experiment	$a(^{63}\text{Cu,g.s.})$ (MHz)	$a(^{63}\text{Cu,e.s.})$ (MHz)	
	ABU	5874.4(5)	505.0(5)
	ABU	5866.9(5)	505.8(5)
	Gas jet	5873(2)	506(2)
	Gas jet	5870(2)	506(2)

Literature	$a(^{65}\text{Cu,g.s.})$ (MHz)	$a(^{65}\text{Cu,e.s.})$ (MHz)	
		6284.38997(6)	542.9(16)
Experiment	$a(^{65}\text{Cu,g.s.})$ (MHz)	$a(^{65}\text{Cu,e.s.})$ (MHz)	
	ABU	6290.9(8)	539.9(8)
	ABU	6284.0(8)	541.0(8)

Table II: Literature values for the hyperfine parameters of the $4s\ ^2S_{1/2}$ to $4p\ ^2P_{1/2}$ transition in ^{63}Cu and ^{65}Cu compared to results obtained for the measurements in the ABU and in a gas jet. The correction to the WS7-60 wavelength meter output, discussed in the text, was applied to the data with the \bar{X} mark [34–37].

both an SFPI and a GPS-referenced frequency comb. For these frequency differences, induced by the hyperfine interaction, it was observed that the wavelength meters, which were all performing within specifications of the manufacturer, exhibit reproducible, quasi-periodic wavelength and device-dependent discrepancies with other reference sources, with the period lying close to the free spectral range of the device's most precise interferometer. This rather inexpensive, practical and simple characterization allows for a firm determination of the $\Delta\lambda_{\alpha\beta}$ in the wavelength range of interest. Either $\Delta\lambda_{\alpha\beta}$ can be reduced to the measurement uncertainty of the comparison, by correcting the observed periodic behavior or, the peak-to-peak discrepancy of the observed pattern is used to define an additional systematic uncertainty $\Delta\lambda_{\alpha\beta}$. In case no comparison is performed, the absolute uncertainty, quoted by the manufacturer, remains the only trustworthy source for $\Delta\lambda_{\alpha\beta}$. This procedure was validated by laser spectroscopy on $^{63-65}\text{Cu}$ isotopes in an Atomic Beam Unit (ABU) and in a gas jet. Finally, to ensure stable performance when probing rare exotic isotopes over longer times, two different solutions are validated, both taking advantage of an external reference source's wavelength stability. In conclusion the quoted absolute measurement uncertainty of the specific wavelength meter should coincide with the expected attainable precision on the physical observables of the experimental laser-spectroscopy technique. In case the former significantly exceeds the latter, an extra characterization of the wavelength meter, as described here, should be performed in the specific wavelength range of interest in order to provide a trustworthy estimate of the measurement uncertainty. This statement, alongside complementary investigations discussed here and in [1], should provide guidelines for users of these devices, both in their

operation and in potential new acquisitions.

ACKNOWLEDGMENTS

This work has received funding from Research Foundation Flanders (FWO, Belgium), from the Excellence of Science program (EOS, FWO-FNRS, Belgium), by GOA/2015/010 and STG/15/031 (BOF KU Leuven), by the Interuniversity Attraction Poles Program initiated by the Belgian Science Policy Office (BriX network P7/12), from the European Union's Horizon 2020 research and innovation program under Grants Agreement No. 654002 (ENSAR2), from the European Re-

search Council under the European Union's Seventh Framework Program (ERC-2011-AdG-291561-HELIOS), from the German Federal Ministry of Education and Research (BMBF) under contracts 05P19RDFN1 and 05P18RFCIA and from the German Research Foundation (DFG) under contract DU 1134/1-2. M.V. is supported by an FWO grant (Aspirant - 1121820N). A significant share of the research work described herein originates from R&D carried out in the frame of the FAIR Phase-0 program of LASPEC/NUSTAR. The authors would like to thank both F. Karlewski (HighFinesse) for his efforts and the fruitful discussions and P. Imgram (TU Darmstadt) for his support with the transfer cavity setup at JYFL.

-
- [1] K. König, P. Imgram, J. Krämer, B. Maaß, K. Mohr, T. Ratajczyk, F. Sommer, and W. Nörtershäuser, 'On the performance of wavelength meters -- Part 2: Frequency-comb based characterization revealing their relative limitations and offering opportunities for more accurate absolute wavelength determinations', submitted for publication in *Applied Physics B* (2019).
- [2] B. Sanguinetti, H. O. Majeed, M. L. Jones, and B. T. Varcoe, *J. Phys. B: At. Mol. Opt. Phys.* **42**, 165004 (2009).
- [3] K. Saleh, J. Millo, A. Didier, Y. Kersalé, and C. Lacroûte, *Appl. Opt.* **54**, 9446 (2015).
- [4] L. Couturier, I. Nosske, F. Hu, C. Tan, C. Qiao, Y. H. Jiang, P. Chen, and M. Weidemüller, *Rev. of Sci. Instrum.* **89**, 043103 (2018).
- [5] L. A. Johnson, H. O. Majeed, B. Sanguinetti, T. Becker, and B. T. Varcoe, *New J. Phys.* **12**, 063028 (2010).
- [6] A. Koszorus, 'Precision measurements of the charge radii of potassium isotopes', accepted for publication *Phys. Rev. C* (2019).
- [7] K. Blaum, J. Dilling, and W. Nörtershäuser, *Phys. Scrip.* **T152** (2013).
- [8] P. Campbell, I. D. Moore, and M. Pearson, *Prog. Part. Nucl. Phys.* **86** (2016).
- [9] V. N. Fedosseev, Y. Kudryavtsev, and V. I. Mishin, *Phys. Scr.* **85**, 058104 (2012).
- [10] B. A. Marsh, T. Day Goodacre, S. Sels, Y. Tsunoda, B. Andel, A. N. Andreyev, N. A. Althubiti, D. Atanasov, A. E. Barzakh, J. Billowes, K. Blaum, T. E. Cocolios, J. G. Cubiss, J. Dobaczewski, G. J. Farooq-Smith, D. V. Fedorov, V. N. Fedosseev, K. T. Flanagan, L. P. Gaffney, L. Ghys, M. Huyse, S. Kreim, D. Lunney, K. M. Lynch, V. Manea, Y. Martinez Palenzuela, P. L. Molkanov, T. Otsuka, A. Pastore, M. Rosenbusch, R. E. Rossel, S. Rothe, L. Schweikhard, M. D. Seliverstov, P. Spagnoletti, C. Van Beveren, P. Van Duppen, M. Veinhard, E. Verstraelen, A. Welker, K. Wendt, F. Wienholtz, R. N. Wolf, A. Zadornaya, and K. Zuber, *Nature Physics* **14**, 1163 (2018).
- [11] R. Ferrer, A. Barzakh, B. Bastin, R. Beerwerth, M. Block, P. Creemers, H. Grawe, R. de Groote, P. Delahaye, X. Fléchar, S. Franchoo, S. Fritzsche, L. P. Gaffney, L. Ghys, W. Gins, C. Granados, R. Heinke, L. Hijazi, M. Huyse, T. Kron, Y. Kudryavtsev, M. Laatiaoui, N. Lecesne, M. Loiselet, F. Lutton, I. D. Moore, Y. Martínez, E. Mogilevskiy, P. Naubereit, J. Piot, S. Raeder, S. Rothe, H. Savajols, S. Sels, V. Sonnenschein, J. C. Thomas, E. Traykov, C. Van Beveren, P. Van den Bergh, P. Van Duppen, K. Wendt, and A. Zadornaya, *Nature Communications* **8**, 14520 (2017).
- [12] S. Raeder, T. Kron, R. Heinke, J. L. Henares, N. Lecesne, P. Schönberg, M. Trümper, and K. Wendt, *Hyperfine Interact.* **238**, 15 (2017).
- [13] R. Neugart, J. Billowes, M. Bissell, K. Blaum, B. Cheal, K. Flanagan, G. Neyens, W. Nörtershäuser, and D. T. Yordanov, *J. Phys. G* **44** (2017).
- [14] Y. Kudryavtsev, R. Ferrer, M. Huyse, P. Van den Bergh, and P. Van Duppen, *Nucl. Instrum. Methods B* **297**, 7 (2012).
- [15] K. Dockx, T. E. Cocolios, R. Ferrer, C. Granados, S. Kraemer, Y. Kudryavtsev, S. Sels, P. Van den Bergh, P. Van Duppen, M. Verlinde, E. Verstraelen, and A. Zadornaya, *Nucl. Instrum. Methods B* **463**, 297 (2020).
- [16] S. Rothe, B. A. Marsh, C. Mattolat, V. N. Fedosseev, and K. Wendt, *J. Phys.: Conference Series* **312**, 052020 (2011).
- [17] S. Raeder, S. Fies, H. Tomita, K. D. A. Wendt, T. Iguchi, and K. Watanabe, in *AIP Conference Proceedings* (AIP, 6–10 October 2008) pp. 96–101.
- [18] H. Tomita, C. Mattolat, T. Kessler, S. Raeder, F. Schweltnus, K. D. A. Wendt, K. Watanabe, and T. Iguichi, *J. Nucl. Sci. Technol.* **45**, 37 (2008).
- [19] V. Sonnenschein, S. Raeder, A. Hakimi, I. D. Moore, and K. Wendt, *J. Phys. B* **45**, 165005 (2012).
- [20] A. Hakimi, T. Fischbach, S. Raeder, N. Trautmann, and K. Wendt, *Hyperfine Interact.* **216**, 59 (2013).
- [21] R. Heinke, T. Kron, S. Raeder, T. Reich, P. Schönberg, M. Trümper, C. Weichhold, and K. Wendt, *Hyperfine Interact.* **238**, 127 (2017).
- [22] T. Kessler, H. Tomita, C. Mattolat, S. Raeder, and K. Wendt, *Laser Phys.* **18**, 842 (2008).
- [23] V. Sonnenschein, I. D. Moore, S. Raeder, M. Reponen, H. Tomita, and K. Wendt, *Laser Phys.* **27**, 085701 (2017).
- [24] W. Zhao, J. Simsarian, L. Orozco, and G. Sprouse, *Rev. Sci. Instrum.* **69**, 3737 (1998).
- [25] D. Studer, J. Ulrich, S. Braccini, T. S. Carzaniga, R. Dressler, K. Eberhardt, R. Heinke, U. Köster,

- S. Raeder, and K. Wendt, *Eur. Phys. J. A* **56**, 69 (2020).
- [26] J. Krämer, K. König, C. Geppert, P. Imgram, B. Maaß, J. Meisner, E. Otten, S. Passon, T. Ratajczyk, J. Ullmann, and W. Nörtershäuser, *Metrologia* **55**, 268 (2018).
- [27] P. Imgram, K. König, J. Krämer, T. Ratajczyk, R. Müller, A. Surzhykov, and W. Nörtershäuser, *Phys. Rev. A* **99**, 012511 (2019).
- [28] I. Moore, T. Eronen, D. Gorelov, J. Hakala, A. Jokinen, A. Kankainen, V. Kolhinen, J. Koponen, H. Penttilä, I. Pohjalainen, M. Reponen, J. Rissanen, A. Saastamoinen, S. Rinta-Antila, V. Sonnenschein, and J. Äystö, *Nucl. Instrum. Methods B* **317**, 208 (2013), xVIth International Conference on ElectroMagnetic Isotope Separators and Techniques Related to their Applications, December 2–7, 2012 at Matsue, Japan.
- [29] R. de Groote, A. de Roubin, P. Campbell, B. Cheal, C. Devlin, T. Eronen, S. Geldhof, I. Moore, M. Reponen, S. Rinta-Antila, and M. Schuh, *Nucl. Instrum. Methods B* **463**, 437 (2019).
- [30] B. Cheal, M. Gardner, M. Avgoulea, J. Billowes, M. Bissell, P. Campbell, T. Eronen, K. Flanagan, D. Forest, J. Huikari, A. Jokinen, B. Marsh, I. Moore, A. Nieminen, H. Penttilä, S. Rinta-Antila, B. Tordoff, G. Tungate, and J. Äystö, *Phys. Lett. B* **645**, 133 (2007).
- [31] A. Zadornaya, P. Creemers, K. Dockx, R. Ferrer, L. P. Gaffney, W. Gins, C. Granados, M. Huuse, Y. Kudryavtsev, M. Laatiaoui, E. Mogilevskiy, S. Raeder, S. Sels, P. Van Den Bergh, P. Van Duppen, M. Verlinde, E. Verstraelen, M. Nabuurs, D. Reynaerts, and P. Papadakis, *Phys. Rev. X* **8**, 41008 (2018).
- [32] R. P. De Groote, M. Verlinde, V. Sonnenschein, K. T. Flanagan, I. Moore, and G. Neyens, *Phys. Rev. A* **95**, 1 (2017).
- [33] W. Gins, R. P. de Groote, M. L. Bissell, C. Granados Buitrago, R. Ferrer, K. M. Lynch, G. Neyens, and S. Sels, *Comput. Phys. Commun.* **222**, 286 (2018).
- [34] P. Vingerhoets, *Nuclear structure of Cu isotopes studied with collinear laser spectroscopy*, Ph.D. thesis, KU Leuven (2011).
- [35] G. Hermann, G. Lasnitschka, C. Schwabe, and D. Spengler, *Spectrochim. Acta, Part B* **48B**, 1259 (1993).
- [36] H. Figger, D. Schmitt, and S. Penselin, *Colloq. Int. C.N.R.S* **164** (1967).
- [37] H. Bucka, J. Ney, and P. Wirtnik, *Zeitschrift für Physik* **202**, 22 (1967).



III

COLLINEAR LASER SPECTROSCOPY OF STABLE PALLADIUM ISOTOPES AT THE IGISOL FACILITY

by

S. Geldhof, P. Campbell, B. Cheal, R. P. de Groot, W. Gins, I. D. Moore
Hyperfine Interactions 241: 41 (2020)

Licensed under Creative Commons CC BY.

<https://doi.org/10.1007/s10751-020-01713-3>



Collinear laser spectroscopy of stable palladium isotopes at the IGISOL facility

Sarina Geldhof¹ · Paul Campbell² · Bradley Cheal³ · Ruben de Groot¹ · Wouter Gins¹ · Iain Moore¹

Published online: 10 March 2020
© The Author(s) 2020

Abstract

Collinear laser spectroscopy on stable palladium isotopes was performed at the IGISOL facility in Jyväskylä in preparation for an experiment on its neutron-rich isotopes. Five transitions from different initial atomic states were tested, with the goal of finding the most spectroscopically efficient. The observed intensities afforded a comparison with atomic-level population predictions based on charge-exchange calculations. For some transitions hyperfine parameters of ^{105}Pd were measured, which were found to be in good agreement with literature values. A King plot analysis was performed using the measured isotope shifts and known charge radii from literature to determine the atomic field and mass shift factors.

Keywords Collinear laser spectroscopy · Palladium · IGISOL

1 Introduction

An experimental campaign to fill in the gap in optical spectroscopy data of radioactive isotopes in the region from $Z = 43$ to $Z = 47$ was started at the IGISOL facility at the Accelerator Laboratory in Jyväskylä. There are pertinent outstanding questions on the nuclear structure of neutron-rich nuclei in this region, with possible (rapid) changes in deformation and the presence of shape coexistence. These refractory elements can be produced at the IGISOL facility thanks to the chemical insensitivity of the production method. Having recently completed successful measurements on several neutron-rich silver isotopes, the next element of choice is palladium. Knowledge about the ground-state properties is needed

This article is part of the Topical Collection on *Proceedings of PLATAN 2019, 1st International Conference, Merger of the Poznan Meeting on Lasers and Trapping Devices in Atomic Nuclei Research and the International Conference on Laser Probing, Mainz, Germany 19-24 May 2019*
Edited by Krassimira Marinova, Michael Block, Klaus D.A. Wendt and Magdalena Kowalska

✉ Sarina Geldhof
sarina.m.geldhof@jyu.fi

¹ Department of Physics, University of Jyväskylä, PB 35 (YFL), 40014 Jyväskylä, Finland

² School of Physics and Astronomy, University of Manchester, Manchester M13 9PL, UK

³ Department of Physics, University of Liverpool, Liverpool L69 7ZE, UK

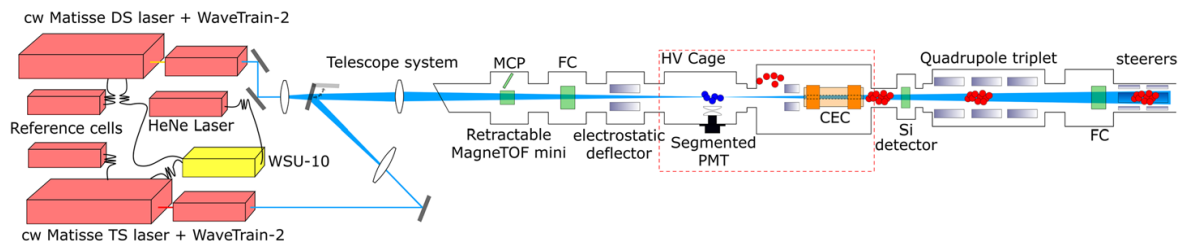


Fig. 1 Schematic view of the light collection region and laser systems of the collinear beamline at IGISOL. The ion bunches (red) enter the beamline from the right side. CEC = Charge-Exchange Cell, PMT = Photo-Multiplier Tube, MCP = Micro-Channel Plate detector, FC = Faraday Cup

to clarify the shape evolution and spin assignments in the Pd isotopic chain, as conflicting interpretations have arisen from several gamma- and beta-decay spectroscopy experiments [1–3].

In preparation for an experiment on radioactive neutron-rich isotopes, extensive offline testing was performed on all stable Pd isotopes, which is presented here. Several transitions suitable for collinear laser spectroscopy were tested in order to select the most efficient choice for online investigations. This also allowed the determination of the atomic field and mass shift factors, which are needed to extract the changes in mean-square charge radii from the isotope shifts.

2 Experimental setup

At the IGISOL facility, radioactive ion beams are produced using the ion-guide method with thin foil targets. Various offline sources are available to provide stable ion beams, such as a spark discharge source which was used in this work [4]. After production, beams are mass separated using a dipole magnet, with a typical mass resolving power of about 400, and injected into the radiofrequency quadrupole (RFQ) cooler-buncher. Ions are extracted from the cooler-buncher at an energy of 800 eV, and after passing through two 90-degree quadrupole benders are subsequently accelerated to 30 keV upon injection into the collinear beamline [5].

A schematic overview of this recently upgraded [6] beamline is shown in Fig. 1. Electrostatic deflectors guide the ions into the charge-exchange cell (CEC) and the light collection region (LCR). A quadrupole triplet is used to focus the beam in front of the Photo-Multiplier Tube (PMT). Ion and laser beams are overlapped in a counter-propagating geometry by tuning both through a removable 0.9 mm aperture. The beamline furthermore has two Faraday cups and a silicon detector which are used to optimize the transport efficiency of stable and radioactive ions, respectively. An off-axis Micro-Channel Plate (MCP) detector and a MagneTOF mini-detector mounted on a linear actuator are installed after the CEC and LCR, which are used for both beam tuning and monitoring the neutralization efficiency.

A new laser system has been installed recently to replace the Spectra Physics 380 dye laser. The new system consists of two Sirah Matisse 2 continuous wave (cw) lasers, one dye DS and one Ti:sapphire TS, both with a WaveTrain 2 frequency doubling unit. They are pumped by a 20W Spectra Physics Millennia eV laser. Both lasers have an external reference cavity to ensure short-term stability. To ensure long-term wavelength stability, these reference cavities can in turn be locked to a HighFinesse WSU-10 wavemeter using a built-in software plug-in or to a frequency-stabilized HeNe laser using a transfer cavity [7]. The (frequency-doubled) laser light required for the atomic transitions studied in this work is

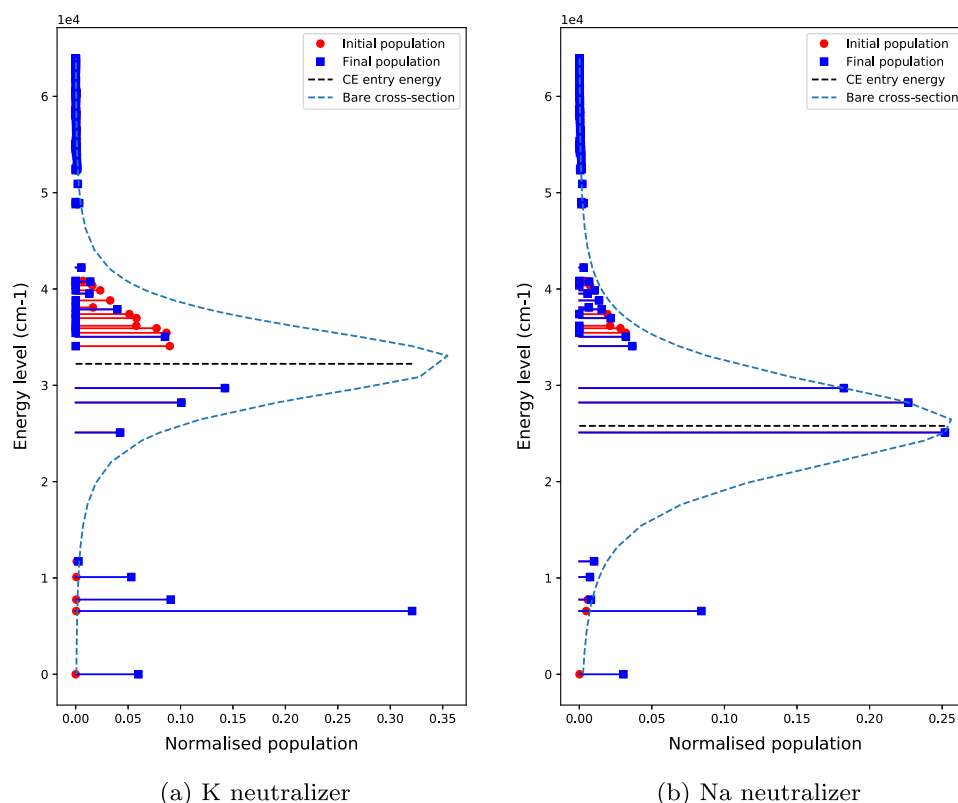


Fig. 2 Charge-exchange calculations predicting final level populations, using either (a) potassium or (b) sodium as the neutralizing vapour [8]

focused into a 1 mm spot in front of the PMT using a telescope system. Background rates due to scattered laser light are typically 100 Hz per 100 μ W of laser light.

3 Results

As any strong transitions in the Pd^+ ion are inaccessible to standard continuous-wave laser systems due to the very short wavelengths, spectroscopy must be performed on the neutral atom. To this end, neutralization by passage of the ion beam through a charge-exchange cell filled with an alkali vapour is utilized. This creates a population distribution among the atomic ground state and several metastable states. From these states, five different transitions were tested which were chosen based on several considerations: the level populations predicted by charge-exchange calculations, the expected transition strength, the atomic spins involved, and the available wavelength range of the laser system. The predicted level populations were calculated with the code described in [8] for a 30 keV beam with either potassium or sodium as the neutralizing vapour. The results can be seen in Fig. 2. The most suitable transitions found in literature are from the ground state and low-lying metastable states, and thus potassium was chosen as the neutralizer as it results in significantly higher final populations for these states of interest. A neutralization efficiency of 30% was measured for Pd^+ ions via the ratio of the total detected beam on the MagneTOF mini detector to that when a deflection voltage is applied to the electrostatic deflector, indicated in Fig. 1.

An overview of the tested transitions with their electronic configurations can be seen in Fig. 3. For the 363.6-, 357.2- and 361.1-nm transitions, spectra on all six stable isotopes, $^{102,104,105,106,108,110}\text{Pd}$, could be collected. Measurements using the 369.1-nm

Fig. 3 Overview of studied transitions. Wavelengths are in vacuum [9]

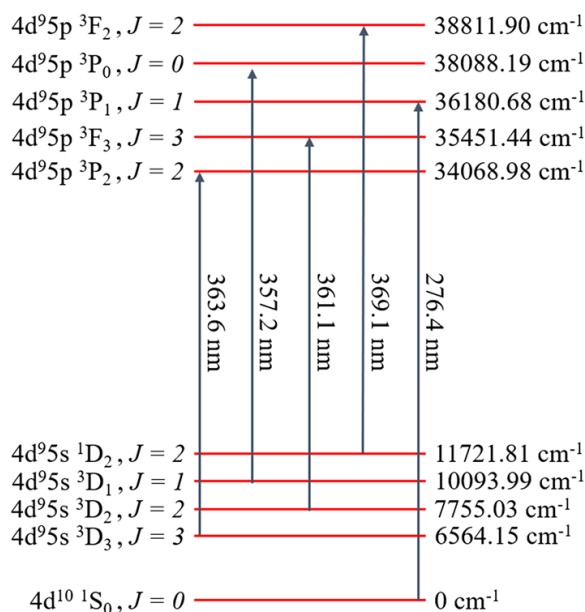


Table 1 Measured hyperfine parameters of ¹⁰⁵Pd compared to literature. Errors on measured values are statistical errors arising from the fitting procedure

Level	A (MHz)		B (MHz)	
	This work	Literature	This work	Literature
4d ⁹ 5p 3P ₁	-126.2(6)	-126.9(6) ^a	6(2)	2.0(9) ^a
4d ⁹ 5s 3D ₃	-391.5(4)	-391.178(1) ^b	-650(5)	-652.906(15) ^b
4d ⁹ 5p 3P ₂	-82.2(5)	-81(2) ^c	-302(4)	-312(7) ^c
4d ⁹ 5s 3D ₂	64.2(4)	66.359(1) ^b	-406(4)	-398.192(10) ^b
4d ⁹ 5p 3F ₃	-115.3(3)	-112(3) ^c	-497(4)	-536(33) ^c

^aref. [13] ^b ref. [14] ^c ref. [11]

transition were not pursued in detail for ¹⁰⁵Pd, which exhibits a hyperfine structure with 13 resonances, since spectra obtained on the even-*A* isotopes showed comparatively low efficiencies for this line. The 276.4-nm transition studied separately proved to be too low in efficiency. Only spectra for ^{105,108}Pd were obtained due to technical difficulties during this period. The low efficiency is due to a combination of a low population of the ground state and a lower quantum efficiency of the PMT at this wavelength.

All spectra were fitted using the SATLAS package [10]. For ¹⁰⁵Pd, the intensity ratios of the hyperfine components were fixed using the Racah coefficients. The hyperfine parameters obtained from the fits for ¹⁰⁵Pd on three transitions are compared to literature values in Table 1. The corresponding spectra with fits can be seen in Fig. 4. Even though a clear spectrum was obtained for the 357.2-nm transition, two of the three resonances were fully unresolved which made it impossible to reliably determine the hyperfine parameters of the lower state, so they were fixed to literature values from [11]. All measured parameters are in good agreement with previous values from literature. From the fitted centroids the isotope shifts relative to *A* = 108 have been calculated and can be found in Table 2. The included systematic error arises from the uncertainty in the determination of the cooler and acceleration voltages and was evaluated using the procedure described in [12].

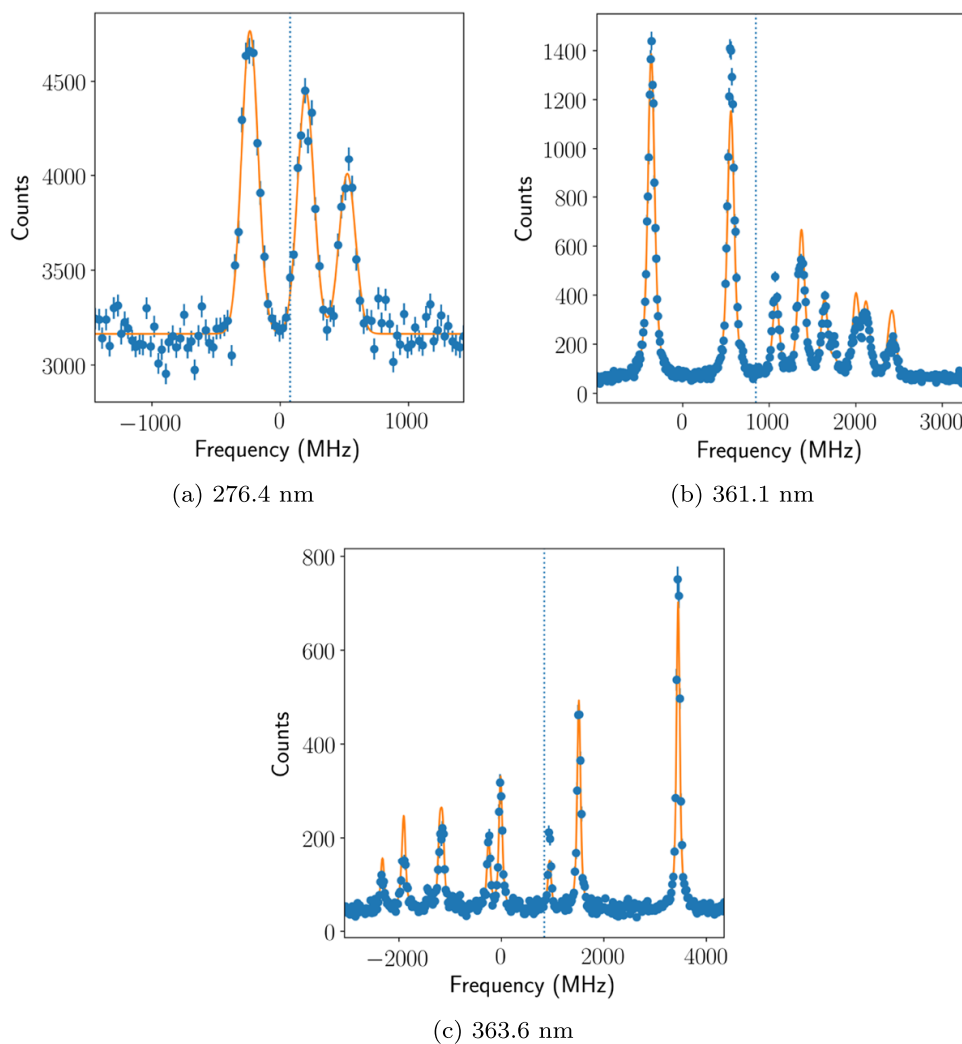


Fig. 4 Spectra of ^{105}Pd with hyperfine fits for all transitions where hyperfine parameters could reliably be determined. Dotted lines denote the center of gravity relative to ^{108}Pd . Fitted parameters can be found in Table 1

Table 2 Measured isotope shifts. Statistical uncertainties are denoted by parentheses and systematic uncertainties due to the conversion from scanning voltages into frequencies are given in square brackets

Isotope	$\delta\nu^{108,A}$ (MHz)				
	363.6	361.1	357.2	369.1	276.4
102	1446.9(6)[190]	1413.6(14)[190]	1446(4)[20]	1337(4)[19]	/
104	954.3(5)[130]	948.4(11)[130]	958(3)[13]	889(4)[13]	/
105	836.9(7)[100]	844.7(9)[100]	842(2)[10]	/	77(3)[13]
106	492.9(5)[60]	486.2(11)[60]	490(2)[7]	464(3)[6]	/
108	0.0	0.0	0.0	0.0	0.0
110	-434.6(6)[60]	-429.4(15)[60]	-443(5)[7]	-401(3)[6]	/

In order to compare the measured peak intensities with the predicted level populations, the particle current and laser power were recorded for each scan. ^{102}Pd , the isotope with lowest abundance (1.02%), was chosen to avoid saturating the RFQ. The scaled intensities

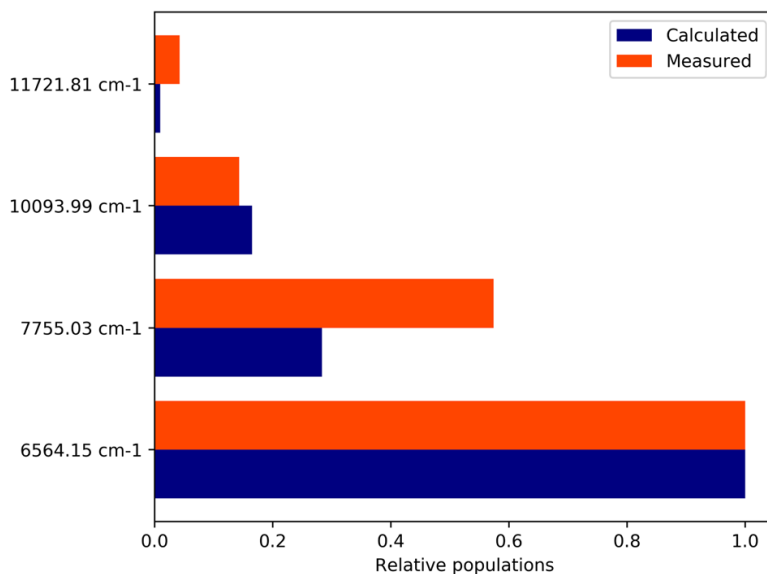


Fig. 5 Measured relative populations determined from ¹⁰²Pd peak intensities compared to predictions [8]

relative to the strongest level can be seen in Fig. 5. The overall order in population distribution is as expected from calculations, but the measurements suggest the 7755.03 cm⁻¹ and 11721.81 cm⁻¹ levels are about a factor of two more populated, or the other two levels a factor of two less. This is most likely due to decay from unknown higher-lying levels which are not included in the calculations.

The level populations are also reflected in the spectroscopic efficiencies achieved for each transition. In this work, the efficiencies are defined according to the number of photons emitted per ion detected at the end of the collinear beamline. For the 363.6-nm transition, ~ 1/7000 photons per ion was reached, while for the 361.1-nm transition it was ~ 1/11000. All other transitions had less than 1/90000 photons/ion, making them unfeasible for experiments on neutron-rich isotopes where the number of ions at the end of the beamline is expected to vary from 2000–15000 pps for ^{112–118}Pd, based on a combination of known fission yield cross sections, as well as scaled mass-separated yields from previously measured Ag isotopes at the IGISOL facility [15].

4 King plot analysis

The optical isotope shift between nuclei with atomic masses *A* and *A'*, δ*v*^{*A',A*}, is related to the change in mean-squared charge radii by

$$\begin{aligned} \delta v^{A',A} &= v^A - v^{A'} \\ &= \left(\frac{1}{m_{A'}} - \frac{1}{m_A} \right) M + F \delta \langle r^2 \rangle^{A',A}. \end{aligned} \tag{1}$$

M and *F* are the transition-dependent atomic mass and field shift factors, which must be determined either theoretically or empirically via the King plot technique [16]. The King plot uses either changes in charge radii obtained from non-optical methods or known atomic

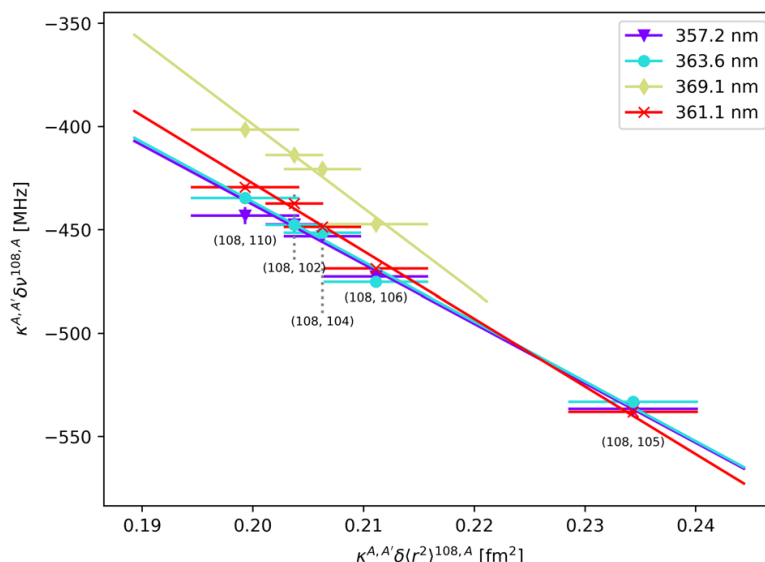


Fig. 6 King plots for all studied transitions. Modified changes in mean-square charge radii are calculated using charge radii obtained from muonic X-rays [17]

Table 3 Atomic field and mass shift factors determined using the King plot technique

Transition (nm)	Field shift (GHz/fm ²)	Mass shift (GHz amu)
363.6	−2.9(6)	845(669)
361.1	−3.3(6)	1346(773)
357.2	−2.9(6)	814(685)
369.1	−4(2)	2444(2782)

factor information from another transition to determine the atomic factors for the transition in question. Multiplying (1) with a modification factor κ ,

$$\kappa^{A,A'} = \frac{m_A m_{A'}}{m_A - m_{A'}} \times \frac{m_{A_{ref}} - m_{A'_{ref}}}{m_{A_{ref}} m_{A'_{ref}}} \tag{2}$$

removes the dependence on nuclear masses and includes a standard reference pair $A_{ref} = 110$ and $A'_{ref} = 108$ for presentation. The modified isotope shifts are then written as

$$\kappa^{A,A'} \delta\nu_i^{A',A} = \frac{m_{110} - m_{108}}{m_{110} m_{108}} \times M_i + F_i \kappa^{A,A'} \delta\langle r^2 \rangle^{A',A} \tag{3}$$

where i specifies the transition. The modified isotope shifts can be plotted against the modified changes in mean-squared charge radii and should yield a straight line, where the gradient contains the field shift factor and the intercept yields the mass shift factor.

In the case of palladium, the charge radii for all stable isotopes are known from muonic X-ray experiments [17]. The King plots for all transitions can be seen in Fig. 6, and the resulting field and mass shift factors in Table 3. As the field shift factor is related to the electron density at the nucleus, it is expected to be negative for transitions involving the promotion of an s-electron orbital to a p-electron orbital, as is the case for all transitions studied here. Due to the similar configurations involved, the field and mass shift factors are similar in magnitude for all transitions.

5 Summary and outlook

Offline testing on stable Pd isotopes has been performed in preparation for an experiment on neutron-rich isotopes produced in proton-induced fission of uranium. Five transitions, each with a different initial atomic state, were tested to determine the optimal approach in terms of spectroscopic efficiency and sensitivity to nuclear structure, and in order to calibrate the atomic factors. It was shown that charge-exchange calculations based on [8] provide a good starting point to choose transitions, but do not reproduce the observed populations exactly. In the end, the 363.6-nm transition from the 6564.15 cm^{-1} level showed to be the most efficient and thus the optimal choice to perform optical spectroscopy in the upcoming experiment. The atomic factors for this transition are the field shift $F = -2.9(6) \text{ GHz/fm}^2$ and mass shift $M = 845(669) \text{ GHz amu}$. These factors will allow the extraction of the unknown changes in mean-square charge radii of the neutron-rich isotopes from their isotope shifts.

Acknowledgements Open access funding provided by University of Jyväskylä (JYU). This work has received funding from the European Unions Horizon 2020 research and innovation program under Grants Agreement No. 654002 (ENSAR2). We gratefully acknowledge W. Nörtershäuser for the use of the charge-exchange cell.

Open Access This article is licensed under a Creative Commons Attribution 4.0 International License, which permits use, sharing, adaptation, distribution and reproduction in any medium or format, as long as you give appropriate credit to the original author(s) and the source, provide a link to the Creative Commons licence, and indicate if changes were made. The images or other third party material in this article are included in the article's Creative Commons licence, unless indicated otherwise in a credit line to the material. If material is not included in the article's Creative Commons licence and your intended use is not permitted by statutory regulation or exceeds the permitted use, you will need to obtain permission directly from the copyright holder. To view a copy of this licence, visit <http://creativecommons.org/licenses/by/4.0/>.

References

1. Kurpeta, J., Urban, W., Płochocki, A., Rissanen, J., Elomaa, V.V., Eronen, T., Hakala, J., Jokinen, A., Kankainen, A., Karvonen, P., Moore, I.D., Penttilä, H., Rahaman, S., Saastamoinen, A., Sonoda, T., Szerypo, J., Weber, C., Äystö, J.: Excited states in ^{115}Pd populated in the β^- decay of ^{115}Rh . *Phys. Rev. C* **82**(027), 306 (2010)
2. Houry, M., Lucas, R., Porquet, M.G., Theisen, C., Girod, M., Aiche, M., Aleonard, M.M., Astier, A., Barreau, G., Becker, F., Chemin, J.F., Deloncle, I., Doan, T.P., Durell, J.L., Hauschild, K., Korten, W., Le Coz, Y., Leddy, M.J., Perries, S., Redon, N., Roach, A.A., Scheurer, J.N., Smith, A.G., Varley, B.J.: Structure of neutron rich palladium isotopes produced in heavy ion induced fission. *Eur. Phys. J. A* **6**(1), 43–48 (1999)
3. Zhang, X.Q., Hamilton, J.H., Ramayya, A.V., Zhu, S.J., Hwang, J.K., Beyer, C.J., Kormicki, J., Jones, E.F., Gore, P.M., Babu, B.R.S., Ginter, T.N., Aryaeinejad, R., Butler-Moore, K., Cole, J.D., Drigert, M.W., Jewell, J.K., Reber, E.L., Gilat, J., Rasmussen, J.O., Daniel, A.V., Oganessian, Y.T., Ter-Akopian, G.M., Ma, W.C., Varmette, P.G., Bernstein, L.A., Loughheed, R.W., Moody, K.J., Stoyer, M.A.: Identification of high spin states in neutron-rich $^{113,115,117}\text{Pd}$ nuclei. *Phys. Rev. C* **61**(014), 305 (1999)
4. Vilén, M., Canete, L., Cheal, B., Giatzoglou, A., de Groote, R.P., de Roubin, A., Eronen, T., Geldhof, S., Jokinen, A., Kankainen, A., Moore, I.D., Nesterenko, D.A., Penttilä, H., Pohjalainen, I., Reponen, M., Rinta-Antila, S.: A new off-line ion source facility at IGISOL. *Nucl. Instrum. Methods Phys. Res. B* **463**, 382–383 (2020)
5. Vormawah, L.J., Vilén, M., Beerwerth, R., Campbell, P., Cheal, B., Dicker, A., Eronen, T., Fritzsche, S., Geldhof, S., Jokinen, A., Kelly, S., Moore, I.D., Reponen, M., Rinta-Antila, S., Stock, S.O., Voss, A.: Isotope shifts from collinear laser spectroscopy of doubly charged yttrium isotopes. *Phys. Rev. A* **97**(042), 504 (2018)
6. de Groote, R.P., de Roubin, A., Campbell, P., Cheal, B., Devlin, C.S., Eronen, T., Geldhof, S., Moore, I.D., Reponen, M., Rinta-Antila, S., Schuh, M.: Upgrades to the collinear laser spectroscopy experiment at the IGISOL. *Nucl. Instrum. Methods Phys. Res. B* **463**, 437–440 (2020)

7. Verlinde, M., Dockx, K., Geldhof, S., König, K., Studer, D., Cocolios, T.E., de Groote, R.P., Ferrer, R., Kieck, T., Moore, I.D., Nörtershäuser, W., Raeder, S., Van den Bergh, P., Van Duppen, P., Wendt, K.: On the performance of wavelength meters - Part 1: Consequences for medium- to high-resolution laser spectroscopy. Submitted (2019)
8. Vernon, A.R., Billowes, J., Binnersley, C.L., Bissell, M.L., Cocolios, T.E., Farooq-Smith, G.J., Flanagan, K.T., Ruiz, R.F.G., Gins, W., de Groote, R.P., Koszorús, Á., Lynch, K.M., Neyens, G., Ricketts, C.M., Wendt, K.D.A., Wilkins, S.G., Yang, X.F.: Simulation of the relative atomic populations of elements $1 \leq Z \leq 89$ following charge exchange tested with collinear resonance ionization spectroscopy of indium. *Spectrochim. Acta B* **153**, 61–83 (2019)
9. Engleman, R., Litzén, U., Lundberg, H., Wyart, J.F.: The Pd I spectrum, term system, isotope shift and hyperfine structure – revised and extended analysis based on FTS emission spectroscopy. *Phys. Scr.* **57**(3), 345–364 (1998)
10. Gins, W., de Groote, R.P., Bissell, M.L., Buitrago, C.G., Ferrer, R., Lynch, K.M., Neyens, G., Sels, S.: Analysis of counting data: Development of the SATLAS Python package. *Comput. Phys. Commun.* **222**, 286–294 (2018)
11. Kümmel, E., Baumann, M., Kischkel, C.S.: Hyperfine structure and isotope shift in the $4d^9 5s$ configuration of Pd I. *Z. Phys. D* **25**(2), 161–165 (1993)
12. Voss, A., Sonnenschein, V., Campbell, P., Cheal, B., Kron, T., Moore, I.D., Pohjalainen, I., Raeder, S., Trautmann, N., Wendt, K.: High-resolution laser spectroscopy of long-lived plutonium isotopes. *Phys. Rev. A* **95**(032), 506 (2017)
13. van Duijn, E.J., Witte, S., Zinkstok, R., Hogervorst, W.: Hyperfine structure and isotope shift measurements on $4d^{10} 1S_0 \rightarrow 4d^9 5p J = 1$ transitions in Pd I using deep-UV cw laser spectroscopy. *Eur. Phys. J. D* **19**(1), 25–29 (2002)
14. Channappa, K.H., Pendlebury, J.M.: Hyperfine structure measurements in some low-lying multiplets of ^{47}Ti , ^{49}Ti , ^{59}Co and ^{105}Pd . *Proc. Phys. Soc.* **86**(5), 1145–1146 (1965)
15. Geldhof, S. et al.: Collinear laser spectroscopy of radioactive Pd isotopes. Proposal to the JYFL PAC (2019)
16. King, W.H.: *Isotope Shifts in Atomic Spectra*. Plenum, New York (1984)
17. Fricke, G., Heilig, K.: *Nuclear Charge Radii*. Landolt-Börnstein/Springer, Berlin (2004)

Publisher's note Springer Nature remains neutral with regard to jurisdictional claims in published maps and institutional affiliations.